

**Shining Light on Dark Matter,
One Photon at a Time**

by

Brandon Leigh Allen

Submitted to the Department of Physics
in partial fulfillment of the requirements for the degree of

Doctorate of Science in Physics

at the

MASSACHUSETTS INSTITUTE OF TECHNOLOGY

June 2019

© Massachusetts Institute of Technology 2019. All rights reserved.

Author
Department of Physics
May 18, 2019

Certified by
Christoph E.M. Paus
Professor
Thesis Supervisor

Accepted by
Nergis Mavalvala
Associate Department Head for Education

**Shining Light on Dark Matter,
One Photon at a Time**

by

Brandon Leigh Allen

Submitted to the Department of Physics
on May 18, 2019, in partial fulfillment of the
requirements for the degree of
Doctorate of Science in Physics

Abstract

A search is conducted for new physics in final states containing a photon and missing transverse momentum in proton-proton collisions at $\sqrt{s} = 13$ TeV. The data collected by the CMS experiment at the CERN LHC correspond to an integrated luminosity of 35.9 inverse femtobarns. No deviations from the predictions of the standard model are observed. The results are interpreted in the context of dark matter production and limits on new physics parameters are calculated at 95% confidence level. For the two simplified dark matter production models considered, the observed (expected) lower limits on the mediator masses are both 950 (1150) GeV for 1 GeV dark matter mass.

Thesis Supervisor: Christoph E.M. Paus
Title: Professor

Acknowledgments

This is the acknowledgements section. You should replace this with your own acknowledgements.

Contents

1	The Standard Model	11
1.1	Strong Interactions	13
1.2	Hadrons	14
1.3	Electroweak Interactions	15
1.4	Electroweak Symmetry Breaking	16
1.5	Fermion Masses	18
1.6	Flavor Mixing	19
1.7	Summary	20
2	Dark Matter	23
2.1	Astrophysical Evidence	24
2.1.1	Galactic Clusters	24
2.1.2	Galactic Rotation Curves	25
2.1.3	Gravitational Lensing	26
2.1.4	Cluster Collisions	27
2.2	Relic Density	30
2.3	Dark Matter Candidates	32
2.3.1	Weakly-Interacting Massive Particles	33
2.3.2	Axions	33
2.3.3	Sterile Neutrinos	34
2.4	Simplified Models for LHC	36
2.5	Non-collider Searches	38
2.5.1	Direct Detection	38

2.5.2	Indirect Detection	41
2.6	Summary	43
3	The Large Hadron Collider	45
3.1	Experimental Apparatus	45
3.2	Collider Phenomenology	47
3.2.1	Parton Distribution Functions	49
3.2.2	Hard Scattering	50
3.2.3	Parton Shower	50
3.2.4	Hadronization	51
4	The CMS Detector	53
4.1	Inner Trackers	55
4.2	Electromagnetic Calorimeter	57
4.2.1	Preshower Detector	59
4.3	Hadronic Calorimeter	60
4.4	Muon Chambers	62
4.5	Online Trigger System	64
4.6	Detector Simulation	66
5	Reconstruction	67
5.1	Tracks	67
5.2	Primary Vertex	67
5.3	Particle Flow	67
5.4	Photons	67
5.5	Electrons	70
5.6	Muons	71
5.7	Hadrons and jets	71
5.8	Missing Transverse Energy	71
5.8.1	ECAL gain-switch effect	71
5.9	Beam Halo Phenomenology	72

5.10 ECAL Barrel Spikes Phenomenology	77
6 Calibration	85
6.1 Trigger Efficiency	85
6.2 Photon Identification Efficiency	87
6.2.1 e/γ ID Efficiency	88
6.2.2 γ -specific ID Efficiency	91
6.3 Lepton Efficiency	99
6.4 Pileup Reweighting	101
6.5 Lepton Veto Efficiency (Events with “Fake Leptons”)	102
6.6 Lepton Veto Efficiency (Events with “Real Leptons”)	104
7 The Monophoton Analysis	105
7.1 Event Selection	106
7.2 Irreducible backgrounds	108
7.2.1 Simulation of $V+\gamma$ Processes	108
7.2.2 Data-driven Control Regions	112
7.3 Misidentified electrons	118
7.4 Misidentified hadrons	119
7.5 Beam halo	125
7.6 Spikes	125
7.7 Statistical Interpretation	127
7.8 Results	128
7.8.1 Pre-fit and post-fit distributions	128
7.8.2 Limits	132

Chapter 1

The Standard Model

The Standard Model (SM) of particle physics describes the physical properties and dynamics of fermions, the fundamental constituents of matter, and their interactions in the language of a Lorentz-invariant quantum field theory (QFT). The Standard Model consists of a set of fermion fields, shown in Table 1.1 and the local gauge symmetry group that acts on them

$$G_{\text{SM}} = \text{SU}(3)_C \times \text{SU}(2)_L \times \text{U}(1)_Y, \quad (1.1)$$

which is composed of the subgroups

$$\begin{aligned} G_{\text{QCD}} &= \text{SU}(3)_C && \text{and} \\ G_{\text{EWK}} &= \text{SU}(2)_L \times \text{U}(1)_Y, \end{aligned} \quad (1.2)$$

corresponding to the strong and electroweak interactions, respectively. Each fermion field exists in a unique representation of G_{SM} , also summarized in Table 1.1. The possible representations of $\text{SU}(3)_C$ are triplet, conjugate, and singlet, denoted by **3**, **$\bar{3}$** , and **1**, respectively, while the possible representations of $\text{SU}(2)_L$ are doublet and singlet, denoted by **2** and **1**, respectively. All fermions exist in the singlet representation of $\text{U}(1)_Y$, only distinguished by differing values of the weak hypercharge Y . Conversely, all fermions in non-singlet representations of $\text{SU}(3)_C$ and $\text{SU}(2)_L$ have

the same interaction strength, a feature known as universality.

Table 1.1: The categories of SM fermions and the action of the SM local gauge symmetry group G_{SM} . Each category contains three members, one for each generation of the Standard Model. A corresponding table exists for the charge conjugated fields representing the anti-fermions. The subscripts L and R denote whether the field is left- or right-handed.

Name	Symbol	Y	$\text{SU}(2)_L$ rep.	$\text{SU}(3)_C$ rep.
Left-handed quark	q_L	$1/6$	2	3
Right-handed up-type quark	u_R	$2/3$	1	3
Right-handed down-type quark	d_R	$-1/3$	1	3
Left-handed lepton	ℓ_L	$-1/2$	2	1
Right-handed charged lepton	e_R	-1	1	1
Right-handed neutrino	ν_R	$1/6$	1	1

For each category of fermion listed in Table 1.1, there exist three generations or copies in the Standard Model, identical except for differing masses. The lepton electroweak doublets contain the left-handed charged leptons and neutrinos

$$\ell_L = \begin{pmatrix} \nu_e \\ e_L^- \end{pmatrix}, \begin{pmatrix} \nu_\mu \\ \mu_L^- \end{pmatrix}, \begin{pmatrix} \nu_\tau \\ \tau_L^- \end{pmatrix}, \quad (1.3)$$

and the right-handed lepton singlets contain the right-handed projections of the same leptons and neutrinos. The quark electroweak doublets contain the left-handed up-type and down-type quarks

$$q_L = \begin{pmatrix} u_L \\ d_L \end{pmatrix}, \begin{pmatrix} c_L \\ s_L \end{pmatrix}, \begin{pmatrix} t_L \\ b_L \end{pmatrix}, \quad (1.4)$$

and the right-handed quark singlets contain the right-handed projections of the same quarks. Quarks also exist in a strong triplet, which will be denoted with a superscript c as necessary.

1.1 Strong Interactions

The strong interactions of quarks and gluons are described by quantum chromodynamics (QCD), with the Lagrangian

$$\mathcal{L}_{\text{QCD}} = i\bar{q}_f^a D^\mu{}^{ab} q_f^b + m_f \bar{q}_f^a q_f^a - \frac{1}{4} G_{\mu\nu}^a G^{a,\mu\nu} + \theta \frac{g_s^2}{72\pi^2} \epsilon_{\mu\nu\rho\sigma} G^{c,\mu\nu} G^{c,\rho\sigma}, \quad (1.5)$$

where repeated indices are contracted. The q_f^a are the quark-field Dirac spinors of flavor $f \in \{u, d, c, s, t, b\}$, color $a \in \{r, g, b\}$ (the basis elements of the triplet representation), and mass m_f . The first term in Equation 1.5 contains the QCD covariant derivative

$$D_\mu^{ab} = \delta^{ab} \partial_\mu - ig_s \sum_c t_c^{ab} G_{c,\mu}, \quad (1.6)$$

where g_s is the strong interaction coupling strength, t_c are the eight 3×3 Hermitian traceless matrices that serve as the generators of the triplet representation of $\text{SU}(3)_C$, and G_c are the corresponding eight gluon fields. The third term in Equation 1.5 contains the gluon field strength tensors

$$G_{\mu\nu}^a = \partial_\mu G_\nu^a - \partial_\nu G_\mu^a - g_s f^{abc} G_\mu^b G_\nu^c, \quad (1.7)$$

where f^{abc} are the structure constants of $\text{SU}(3)_C$. The non-Abelian structure of the $\text{SU}(3)_C$ group allows for 3-gluon and 4-gluon interactions in addition to the quark-antiquark-gluon interactions.

The last term in Equation 1.5 violates CP conservation and produces a non-zero electric dipole moment (EDM) for the neutron. Experimental limits on the neutron EDM constrain the observed QCD vacuum angle θ to be smaller than 10^{-10} . The Peccei-Quinn theory provides a possible explanation for this contradiction by introducing the hypothetical axion particle a with the following Lagrangian

$$\mathcal{L}_a = \frac{1}{2} \partial_\mu a \partial^\mu a + \frac{g_s^2}{72\pi^2} \frac{a}{f_a} \epsilon_{\mu\nu\rho\sigma} G^{c,\mu\nu} G^{c,\rho\sigma} \quad (1.8)$$

, where f_a is axion decay constant that determines its characteristic scale. The second

term in Equation 1.8 cancels the last term in Equation 1.5 when the axion field dynamically assumes its vacuum expectation value $\langle a \rangle = -f_a\theta$. The axion is a potential dark matter candidate and will be discussed further in Section 2.3.2.

1.2 Hadrons

Free quarks and gluons are not observed in nature, only in bound states called hadrons. This is a consequence of two factors: color confinement and asymptotic freedom.

Color confinement is the hypothesis that colored objects are always confined to color singlet states and that no objects with non-zero color charge can propagate as free particles. Thus, quarks can only exist in bound states of a quark-antiquark pair or three quarks, called mesons and baryons, respectively. Since gluons carry a color charge, they are confined to hadrons as well. Confinement is a low-energy non-perturbative phenomenon, occurring only below the QCD confinement scale Λ_{QCD} . An analytic proof of color confinement does not exist currently; however, the running of the strong coupling constant $\alpha_s = g_s^2/4\pi$ provides a mechanism for it.

Due to higher-order corrections to propagators in a QFT, physical quantities such as coupling constants and masses acquire a scale-dependence, where the value of the quantity changes as a function of the probed energy scale q^2 . The process of recovering scale-invariance is called renormalization and ensures that any divergent terms from the higher-order corrections cancel out in the physical values. Given the value of an arbitrary coupling constant α at some known scale μ^2 , the value of α at arbitrary scale q^2 is

$$\alpha(q^2) = \frac{\alpha(\mu^2)}{1 - \alpha(\mu^2) [\Pi(q^2) - \Pi(\mu^2)]}, \quad (1.9)$$

where $\Pi(q^2)$ and $\Pi(\mu^2)$ are the self-energy correction of the propagator at scales q^2 and μ^2 . While these individual terms are separately divergent, their difference is finite and calculable.

For values of q^2 and μ^2 larger than the confinement scale Λ_{QCD} , the difference

between the gluon self-energy corrections to one-loop order is given by

$$\Pi_s(q^2) - \Pi_s(\mu^2) \approx -\frac{\beta}{4\pi} \ln \left(\frac{q^2}{\mu^2} \right) \quad (1.10)$$

where β depends on the number of quark and gluon loops. For N_c colors and N_f quark flavors with mass below $|q|$,

$$\beta = \frac{11N_c - 2N_f}{12\pi}. \quad (1.11)$$

In the Standard Model, $N_c = 3$ and $N_f \leq 6$ regardless of energy, thus β is always positive. Combining Equations 1.9 and 1.10, the evolution of α_s is given by

$$\alpha_s(q^2) = \frac{\alpha_s(\mu^2)}{1 + \beta \alpha_s(\mu^2) \ln \left(\frac{q^2}{\mu^2} \right)} \approx \frac{1}{\beta \ln \left(\frac{q^2}{\Lambda_{\text{QCD}}^2} \right)} \quad (1.12)$$

for a sufficiently large energy scale $q^2 \gg \Lambda_{\text{QCD}}^2$. Through electron-positron collisions, the value of α_s at the Z -pole has been measured to be $\alpha_s(m_Z^2) = 0.1181 \pm 0.0011$ with a corresponding confinement scale of $\Lambda_{\text{QCD}} = 218$ MeV.

From Equation 1.12, we see that α_s decreases with increasing q^2 . At $|q| \sim 1$ GeV, the value of α_s is of $\mathcal{O}(1)$ confining quarks and gluons to hadrons in a strongly-bound non-perturbative state. However, $|q| \gtrsim 100$ GeV, we have $\alpha_s \approx 0.1$ which is small enough that perturbation theory can be used and quarks can be treated as quasi-free particles. This property of QCD is known as asymptotic freedom.

1.3 Electroweak Interactions

The electroweak interactions of fermions are described by $SU(2)_L \times U(1)_Y$ gauge group, with the Lagrangian

$$\mathcal{L}_{\text{EWK}} = i\bar{\psi}_i \not{D} \psi_i - \frac{1}{4} \vec{W}_{\mu\nu} \cdot \vec{W}^{\mu\nu} - \frac{1}{4} B_{\mu\nu} B^{\mu\nu} \quad (1.13)$$

where repeated indices are contracted and $\psi \supseteq \{q_L, u_R, d_R, \ell_L, e_R, \nu_R\}$ is the set of SM fermions, and the gauge field tensors are given by

$$\begin{aligned} B_{\mu\nu} &= \partial_\mu B_\nu - \partial_\nu B_\mu \quad \text{and} \\ \vec{W}_{\mu\nu} &= \partial_\mu \vec{W}_\nu - \partial_\nu \vec{W}_\mu + g \vec{W}^\mu \times \vec{W}^\nu, \end{aligned} \quad (1.14)$$

where \vec{W}_μ and B_μ are the gauge fields for $SU(2)_L$ and $U(1)_Y$, respectively, and g is the coupling strength for $SU(2)_L$. The first term in Equation 1.13 contains the EWK covariant derivative

$$D_\mu = \partial_\mu - ig \vec{T} \cdot \vec{W}_\mu - ig' Y B_\mu, \quad (1.15)$$

where g' is the coupling strength for $U(1)_Y$, Y is the $U(1)_Y$ hypercharge of the fermion field, and \vec{T} are the generators of the doublet representation of $SU(2)_L$. The generators can be written in terms of the Pauli spin matrices $\vec{T} = \vec{\sigma}/2$ and only have non-zero action on left-handed particles. The values of the hypercharge Y shown in Table 1.1 are chosen such that the physical electric charge of each fermion is given by $Q = T_3 + Y$.

Notice that Equation 1.13 does not contain a Dirac mass term like that found in Equation 1.5. This is because the term

$$m \bar{\psi} \psi = m (\bar{\psi}_L \psi_R + \bar{\psi}_R \psi_L) \quad (1.16)$$

mixes the left-handed and right-handed fermions leading to a Lagrangian that is no longer invariant under $SU(2)_L$. As the observed fermions are not massless, the Lagrangian given in Equation 1.13 is incomplete and an additional mechanism needs to be introduced to produce non-zero fermion masses.

1.4 Electroweak Symmetry Breaking

Spontaneous electroweak symmetry breaking provides the mechanism we need, as well as providing masses to the weak gauge bosons. The $SU(2)_L$ symmetry is broken by introducing a left-handed complex scalar doublet ϕ with $Y_\phi = 1/2$ to the Lagrangian

in the following manner

$$\mathcal{L}_{\text{EWK}} \mapsto \mathcal{L}_{\text{EWK}} + |D_\mu \phi|^2 + \mu^2 \phi^2 - \lambda |\phi|^4. \quad (1.17)$$

We choose to write this complex doublet, known as the complex Higgs field, in terms of four real-valued fields so that

$$\phi = \frac{1}{\sqrt{2}} \begin{pmatrix} \phi_1 + i\phi_2 \\ \phi_3 + i\phi_4 \end{pmatrix}. \quad (1.18)$$

Fortunately, the two self-interaction terms create a Higgs potential with a degenerate global minimum at the vacuum expectation value (vev)

$$v \equiv \langle |\phi| \rangle = \sqrt{\frac{\mu^2}{\lambda}}, \quad (1.19)$$

and through gauge rotations we set $\langle \phi_{1,2,4} \rangle = 0$, removing three degrees of freedom and producing three massless Nambu-Goldstone bosons. The remaining degree of freedom is the real Higgs field H which expresses small perturbations around the vev in the third component of the complex Higgs field $\phi_3 = v + H$.

The kinetic term in Equation 1.17 couples the complex Higgs field to the EWK gauge bosons as follows at the vev

$$|D_\mu \phi|^2 = \frac{v^2}{8} \left[(gW_\mu^1)^2 + (gW_\mu^2)^2 + (g'B_\mu - gW_\mu^3)^2 \right]. \quad (1.20)$$

Diagonalizing this term gives rise to the three massive weak bosons and the massless photon that we observe in nature:

$$\left. \begin{aligned} W_\mu^\pm &\equiv \frac{1}{\sqrt{2}} (W_\mu^1 \mp W_\mu^2) \\ Z_\mu &\equiv \cos \theta_W W_\mu^3 - \sin \theta_W B_\mu \\ A_\mu &\equiv \sin \theta_W W_\mu^3 + \cos \theta_W B_\mu \end{aligned} \right| \begin{aligned} m_W &= \frac{1}{2} v g \\ m_Z &= \frac{1}{2} v \sqrt{g^2 + (g')^2} \\ m_A &= 0, \end{aligned} \quad (1.21)$$

where $\tan \theta_W = g'/g$. With this, we rewrite Equation 1.13 in terms of the observed

electromagnetic, charged weak, and neutral weak currents as follows:

$$\begin{aligned}\mathcal{L}_{\text{EWK}} = & \bar{\psi}_i (i\cancel{d} - eQ\cancel{A}) \psi_i - \frac{g}{2\sqrt{2}} \bar{\psi}_i \left(T^+ W^+ + T^- W^- \right) \psi_i - \frac{1}{2} m_W^2 W_\mu^+ W^{-\mu} \\ & - \frac{g}{2 \cos \theta_W} \bar{\psi}_i (g_V - g_A \gamma^5) \cancel{Z} \psi_i - \frac{1}{2} m_Z^2 Z_\mu Z^\mu,\end{aligned}\quad (1.22)$$

where $e = g' \cos \theta_W$ is the charge of the electron, $T^\pm = (T_1 \mp iT_2)/\sqrt{2}$ are the weak isospin raising and lowering operators, and $g_V = T_3$ and $g_A = T_3 - 2Q \sin^2 \theta_W$ are the vector and axial-vector couplings for the neutral weak current.

We can also expand Equation 1.17 about the vev giving us the following Higgs Lagrangian

$$\begin{aligned}\mathcal{L}_H = & \frac{1}{2} \partial_\mu H \partial^\mu H - \frac{1}{2} m_H^2 H^2 + \frac{m_H^2}{2v} H^3 + \frac{2m_W^2}{v} W_\mu^+ W^{-\mu} H + \frac{m_Z^2}{v} Z_\mu Z^\mu H \\ & + \frac{m_H^2}{8v^2} H^4 + \frac{m_W^2}{v^2} W_\mu^+ W^{-\mu} H^2 + \frac{m_Z^2}{2v^2} Z_\mu Z^\mu H^2,\end{aligned}\quad (1.23)$$

where $m_H = \mu\sqrt{2}$. Thus, we see that the real Higgs field H has trilinear and quartic couplings to itself and the weak gauge bosons with coupling strengths proportional to the mass squared of the appropriate boson. This suggests a way to introduce fermion masses through the Higgs field.

1.5 Fermion Masses

Introducing Yukawa couplings between the complex Higgs field ϕ and the SM fermion fields enables us to add mass terms for the fermions. First, we start with the terms for charged leptons,

$$\mathcal{L}_Y^{\text{leptons}} = -\bar{\ell}_L Y_e \phi e_R - \bar{e}_R Y_e^\dagger \phi^\dagger \ell_L,\quad (1.24)$$

where Y_e is the Yukawa matrix for the charged leptons. In general, Yukawa matrices and thus mass matrices are non-diagonal and hence we need to convert from the electroweak eigenstates $f_{L,R}$ to the mass eigenstates $\tilde{f}_{L,R} = U_{L,R}^f f_{L,R}$ where $U_{L,R}^f$ is a

unitary matrix. With this we rewrite Equation 1.24 in terms of the mass eigenstates

$$\begin{aligned}\mathcal{L}_Y^{\text{leptons}} &= -\bar{\tilde{\ell}}_L U_L^e Y_e \phi U_R^{e\dagger} \tilde{e}_R - \bar{\tilde{e}}_R U_R^e Y_e^\dagger \phi^\dagger U_L^{e\dagger} \tilde{\ell}_L \\ &= -\bar{\tilde{\ell}}_L \tilde{Y}_e \phi \tilde{e}_R - \bar{\tilde{e}}_R \tilde{Y}_e^\dagger \phi^\dagger \tilde{\ell}_L,\end{aligned}\quad (1.25)$$

where $\tilde{Y}_e = U_L^e Y_e U_R^{e\dagger}$ is the diagonalized Yukawa matrix for the charged leptons. After electroweak symmetry breaking, these terms become

$$\begin{aligned}\mathcal{L}_Y^{\text{leptons}} &= -\frac{v+H}{\sqrt{2}} \left(\bar{\tilde{e}}_L \tilde{Y}_e \tilde{e}_R + \bar{\tilde{e}}_R \tilde{Y}_e^\dagger \tilde{e}_L \right) \\ &= -\left(1 + \frac{H}{v} \right) \left(\bar{\tilde{e}}_L \tilde{M}_e \tilde{e}_R + \bar{\tilde{e}}_R \tilde{M}_e^\dagger \tilde{e}_L \right) \\ &= -\tilde{M}_e \bar{e} e - \frac{\tilde{M}_e}{v} \bar{e} e H,\end{aligned}\quad (1.26)$$

where $\tilde{M}_e = v \tilde{Y}_e / \sqrt{2}$ is the diagonalized mass matrix for the charged leptons and e is the set of massive Dirac spinors for the charged leptons.

From Equation 1.26, we see that the Yukawa couplings between the complex Higgs field ϕ and the charged leptons result in a Dirac mass term and a coupling to the real Higgs field H that is proportional to the mass of the charged leptons and the vev. The same procedure is used to introduce mass terms for the down-type quarks whereas for the neutrinos and up-type quarks we must use the conjugate doublet $\phi_c = -i\sigma_2\phi^*$ in place of ϕ to obtain the same result.

1.6 Flavor Mixing

For the charged leptons and up-type quarks, it is possible to define a basis of simultaneous electroweak and mass eigenstates, so in practice $\tilde{Y}_{e,u} = Y_{e,u}$ as $U_L^{e,u} = U_R^{e,u} = \mathbf{I}$. However, it is not possible to do this for the neutrinos at the same time as the charged leptons or for the down-type quarks at the same time as the up-type quarks.

In Equation 1.22, the charged current term involves interactions between the up-type and down-type quarks and is not preserved under the transform $f \rightarrow \tilde{f}$. Writing

this in terms of the mass eigenstates we have

$$\begin{aligned}\mathcal{L}_{\text{CC}} &= -\frac{g}{2\sqrt{2}} \left(\bar{u}_L T^+ W^+ d_L + \bar{d}_L T^- W^- u_L \right) \\ &= -\frac{g}{2\sqrt{2}} \left(\bar{u}_L T^+ W^+ V_{\text{CKM}} \tilde{d}_L + \bar{d}_L T^- W^- V_{\text{CKM}}^\dagger u_L \right),\end{aligned}\quad (1.27)$$

where $V_{\text{CKM}} = U_L^{u\dagger} U_L^d$ is the Cabibbo-Kaboyshi-Maskawa matrix and $u_L = \tilde{u}_L$ by construction. The CKM matrix is unitary with four free parameters, the mixing angles between quark generations $\phi_{12} = 13.1$, ϕ_{23} , and ϕ_{13} as well as a CP-violating phase δ . In terms of these parameters, the CKM matrix is

$$V_{\text{CKM}} = \begin{pmatrix} c_{12} & s_{12} & 0 \\ -s_{12} & c_{12} & 0 \\ 0 & 0 & 1 \end{pmatrix} \times \begin{pmatrix} 1 & 0 & 0 \\ 0 & c_{23} & s_{23} \\ 0 & -s_{23} & c_{23} \end{pmatrix} \times \begin{pmatrix} c_{13} & 0 & s_{13} e^{-i\delta} \\ 0 & 1 & 0 \\ -s_{13} e^{i\delta} & 0 & c_{13} \end{pmatrix}, \quad (1.28)$$

where $s_{ij} = \sin \phi_{ij}$ and $c_{ij} = \cos \phi_{ij}$. It has been experimentally determined that the CKM is mostly diagonal with $s_{13} \ll s_{23} \ll s_{12} \ll 1$.

The equivalent mixing matrix for the neutrinos is the Pontecorvo-Maki-Nakagawa-Sakata matrix U_{PMNS} , which converts from the mass eigenstates ν_1 , ν_2 , and ν_3 to the electroweak eigenstates ν_e , ν_μ , ν_τ . Unlike the CKM matrix, the PMNS is non-diagonal resulting in stronger mixing in the neutrino sector. The values of the mixing angles θ_{12} , θ_{23} , and θ_{13} have been measured in neutrino oscillation experiments while the CP-violating phase δ' has not yet been directly measured. From cosmological measurements, it is known that the sum of the neutrino masses is less than one eV.

1.7 Summary

The Standard Model has a total of 26 free parameters and 17 physical particles. The parameters are the twelve Yukawa couplings for the fermions, the four parameters of the CKM matrix, the four parameters of the PMNS matrix, the three coupling constants g_s , g , and g' , the Higgs vacuum expectation value v , the Higgs mass m_H , and the QCD vacuum angle θ . The best fit values of the SM parameters, excluding

Table 1.2: The free parameters of the Standard Model, not including masses.

Parameter	Description	Best Fit Value
ϕ_{12}	CKM 12-mixing angle	13.1°
ϕ_{23}	CKM 23-mixing angle	2.4°
ϕ_{13}	CKM 13-mixing angle	0.4°
δ	CKM CP-violating phase	0.995
$\sin^2 \theta_{12}$	PMNS 12-mixing angle	0.297
$\sin^2 \theta_{23}$	PMNS 23-mixing angle	0.437
$\sin^2 \theta_{13}$	PMNS 13-mixing angle	0.0214
δ'	PMNS CP-violating phase	1.35
g_s	SU(3) _C coupling constant	1.221
g	SU(2) _L coupling constant	0.652
g'	U(1) _Y coupling constant	0.357
v	Higgs vacuum expectation value	246 GeV
θ	QCD vacuum angle	$< 10^{-10}$

masses, are summarized in Table 1.2.

The physical particles are the single-particle states of the various mass eigenfields and their properties are summarized in Table 1.3. Each of the fermion fields has a corresponding anti-particle with the electromagnetic and color charges inverted. Most of these single-particle states have finite lifetimes and decay to lower energy configurations. The only particles whose decays have not been observed are the photon, the electron, the neutrinos, and the proton (a baryon of flavor content uud). Additionally, stable bound states of protons and neutrons (a baryon of flavor content udd) exist in the form of atomic nuclei.

Table 1.3: The physical particles of the Standard Model.

Name	Symbol	Spin	Charge	Mass
up quark	u	$\frac{1}{2}$	$\frac{2}{3}$	2.2 MeV
down quark	d	$\frac{1}{2}$	$-\frac{1}{3}$	4.7 MeV
charm quark	c	$\frac{1}{2}$	$\frac{2}{3}$	1.28 GeV
strange quark	s	$\frac{1}{2}$	$-\frac{1}{3}$	95 MeV
top quark	t	$\frac{1}{2}$	$\frac{2}{3}$	173 GeV
bottom quark	b	$\frac{1}{2}$	$-\frac{1}{3}$	4.18 GeV
electron neutrino	ν_e	$\frac{1}{2}$	0	-
electron	e	$\frac{1}{2}$	-1	511 keV
muon neutrino	ν_μ	$\frac{1}{2}$	0	-
muon	μ	$\frac{1}{2}$	-1	105 MeV
tau neutrino	ν_τ	$\frac{1}{2}$	0	-
tau	τ	$\frac{1}{2}$	-1	1.78 GeV
gluon	g	1	0	0
photon	γ	1	0	0
Z boson	Z	1	0	91.2 GeV
W boson	W^\pm	1	± 1	80.4 GeV
Higgs boson	H	0	0	125 GeV

Chapter 2

Dark Matter

As a theory of the fundamental particles and forces of nature, the Standard Model should also help explain physics at the largest scales. The Λ CDM model best explains all current cosmological observations including the structure of the cosmic microwave background; the abundances of hydrogen, helium, and lithium; the large-scale structure in the distribution of galaxies, and the accelerating expansion of the universe. However, the latest results from the Planck collaboration show that baryonic matter (matter consisting of various combinations of protons, neutrons, and electrons) only contributes $\sim 5\%$ of the total energy of the universe, with radiation (photons and relativistic neutrinos) contributing less than a hundredth of a percent.

The remaining 95% of energy comes from just two sources: $\sim 27\%$ from non-relativistic non-baryonic matter referred to as dark matter and $\sim 68\%$ from an unknown form of energy that permeates all of space referred to as dark energy. Current observations show that dark energy is uniform in space and time producing a similar effect to that of the cosmological constant in the Einstein field equations of general relativity. Not much else is known about dark energy, although there are many experiments attempting to discover additional properties. The work in this thesis shall focus on trying to explain dark matter.

Dark matter cannot be explained by the 17 particles of the Standard Model (see Section 2.3), yet its gravitational effects have been observed in many circumstances. The rest of this chapter will cover the astrophysical evidence for dark matter (Sec-

tions 2.1 and 2.2), various dark matter candidates (Section 2.3) and the models investigated at the LHC (Section 2.4), and non-collider searches for dark matter (Section 2.5).

2.1 Astrophysical Evidence

All existing evidence for dark matter comes from astrophysical observations of its gravitational effects on the universe at various length scales. We shall focus on four different sources of evidence: the average velocity of galaxies in clusters, the rotation curves of spiral galaxies, strong gravitational lensing, and merging galactic clusters. The evidence presented here is not exhaustive, see Reference ?? for more detail.

2.1.1 Galactic Clusters

Galactic clusters are the largest gravitational bound systems, with the orbital velocities of the individual clusters determined by the total gravitational mass of the cluster. Applying the Virial Theorem gives the explicit relation

$$v^2 = \frac{GM}{2r}, \quad (2.1)$$

where v is the average orbital velocity of a galaxy in the cluster, r is the average separation between galaxies in the cluster, M is the total gravitational mass of the cluster, and G is the Newtonian constant of gravitation. In 1933, Fritz Zwicky measured the average orbital velocity of the Coma cluster and discovered that it was a factor of ten larger than the observed visible mass of the Coma cluster, leading to the conclusion that the majority of the cluster consisted of non-luminous matter. Today studies show that stars only contribute 1% of the total cluster mass, with a hot, baryonic intracluster medium and dark matter contributing the remaining 14% and 85% of the total cluster mass, respectively.

2.1.2 Galactic Rotation Curves

Spiral galaxies are stable gravitational bound systems with stars and interstellar gas rotating around the galactic center in nearly circular orbits in a single plane. For these galaxies, the orbit of an individual star is stable when the gravitational force acting on the star balances the centripetal acceleration of the star. With this condition, the expected stellar velocity v is a function of distance r from the galactic center given by

$$v = \sqrt{\frac{GM(r)}{r}} \quad (2.2)$$

where $M(r)$ is the total gravitational mass inside radius r . Thus, past a certain critical radius r_c , the stellar velocity should fall with as $r^{1/2}$ as the mass of the galaxy is no longer increasing.

In 1980, Vera Rubin and Kent Ford observed that instead of decreasing at distances outside the visible galaxy, the stellar velocity stayed constant out to a very great distance, necessitating an additional non-luminous source of mass. The most common explanation for this missing mass is the existence of an isotropic dark matter halo surrounding the galaxy. With the inclusion of interstellar gas, the total mass inside radius r is given by

$$M(r) = 4\pi \int_0^r dr' (r')^2 [\rho_S(r') + \rho_g(r') + \rho_{DM}(r')], \quad (2.3)$$

where ρ_S , ρ_g , and ρ_{DM} are the density profiles of the stars, interstellar gas, and dark matter in the galaxy, respectively. Once these densities have been specified, it is possible to plot the fraction of the total stellar velocity due to each mass source as a function of distance from the galactic center.

Figure 2-1 shows the results of doing this using the observed stellar and interstellar mass density profiles and the expected density from an isotropic dark matter halo for two different spiral galaxies. In both cases, this reproduces the observed flat galactic rotation curve incredibly well, lending strong support for the existence of galactic dark matter halos.

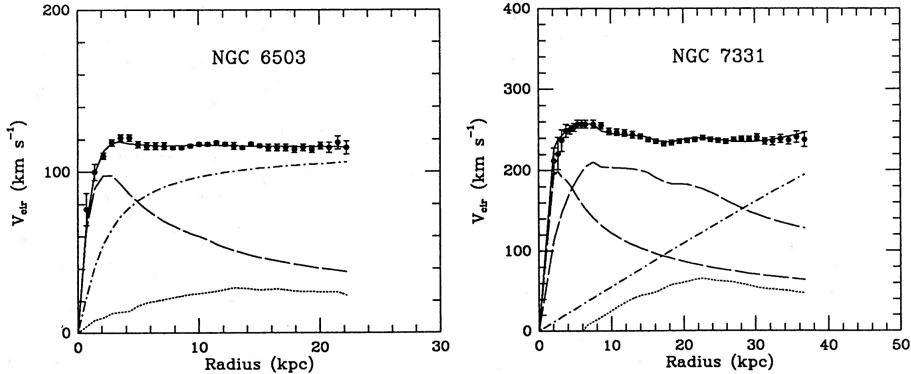


Figure 2-1: The observed (points) and fitted (solid line) rotation curves for two sample galaxies. The fit consists of three components: the stellar component (dashed), the interstellar gas (dotted), and the dark matter halo (dash-dotted). Reprinted from Reference [1].

2.1.3 Gravitational Lensing

As a consequence of Einstein's equivalence principle, a massive body will deflect light, a phenomenon known as gravitational lensing. In the language of general relativity, this means that the photons take the path given by the geodesic lines following the curvature of space-time due to the massive body. For most observations of gravitational lensing due to astrophysical bodies, the physical size of the lensing object is much smaller than the distance between observer, lens, and source allowing us to use the thin lens approximation. Approximating the lens as a planar distribution of matter, the angular deflection is given by

$$\vec{\alpha}(\vec{x}) = \frac{4G}{c^2} \int d^2x' \frac{\vec{x} - \vec{x}'}{|\vec{x} - \vec{x}'|^2} \int dz \rho(\vec{x}', z) \quad (2.4)$$

where \vec{x} is a two-dimensional vector in the plane of the lens, z is the perpendicular distance from the plane of the lens, and ρ is the three dimensional density. If the source is treated as a point mass, this reduces to

$$\alpha = \frac{4G}{c^2} \cdot \frac{M}{b} \quad (2.5)$$

where $b = |\vec{x} - \vec{x}'|$ is the impact parameter and M is the total mass of the object. Thus, measuring the angle of deflection due to gravitational lensing around an astrophysical object provides an independent measurement of the total mass of the body which can be compared against the mass of the luminous objects in the body.

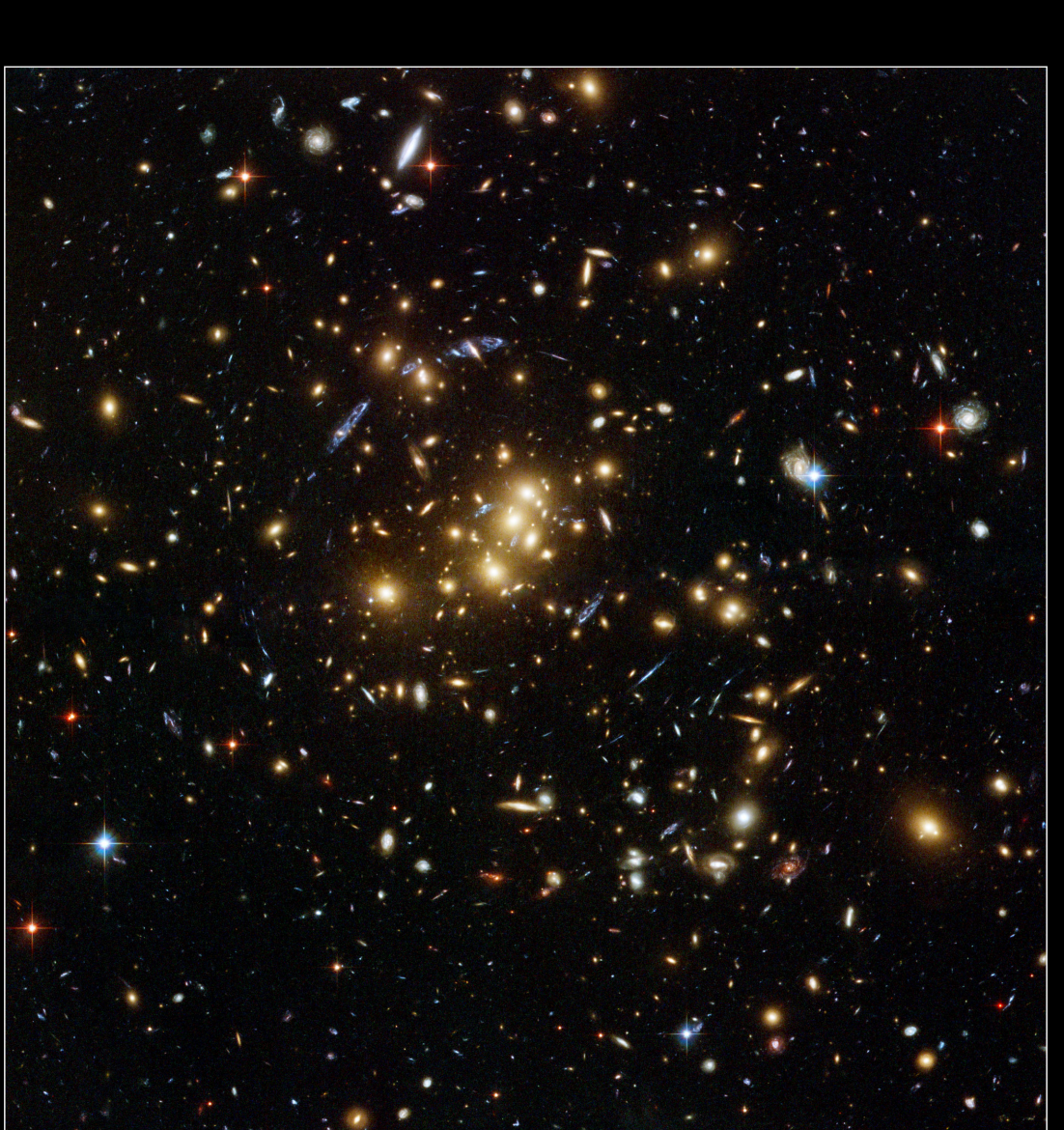
Depending on the mass of the deflecting body and impact parameter, the size of deflection can fall into three different regimes. The first of these is called strong lensing where the curving of space-time is so strong that light can travel multiple paths around the lens and still reach the observer. If the source is directly behind a circular lens, light travels around all sides of the lens and appears as an Einstein ring, while if the source is offset or the lens is non-circular, the source will instead appear in multiple locations as if viewed from slightly different angles. An example of strong lensing is shown in Figure 2-2.

The next regime is known as weak lensing, where the deflection is enough to distort the image of the source but not enough to result in multiple images. The shear of this distortion can be converted into a map of the projected mass distribution. True weak lensing results in circular “*E*-mode” patterns while sources of systematic uncertainty produce both “*E*-mode” and curl-like “*B*-mode” patterns. Thus, requiring a zero “*B*-mode” contribution assures that the measured mass distribution is accurate. Figure 2-3 shows the observed shear of half a million galaxies measured in the Hubble Space Telescope COSMOS survey.

The final regime is the microlensing that occurs when a lens moves relative to a luminous source. As the lens passes in front of the source, it will temporarily increase the apparent luminosity of the source, enabling a mass measurement of the lens. Microlensing results show that rocky exoplanets orbit other stars and that these planets cannot form the bulk of dark matter in the Milky Way.

2.1.4 Cluster Collisions

Additionally, gravitational lensing measurements of galactic cluster collisions provide support for dark matter and help constrain its properties. Figure 2-4 shows the merging cluster 1E0657-558. By comparing the weak lensing reconstruction of



Galaxy Cluster Cl 0024+17 (ZwCl 0024+1652)
Hubble Space Telescope • ACS/WFC

NASA, ESA, and M.J. Jee (Johns Hopkins University)

STScI-PRC07-17b

Figure 2-2: Strong gravitational lensing around galaxy cluster CL0024+17, consisting of the gravitationally bound yellow, elliptical galaxies. The elongated blue objects are from much more distant galaxies behind the cluster which are distorted into arcs due to gravitational lensing from the dark matter halo surrounding the cluster. Figure credit: NASA, ESA, M.J. Jee and H. Ford (Johns Hopkins University)

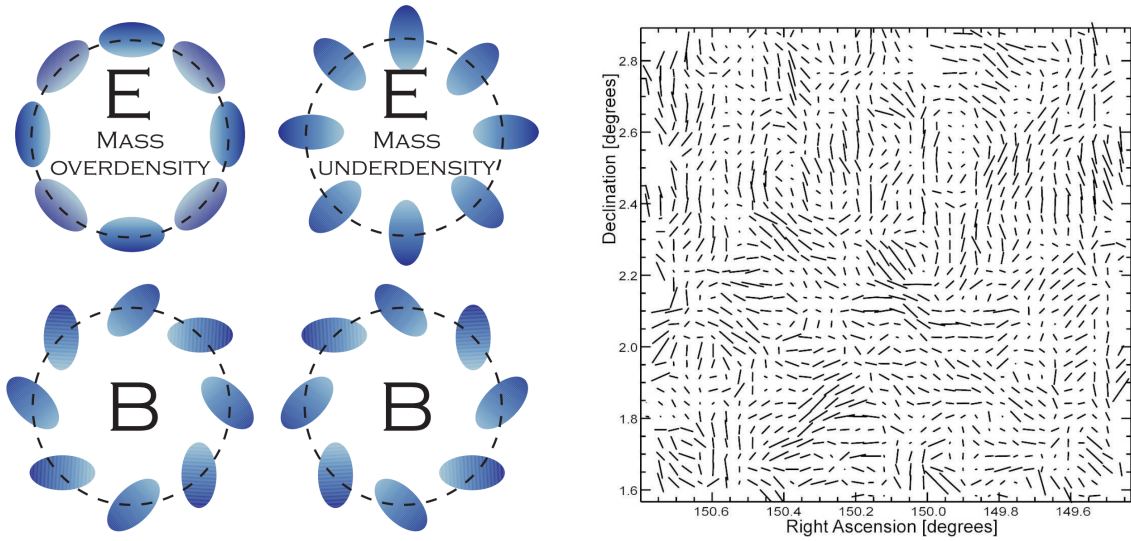


Figure 2-3: Left: Examples of circular “E-mode” and curl-like “B-mode” patterns. Right: The observed ellipticities of half a million distant galaxies within the 2 square degree Hubble Space Telescope COSMOS survey. Reprinted fom Reference [1].

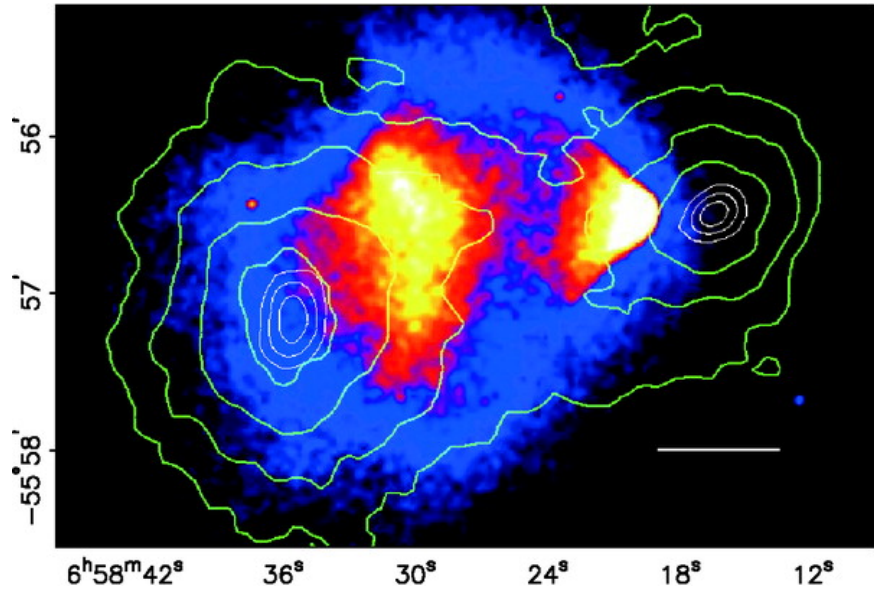


Figure 2-4: The merging cluster 1E0657-558. The green contours show the weak lensing reconstruction of the gravitational potential of the cluster. The colors indicate the X-ray temperature of the plasma, changing from blue to white as the plasma goes from coolest to hottest. The smaller “bullet” cluster on the right which traversed through the larger cluster on the left. Reprinted from Reference [1].

the gravitational potential of the cluster shown in green contours against temperature color gradient of the X-ray emitting interstellar plasma, it was learned that the gravitational potential of the cluster does not track the dominant baryonic mass contribution coming from the plasma. Instead, the gravitational potential tracks the smaller stellar baryonic mass component. Dark matter must be the dominant gravitational source in the cluster since the center of total mass is offset from the center of baryonic mass. Furthermore, the observation of two gravitational mass centers places strong constraints on the self-interaction of dark matter requiring that the observed mass must have a self-interaction collisional cross section $\sigma/m < 1.25 \text{ cm}^2\text{g}^{-1}$ at a 68% confidence level.

2.2 Relic Density

During the early universe, dark matter (DM) was in thermal equilibrium with the rest of the SM particles with a number density n_χ given by

$$n_\chi^{\text{eq}} = \frac{g}{(2\pi)^3} \int f(\vec{p}) d^3\vec{p}, \quad (2.6)$$

where g is the number of internal degrees of freedom of the DM particle χ and $f(\vec{p})$ is either the Fermi-Dirac or Bose-Einstein distribution, depending on the quantum statistics of the DM particle. At very high temperatures relative to the mass m_χ of the DM particle, dark matter and SM particles rapidly convert back and forth with a DM annihilation rate $\Gamma = \langle \sigma_A v \rangle \cdot n_\chi$, where $\langle \sigma_A v \rangle$ is the thermally averaged product of the total cross section for annihilation σ_A and the relative velocity v of the dark matter particles. After the temperature drops below m_χ , the DM annihilation rate Γ drops below the Hubble expansion rate H of the universe and the DM particles stop annihilating and freeze-out of equilibrium with the SM particles, leaving the DM relic density that we observe today. During the freeze-out process, the time dependence

of the number density n_χ is described by the Boltzmann equation as follows

$$\frac{dn_\chi}{dt} + 3Hn_\chi = -\langle\sigma_A v\rangle [(n_\chi)^2 - (n_\chi^{\text{eq}})^2]. \quad (2.7)$$

The LHS term accounts for the reduction in density due to the expansion of the universe. The two RHS terms account for the change in density due to annihilation and product of DM particles to and from SM particles, respectively.

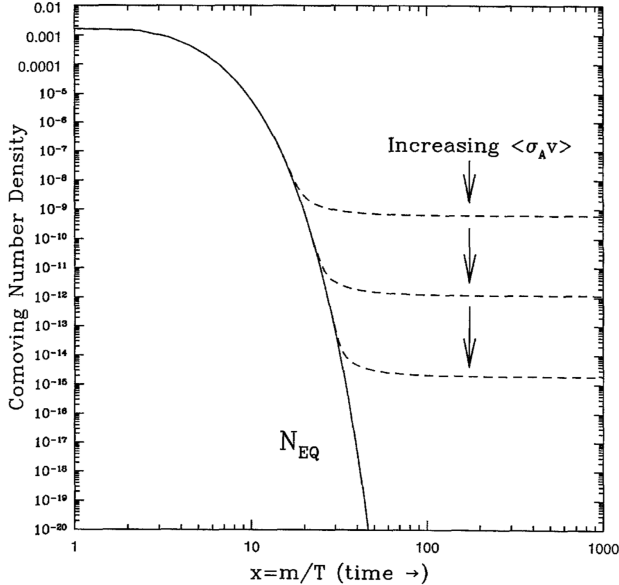


Figure 2-5: Number density of dark matter in the early universe as a function of time. The solid curves are the equilibrium abundance while the dashed curves are the actual abundance after freeze-out. Reprinted from Reference [1].

Figure 2-5 shows the calculated DM number density n_χ as a function of time in the early universe. As the annihilation cross section increases, the relic density decreases as the dark matter particles stay in equilibrium longer. We shall make an order-of-magnitude estimate of the relic density by assuming that $\langle\sigma_A v\rangle$ is independent of energy. Freeze-out occurs at the temperature T_f where the expansion rate $H(T)$ equals the annihilation rate $\Gamma(T)$. The temperature dependence of Γ is simply that of n_χ , e.g. $\Gamma \propto T^3$. Meanwhile, the early universe is radiation dominated, so we have that $H \propto T^2$. Furthermore, astrophysical measurements (see Section 2.1) can't give direct bounds on the number density, only on the mass density $\rho_\chi = m_\chi n_\chi$.

Additionally, mass densities are usually expressed as a fraction of the critical density of the universe $\rho_c = 3H^2/(8\pi G)$. Combining all of this, the relic density of dark matter is given by

$$\Omega_\chi \cdot h^2 = \frac{m_\chi n_\chi}{\rho_c} \simeq \frac{10^{-27} \text{ cm}^3 \text{ s}^{-1}}{\langle \sigma_A v \rangle}, \quad (2.8)$$

where $h = H_0/(100 \text{ km s}^{-1} \text{ Mpc}^{-1})$ is the reduced Hubble constant. Thus, to first order the DM relic density depends only on two things: the total DM annihilation cross section σ_A and the mass m_χ of the DM candidate, as after freeze-out $T \ll m_\chi$ and the velocity v is strictly proportional to m_χ . The latest Planck results measure that $\Omega_\chi \cdot h^2 = 0.1200 \pm 0.0012$, providing strong constraints on the possible values of σ_A and m_χ .

2.3 Dark Matter Candidates

Any dark matter candidate must satisfy the following criteria:

- No or extremely weak interactions with photons, e.g. be **dark**
- Weak baryonic interactions to preserve the DM halos discussed in Section 2.1.2
- Weak self-interactions as discussed in Section 2.1.4
- The observed relic density discussed in Section 2.2.

These four criteria place stringent requirements on dark matter candidates. The light neutrinos, the only SM particles satisfying the first three conditions, are excluded as the total neutrino relic density has a bound of $\Omega_\nu \cdot h^2 \leq 0.00067$ at 95% confidence level from analysis of the CMB anisotropies. Big Bang Nucleosynthesis and gravitational microlensing have mostly exclude non-luminous baryonic matter from forming the bulk of dark matter. Thus, most theories of dark matter propose a new fundamental particle as a dark matter candidate. The following sections discuss the most common dark matter candidates, namely weakly-interacting massive particles (WIMPs), axions, and sterile neutrinos.

2.3.1 Weakly-Interacting Massive Particles

The annihilation cross-section of new particle χ with electroweak scale interactions is approximately

$$\langle \sigma_A v \rangle \approx \left(\frac{\alpha \cdot g_\chi^2}{m_\chi} \right)^2 = \left(\frac{e^2}{4\pi} \cdot \frac{(0.8)^2}{100 \text{ GeV}} \right)^2 \simeq 10^{-26} \text{ cm}^3 \text{ s}^{-1}, \quad (2.9)$$

where $\alpha = e^2/4\pi$ is the fine-structure constant, $m_\chi = 100 \text{ GeV}$ is the mass of the particle, and $g_\chi \approx 0.8$ is the effective coupling for the four-point interaction $\chi\bar{\chi} \rightarrow f\bar{f}$. Plugging this into Equation 2.8, we obtain $\Omega_\chi \cdot h^2 \sim 0.1$, which is very close to the observed value. This numerical coincidence motivates a new weakly-interacting massive particle (WIMP) as a good DM candidate.

The only criteria to be a WIMP beyond the generic definition of dark matter is that the mass and interaction strength of the new particle must be approximately that of the EWK scale. Thus, a great many new physics models have WIMPs natively, such as the neutralino in supersymmetry and the lightest Kaluza-Klein particle in theories of universal extra dimensions. In this thesis, we shall focus on a set of simplified models that describe WIMP interactions in a relatively model-independent manner. For more details, see Section 2.4.

2.3.2 Axions

The hypothetical axion particle introduced in Section 1.1 is a dark matter candidate if the axion decay constant f_a is large enough as all axion-SM couplings are inversely proportional to it. Constraints from the observed duration of the neutrino burst from supernova SN 1987A require that $f_a \gtrsim 10^9 \text{ GeV}$, sufficiently high that the axion lifetime exceeds the age of the universe by many orders of magnitude. Thus, the axion is a viable DM candidate due to its long lifetime and weak couplings to SM particles.

After accounting for kinematic mixing with the π^0 and η mesons, the axion mass is given by

$$m_a = \left(\frac{\sqrt{m_u m_d}}{m_u + m_d} \right) \left(\frac{f_\pi}{f_a} \right) m_\pi \simeq \left(\frac{10^7 \text{ GeV}}{f_a} \right) \text{ eV}, \quad (2.10)$$

where f_π is the pion decay constant and m_u , m_d , and m_π are the masses of the up quark, the down quark, and the neutral pion, respectively. From this, we see that the axion mass is inversely proportional to f_a , leading to an upper limit of $m_a \lesssim 10 \text{ meV}$. The Planck measurements of the cosmic microwave background also provide a lower (upper) bound on the axion mass $m_a \gtrsim 10 \mu\text{eV}$ (axion decay constant $f_a \lesssim 10^{12} \text{ GeV}$), otherwise the axion abundance is too high.

The axion obtains a two-photon vertex through loops involving virtual quarks and gluons of the form

$$\mathcal{L}_{a\gamma\gamma} = \frac{1}{4} g_{a\gamma\gamma} \epsilon_{\mu\nu\rho\sigma} F^{\mu\nu} F^{\rho\sigma} a = -g_{a\gamma\gamma} (\vec{E} \cdot \vec{B}) a, \quad (2.11)$$

where $F^{\mu\nu}$ is the electromagnetic field-strength tensor, \vec{E} and \vec{B} are the electric and magnetic fields, respectively, and the coupling constant is

$$g_{a\gamma\gamma} = -\frac{\alpha}{3\pi f_a} \left(\frac{m_u + 4m_d}{m_u + m_d} \right). \quad (2.12)$$

From this, we can see that the axion's coupling to the photon is incredibly small unless in the presence of a strong electromagnetic field. Thus, astrophysical axions are **dark** unless they enter a region with such a field. Searches for axions such as CAST[] and ADMX[] exploit this to try to observe axion-to-photon conversions.

2.3.3 Sterile Neutrinos

In Section 1.5, we introduced mass for the SM fermions through the Higgs mechanism in order to preserve $SU(2)_L$ gauge invariance. However, since the right-handed neutrinos are singlets under the full $SU(3)_C \times SU(2)_L \times U(1)_Y$ gauge of the SM, it is possible to add explicit Majorana mass terms in addition to the Dirac mass terms in

the SM Lagrangian as follows

$$\begin{aligned}
\mathcal{L}_{\nu_R} &= i\bar{\nu}_R \not{\partial} \nu_R - (\bar{\ell}_L Y_\nu \phi_c \nu_R + \bar{\nu}_R Y_\nu^\dagger \phi_c^\dagger \ell_L) - \frac{1}{2} \left(\bar{\nu}_R^c M_M \nu_R + \bar{\nu}_R M_M^\dagger \nu_R^c \right) \\
&= i\bar{\nu}_R \not{\partial} \nu_R - (\bar{\nu}_L M_\nu \nu_R + \bar{\nu}_R M_\nu^\dagger \nu_L) - \frac{1}{2} \left(\bar{\nu}_R^c M_M \nu_R + \bar{\nu}_R M_M^\dagger \nu_R^c \right) \\
&= i\bar{\nu}_R \not{\partial} \nu_R - \frac{1}{2} \left[\begin{pmatrix} \bar{\nu}_L & \bar{\nu}_R^c \end{pmatrix} \begin{pmatrix} 0 & M_\nu \\ M_\nu^T & M_M \end{pmatrix} \begin{pmatrix} \nu_L^c \\ \nu_R \end{pmatrix} + h.c. \right], \tag{2.13}
\end{aligned}$$

where ν_R^c are the charge conjugates of the right-handed neutrinos, $h.c.$ stands for hermitian conjugate, and Y_ν , M_ν , and M_M are the Yukawa, Dirac mass, and Majorana mass matrices for the neutrinos, respectively.

In the limit $M_M \gg M_\nu$, the combined mass matrix has two distinct sets of eigenvalues: the sterile neutrinos ν_s with masses $m_s \simeq M_M$ and the active neutrinos ν_a with masses $m_a \simeq M_\nu^2/M_M$. The active and sterile neutrinos are related to the left- and right-handed neutrinos by the active-sterile mixing matrix $\theta = M_\nu M_M^{-1}$ as follows

$$\begin{aligned}
|\nu_a\rangle &= \cos \theta |\nu_L\rangle + \sin \theta |\nu_R\rangle \\
|\nu_s\rangle &= -\sin \theta |\nu_L\rangle + \cos \theta |\nu_R\rangle. \tag{2.14}
\end{aligned}$$

In this formulation, the active neutrinos are the observed neutrinos of the SM while the sterile neutrino states are a promising dark matter candidate as they only interact with the SM through neutrino oscillations. Furthermore, the sterile neutrinos must have $m_s \simeq$ keV or else they cannot account for the observed masses of DM-dominated objects without violating the Pauli exclusion principle. Fortunately, this constraint also means that the oscillation rate into active neutrinos is low enough that the sterile neutrino lifetime is longer than the age of the universe. Additionally, the Majorana mass term allows for additional CP-violating phases beyond the Dirac phases discussed in Section 1.6. Astrophysical detection, accelerator production, and neutrinoless double β decay experiments all place constraints on sterile neutrino properties.

2.4 Simplified Models for LHC

Without loss of generality, we assume that dark matter consists of a single Dirac fermion WIMP species χ with mass m_{DM} . In order to observe DM at a hadron collider, there must exist a new mediator particle with mass M_{med} that couples to both SM quarks and χ with couplings g_q and g_{DM} , respectively. In general, this mediator can have any spin structure; for purposes of simplicity, we limit ourselves to the observed mediators in the SM: a spin-0 scalar S , a spin-0 pseudoscalar P , a spin-1 vector V_μ , and a spin-1 axial-vector A_μ (not to be confused with SM photon). The Lagrangians for these possible mediators are

$$\mathcal{L}_S = \frac{1}{2}M_{\text{med}}^2 S^2 + g_{\text{DM}} \bar{\chi} S \chi + g_q \sum_q \bar{q} Y_q S q \quad (2.15)$$

$$\mathcal{L}_P = \frac{1}{2}M_{\text{med}}^2 P^2 + g_{\text{DM}} \bar{\chi} \gamma^5 P \chi + i g_q \sum_q \bar{q} Y_q \gamma^5 P q \quad (2.16)$$

$$\mathcal{L}_V = \frac{1}{2}M_{\text{med}}^2 V_\mu V^\mu + g_{\text{DM}} \bar{\chi} \not{V} \chi + g_q \sum_q \bar{q} \not{V} q \quad (2.17)$$

$$\mathcal{L}_A = \frac{1}{2}M_{\text{med}}^2 A_\mu A^\mu + g_{\text{DM}} \bar{\chi} \gamma^5 \not{A} \chi + g_q \sum_q \bar{q} \gamma^5 \not{A} q, \quad (2.18)$$

where $\{q\}$ and $\{Y_q\}$ are the SM quarks and their associated Yukawa couplings and we have assumed that the coupling g_q is universal to all quarks without any loss of generality. The width of the mediators is determined by the coupling constants and mass of the mediator. Thus, these four models are described by only four parameters in addition to the spin structure of their couplings: $\{g_q, g_{\text{DM}}, m_{\text{DM}}, M_{\text{med}}\}$. For the results shown in this thesis, we fix $g_q = 0.25$ and $g_{\text{DM}} = 1$ to satisfy the narrow width approximation and provide complimentarity to dijet and dilepton searches for new mediators. Meanwhile, we scan the mass parameters m_{DM} and M_{med} between 1-1000 GeV and 10-2000 GeV, respectively.

As the CMS detector is focused on observing particles through electromagnetic and strong interactions (see Chapter 4), the production of DM particles alone does not result in an observable signature in the detector. Instead, we look for events where

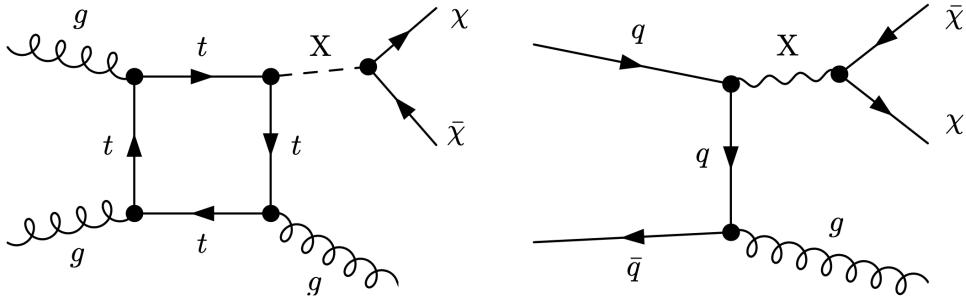


Figure 2-6: Feynmann diagrams for possible dark matter production modes at the LHC, with X denoting the mediator and χ the dark matter particle. The left diagram is most common for scalar and pseudoscalar mediators, while the right diagram is most common for vector and axial mediators. For the right diagram, the gluon can be replaced with any of the EWK gauge boson whereas for the left diagram, other production modes dominate for the EWK gauge bosons. Reprinted from Reference [1].

they are produced in association with a visible SM particle with the resulting signature of the SM particle recoiling against an invisible state. The standard mechanism for producing this final state is for one of the incoming partons to radiate the visible SM particle, usually a quark or a gauge boson, as shown in Figure 2-6. The possible final states split into the categories shown in Table 2.1 with unique final states and interaction strengths.

Table 2.1: Final states of DM production with approximate interaction strength.

Name	Strength	Final State
Monojet	$\mathcal{O}(\alpha_s)$	$j + \chi\bar{\chi}$
Monophoton	$\mathcal{O}(\alpha)$	$\gamma + \chi\bar{\chi}$
Mono-Z	$\mathcal{O}(\alpha)/M_Z^2$	$\ell\ell + \chi\bar{\chi}$

The monojet final state has the highest production rate but also the largest amount of background from SM processes. The Mono-Z final state is the cleanest signature but also has a substantially suppressed production rate due to the mass of the Z boson and the small branching ratio to leptons. The monophoton final state lands in the middle on both metrics: the production rate is $\sim 1/10$ that of the monojet final state but also has fewer backgrounds from SM processes. Additionally, the monophoton state has the “advantage” of being able to distinguish between the spin-0 and spin-1 mediators by the “virtue” of the $gg \rightarrow S\gamma$ and $gg \rightarrow P\gamma$ processes being forbidden by

Furry's theorem. For the bulk of this thesis, we focus on the monophoton final state, saving comparisons against the monojet and mono- Z states for Chapter ??.

2.5 Non-collider Searches

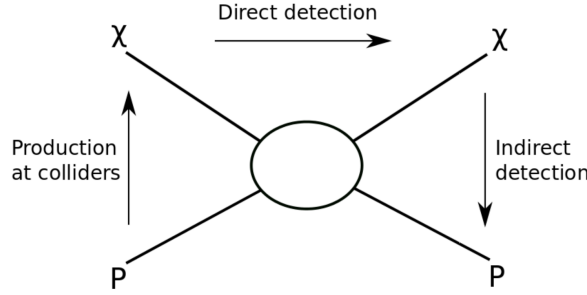


Figure 2-7: Possible dark matter detection channels. Reprinted from Reference [].

The goal of a collider-based search for dark matter is to create pairs of DM candidates through quark-antiquark annihilation, i.e. $q\bar{q} \rightarrow \chi\bar{\chi}$. However, there are other ways you can look at this interaction when attempting to find dark matter, as shown in Figure 2-7. The longest running searches for DM particles have been direct detection searches, where one attempts to observe the scattering of a DM particle off of a heavy nucleus, i.e. $q\chi \rightarrow q\chi$. Another method involves the inverse process utilized at hadron colliders, the observation of SM particles produced in the annihilation of astrophysical DM pairs, i.e. $\chi\bar{\chi} \rightarrow q\bar{q}$. In this section, we shall give a brief overview of the leading experiments for these two approaches.

2.5.1 Direct Detection

Direct detection experiments aim to observe a collision between a DM particle χ and an atomic nucleus N . The typical nuclear recoil for such a collision is in the 1–100 keV range and there are various different technologies that are used to identify the recoiling nucleus, as shown in Figure 2-8. The three main signals are light from a scintillating material, charge from an ionization reaction, and phonons from thermal

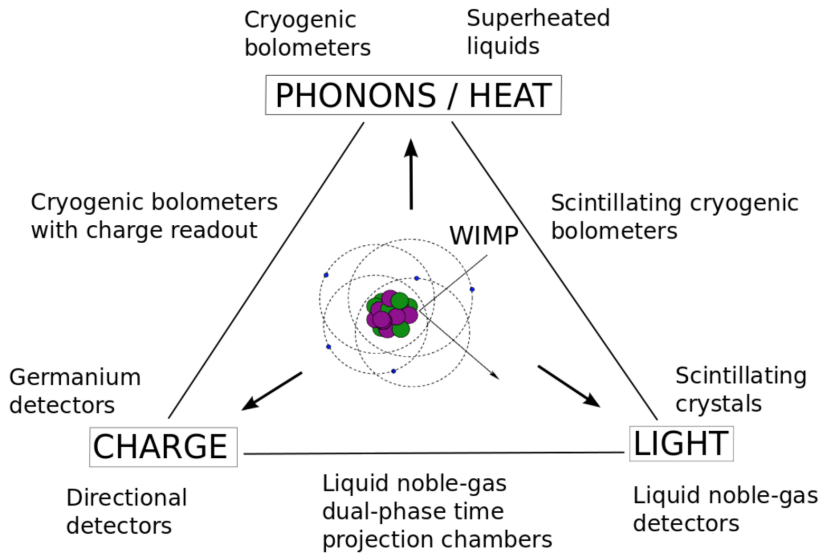


Figure 2-8: Possible signals measured and technologies used in direct detection experiments. Reprinted from Reference [1].

excitations. Many detectors utilize multiple signals in order to enhance background rejection. A final consideration is whether the interaction is spin-independent (SI) or spin-dependent (SD), corresponding to a vector/scalar or axial/pseudoscalar mediator, respectively. The SI DM-nucleus cross-section scales as the number of nucleons squared and thus experiments focusing on SI interactions use materials with a large atomic number. Conversely, the spin-dependent DM-nucleus cross-section depends on the total nuclear spin and experiments focusing on SD interactions use materials with an odd number of nucleons, particularly those with unpaired protons and neutrons. The remainder of this section will discuss three proto-typical direct detection experiments.

The Large Underground Xenon (LUX) experiment is a dual-phase xenon time projection chamber that utilizes both scintillation light and free electrons from ionization to detect nuclear recoils. The active detector volume has 250 kg of ultrapure liquid xenon, a large enough volume that the detector is self-shielding. Odd isotopes make up 47% of naturally occurring xenon, enabling measurements of spin-dependent interactions with approximately half the active detector volume. The latest LUX

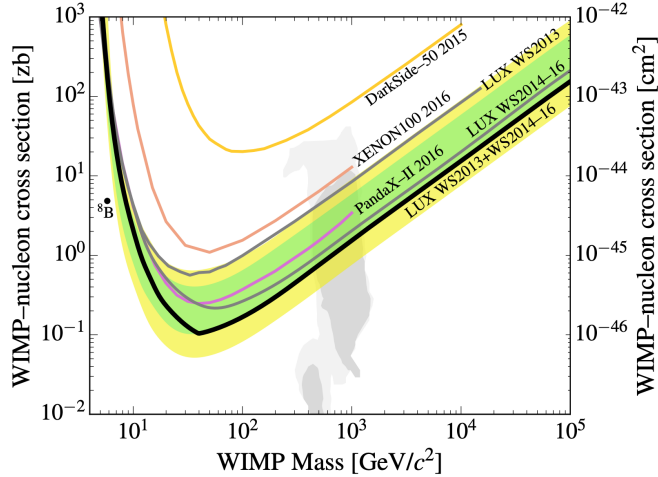


Figure 2-9: Latest SI independent results from the LUX experiment (brazilian flag bands). Reprinted from Reference [1].

results are shown in Figure 2-9.

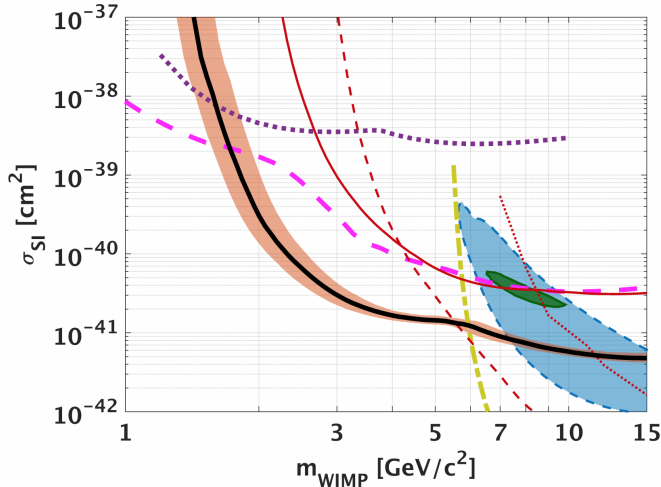


Figure 2-10: Latest SI independent results from the CDMSlite experiment (black line with salmon band). Reprinted from Reference [1].

The CDMSlite experiment uses a cryogenic germanium bolometer that detects phonons and ionization from nuclear recoils. The presence of both signals allows for particle identification, but the most sensitive results only use the phonon signals. CDMSlite is most sensitive to dark matter with masses between 1-10 GeV as shown in Figure 2-10.

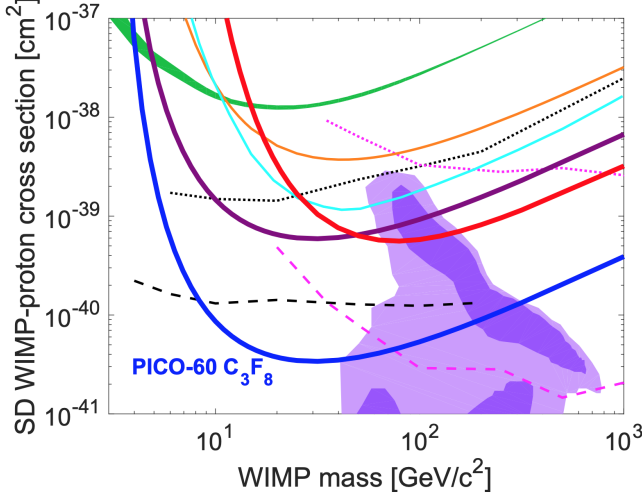


Figure 2-11: Latest SD independent results from the PICO-60 experiment (thick blue line). Reprinted from Reference [].

The PICO-60 experiment uses a bubble chamber filled with C_3F_8 to observe nuclear recoils with a threshold of 13.6 keV. This threshold is high enough to reject backgrounds from minimum ionizing particles while still having sufficient signal efficiency. Furthermore, flourine has exactly one unpaired proton and no unpaired neutrons, greatly enhancing the sensitivity to the proton-coupling SD interactions. The latest results from PICO-60 are shown in Figure 2-11.

2.5.2 Indirect Detection

In Section 2.2, we discussed the process of dark matter annihilation in the early universe and found that the relic density $\Omega_\chi \cdot h^2$ depended on the average annihilation cross section $\langle \sigma_A v \rangle$. In Section 2.3.1, we found that a 100 GeV WIMP particle must have $\langle \sigma_A v \rangle \sim 10^{-26} \text{ cm}^3 \text{ s}^{-1}$ in order to produce the observed relic density. While our calculation in Section 2.2 assumed that the DM number density didn't change appreciably after freezeout, there is still a non-zero annihilation rate of $n_\chi^2 \langle \sigma_A v \rangle / 2$ for dark matter to SM particles. With this decay rate and the observed relic density, there should be $\mathcal{O}(10)$ particles from DM annihilation reaching Earth per year per square meter. Thus, it is possible to learn about dark matter by observing the particle flux near Earth.

While dark matter can decay to a pair of any SM particles, the only ones that live long enough to reach Earth are photons, neutrinos, electrons, positrons, protons, and anti-protons, whether produced directly or from decays of short-lived particles. While it is possible to measure the flux of all of these particles, it is only possible to observe the energy spectrum and source locations of photons and neutrinos as galactic magnetic fields obscure these for the charge particles. Thus, experiments such as the Alpha Magnetic Spectrometer (AMS-02) look for a rise in the positron and anti-proton fractions of the cosmic ray flux to find signs of WIMP annihilation. Similarly, gamma ray telescopes such as the Fermi Large Area Telescope (Fermi-LAT) search for high-energy photons originating from dwarf spheroidal galaxies as they have especially high ratios of dark matter to luminous matter. Both experiments have tentative signals that are yet to be confirmed.

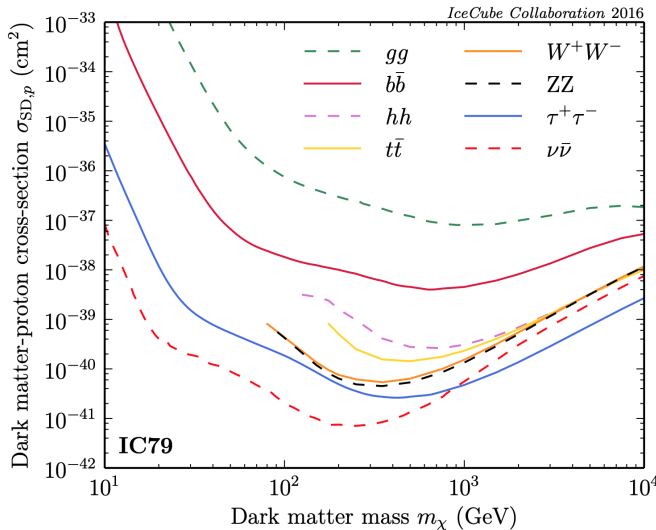


Figure 2-12: Latest SD independent results from the IceCube experiment. Reprinted from Reference [1].

The neutrino channel differs from the other two because it is sensitive to the annihilation of WIMPs that have been gravitationally captured by the sun. While solar WIMPs can decay to any SM particle, only neutrinos are capable of escaping the sun. Furthermore, astrophysical uncertainties are very small for neutrinos originating from the sun versus galactic sources. Additionally, solar WIMPs are in equilibrium, so the annihilation flux depends on the DM-nucleon cross-section instead of the annil-

ihilation cross-section allowing for easy comparison with direct detection experiments. Since the sun consists primarily of hydrogen, observations of solar WIMPs are especially sensitive to spin-dependent processes. The IceCube neutrino observatory is a Cherenkov light detector consisting of a cubic kilometer of Antarctic ice instrumented with 79 strings of photomultiplier tubes. Figure 2-12 shows the latest results from IceCube, with each curves assuming annihilation into a different SM particle pair.

2.6 Summary

Copious astrophysical evidence exists for a non-relativistic non-baryonic type of matter referred to as dark matter that constitutes ~ 27 of the energy of the universe. The favored source for dark matter is a new beyond the Standard Model particle that has weak interactions with photons, baryons, and itself and a relic density of $\Omega_\chi \cdot h^2 = 0.1200 \pm 0.0012$. While other candidates exist, a new weakly-interacting massive particle is a dark matter candidate found in many theories of new physics. Collider, direct detection, and indirect detection searches can all be interpreted in the context of simplified models, which posit a new Dirac fermion DM particle and a massive mediator. The remainder of this thesis focuses on a search for dark matter produced in conjunction with a single photon at the Large Hadron Collider using the Compact Muon Solenoid detector.

Chapter 3

The Large Hadron Collider

3.1 Experimental Apparatus

The Large Hadron Collider (LHC) is a circular proton-proton collider, 27 km in circumference and between 40 and 175 m below the surface, located at the European Organization for Nuclear Research (CERN) on the French-Swiss border near the city of Geneva. Designed to collide protons at a maximum center-of-mass energy $\sqrt{s} = 14 \text{ TeV}$, the LHC has delivered collisions at $\sqrt{s} = 7, 8 \text{ TeV}$ during Run 1 (2010-2012) and at $\sqrt{s} = 13 \text{ TeV}$ during Run 2 (2015-2018). While the LHC is primarily a proton-proton collider, lead (Pb) ion beams of energy of up to 2.8 TeV per nucleon are used to produce lead-lead and proton-lead collisions. In this thesis, we focus exclusively on data recorded from proton-proton collisions during Run 2.

The LHC is the final stage of the CERN accelerator complex depicted in Figure 3-1. Hydrogen atoms are stripped of their electrons and accelerated to an energy of 50 GeV by the LINAC2 linear acceleration. Following this, they are injected into the Booster ring, the Proton Synchrotron (PS), and the Super Proton Synchrotron (SPS) and accelerated to 1.4, 26, and 450 GeV, respectively. After the SPS, the protons are injected into the two counter-circulating rings of the LHC in up to 2808 discrete bunches with a bunch spacing of 25 ns. The two beams intersect in eight places along the LHC with detector experiments CMS, ATLAS, LHCb, and ALICE each located at an intersection point.

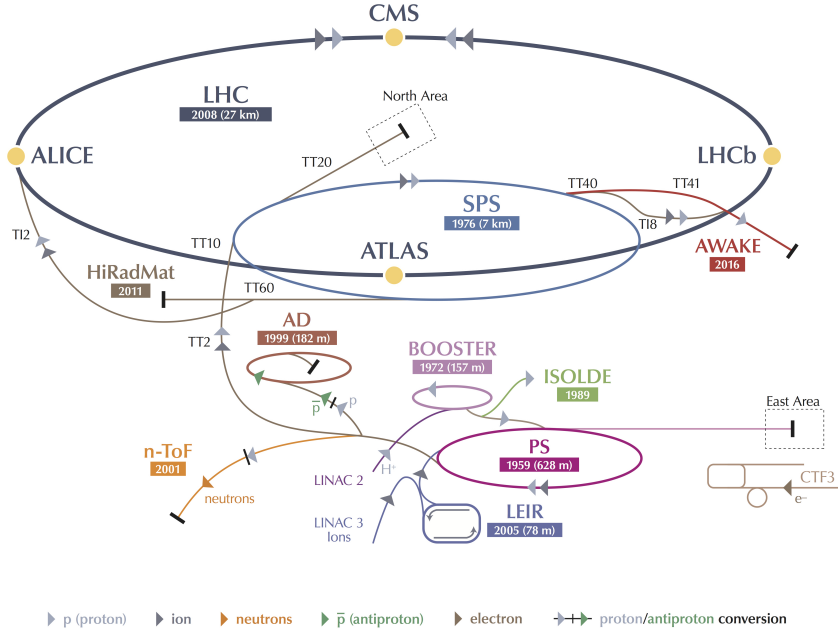


Figure 3-1: A schematic representation of the CERN accelerator complex. The LHC (dark blue) is fed protons by a chain of intermediate accelerators, beginning with LINAC2 (light pink). Reprinted from the CERN Document Server [1].

The LHC is a synchrotron containing 1232 superconducting NbTi dipole magnets measuring 15 m in length, each with a peak dipole field of 8.33 Tesla. There are an additional 492 quadrupole magnets measuring 5-7 m in length which focus the beams in between the dipole magnets. Due to space limitations in the tunnels, the beam pipes are magnetically coupled and the magnets share the same superfluid liquid helium cryostatic system to achieve the 1.9K temperature required to achieve the desired magnetic field strength.

The number of events produced at the LHC is given by

$$N(pp \rightarrow X) = \int dt L(t) \sigma(pp \rightarrow X), \quad (3.1)$$

where σ is the cross section of the process and L is the instantaneous luminosity of the machine given by

$$L = \frac{N_b^2 n_b f_{\text{rev}} \gamma}{4\pi\epsilon\beta^*} \times F, \quad (3.2)$$

where N_b is the number of particles per bunch ($\mathcal{O}(10^{11})$), n_b is the number of bunches per beam, f_{rev} is frequency of revolution, γ is the Lorentz factor of the beam, ϵ is transverse emittance of the beam, β^* is beta function of the beam at the collision point, and F is the geometric luminosity reduction factor due to the crossing angle at the interaction point. The instantaneous luminosity decreases exponentially as a function of time due to N_b and n_b being reduced by collisions. The LHC is designed to deliver an initial instantaneous luminosity of $\mathcal{O}(10^{34}) \text{ cm}^{-2} \text{ s}^{-1}$, achieved by having multiple inelastic proton-proton interactions per bunch crossing known as pileup.

As all known cross sections are time-independent, the total number of events is directly proportional to the integrated luminosity given by

$$L_{\text{int}} = \int_0^T dt L(t) = L(0)\tau_L (1 - e^{-T/\tau_L}), \quad (3.3)$$

where T is the time since starting collisions, $L(0)$ is the initial instantaneous luminosity, and $\tau_L \approx 15$ the characteristic beam loss timescale for the LHC. The total luminosity delivered by the LHC and recorded by CMS during the 2016 is shown in Figure 3-2.

3.2 Collider Phenomenology

The proton is a composite particle consisting of valence quarks, sea quarks, and gluons, collectively referred to as partons. When colliding protons at the LHC, we are actually interested in the inelastic scattering of a pair of partons from the incident protons. Each parton a, b carries a fraction of the momentum of the incoming proton $x_{a,b}$ following the particle-dependent parton distribution functions (PDFs) $f_{a,b}$. The differential cross section for $2 \rightarrow N$ parton scattering process is given by

$$d\sigma(ab \rightarrow \{c_i\}) = \frac{(2\pi)^4}{2s} \left(\prod_i \frac{d^3 p_i}{(2\pi)^3} \right) \cdot \delta^4 \left(k_a + k_b - \sum_i p_i \right) \cdot |\mathcal{M}(ab \rightarrow \{c_i\})|^2 \quad (3.4)$$

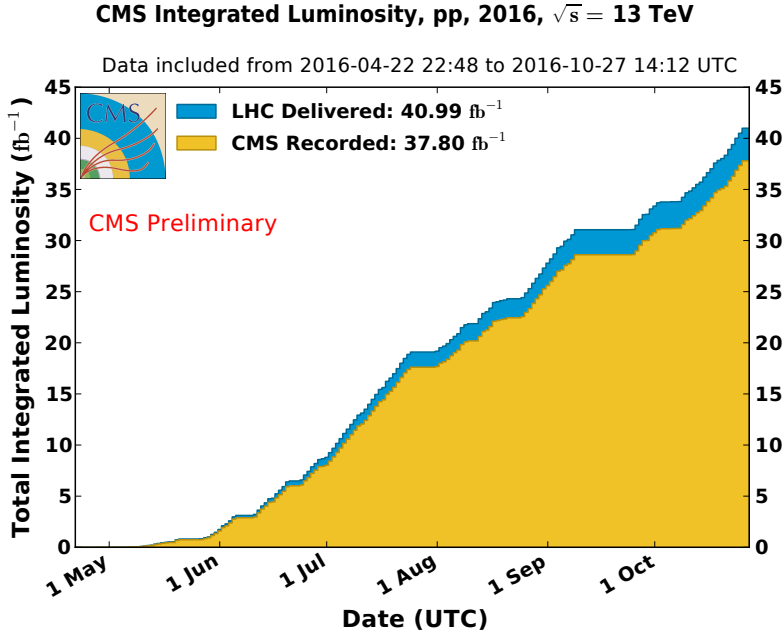


Figure 3-2: The total integrated luminosity of the LHC during proton-proton collisions during 2016.[] While a total luminosity of 41 fb^{-1} was collected, only a subset during which the detector operated optimally is used in this thesis. This corresponds to 36 fb^{-1} of data.

where $k_{a,b} = x_{a,b}\sqrt{s}$ are the momenta of the incoming partons, $\{p_i\}$ are the momenta of the outgoing partons $\{c_i\}$, and \mathcal{M} is the matrix element of the process.

This parton level scattering, called the hard scattering process, is perturbatively calculable through standard QFT methods. However, the hard scattering does not include any effects related to the PDFs of the incoming partons or the decay and hadronization of the outgoing partons into the final state particles (called the parton shower), both of which involve non-perturbative aspects of QCD. Fortunately, the collinear factorization theorem states that the probability of obtaining the final state $X(\Theta)$ from a hadron collision can be calculated as the product of the probability that specific partons a, b are involved in the interaction, the probability for the hard scattering to produce outgoing partons $\{c_i\}$, and the formation of final state hadrons from these outgoing partons. The factorization process is not unique and requires the choice of an arbitrary energy scale μ_F , which defines a lower bound for interactions to be considered part of the hard scattering.

Including the effects from PDFs and parton showering (PS), the general cross

section for $pp \rightarrow X(\Theta)$ is

$$\frac{d\sigma}{d\Theta}(pp \rightarrow X(\Theta)) = \sum_{a,b} \int dx_a f_a(x_a, \mu_F) \cdot dx_b f_b(x_b, \mu_F) \times d\sigma(ab \rightarrow \{c_i\}) \times D(\{c_i\} \rightarrow X(\Theta)) \quad (3.5)$$

where the sum is over the initial state partons and D is the fragmentation function that describes parton shower process resulting in the observed final state. The following sections discuss the simulation of the three main elements of Equation 3.5: the parton distribution functions f_a , the hard scattering cross section $d\sigma$, and the parton shower and hadronization processes that contribute to the fragmentation function D .

3.2.1 Parton Distribution Functions

Due to soft collinear emissions from the partons, the behavior of the parton distribution functions depends on the factorization scale. Denoting the gluon PDF as $g(x, \mu_F)$ and the PDF for quark flavor i as $q_i(x, \mu_F)$, the analytic behavior of the PDFs is given by the DGLAP evolution equations

$$\mu_F \frac{d}{d\mu_F} \begin{pmatrix} q_i(x, \mu_F) \\ g(x, \mu_F) \end{pmatrix} = \frac{\alpha_s}{2\pi} \int_x^1 \frac{dy}{y} \begin{pmatrix} P_{qq}(x/y) & P_{qg}(x/y) \\ P_{gq}(x/y) & P_{gg}(x/y) \end{pmatrix} \begin{pmatrix} q_i(y, \mu_F) \\ g(y, \mu_F) \end{pmatrix} \quad (3.6)$$

where y is the fraction of momentum carried by initial parton and the P matrix elements are the splitting kernels defined by

$$\left| \begin{array}{l} P_{qq}(z) = \frac{4}{3} \left(\frac{1+z^2}{1-z} \right) \\ P_{qg}(z) = \frac{4}{3} \left(\frac{1+(1-z)^2}{z} \right) \\ P_{gq}(z) = \frac{1}{2} (z^2 + (1+z)^2) \\ P_{gg}(z) = 6 \left(\frac{1-z}{z} + \frac{z}{1-z} + z(1-z) \right). \end{array} \right. \quad (3.7)$$

The DGLAP equations cannot be solved analytically at a fixed scale. Instead, parameterized functional forms are fitted to data from many experiments. The results presented in this thesis use the NNPDF3.0 PDF set provided by the NNPDF collaboration.

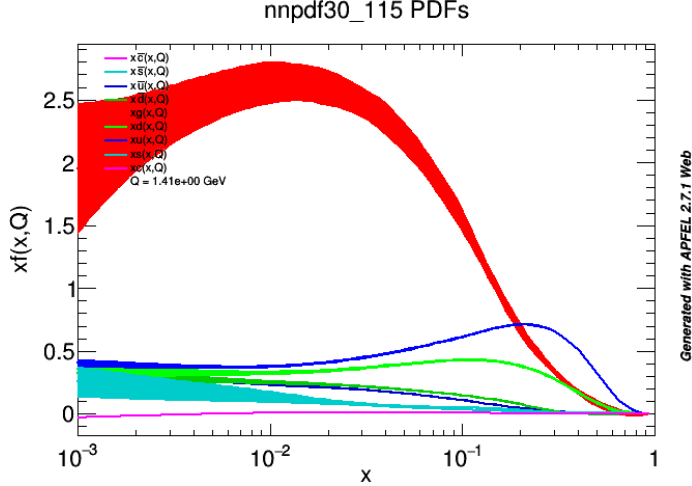


Figure 3-3: The various quark and gluon PDFs for the proton, as a function of momentum fraction x . The specific PDF set is the NNPDF3.0 118 NLO PDF set.

oration. Figure 3-3 shows the quark and gluon PDFs for the proton. As $x \rightarrow 0$, the gluon fraction dominates while as $x \rightarrow 1$, the up-quark fraction $u(x, \mu_F)$ approaches $\frac{2}{3}$, the down-quark fraction $d(x, \mu_F)$ approaches $\frac{1}{3}$, and the gluon and sea quark fractions approach zero.

3.2.2 Hard Scattering

The hard scattering process is simulated using Monte Carlo generators that sample events with probability proportional to the phase space and matrix element. For the results contained in this thesis, the primary hard interaction is simulated using the MADGRAPH5 aMC@NLO generator, which can simulate to leading order (LO) in EW vertices and up to next-to-leading order (NLO) in QCD vertices.

3.2.3 Parton Shower

The parton shower is a sequence of splittings where one outgoing parton c_i emits a second soft and/or collinear particle j . Each splitting has an associated splitting kernel $P_{c_i \rightarrow c_i j}(z)$, where z is the momentum fraction carried by the initial parton. The allowed QCD splittings are $q \rightarrow qg$, $g \rightarrow q\bar{q}$, and $g \rightarrow gg$ and the allowed QED

splittings are $f \rightarrow f\gamma$ and $\gamma \rightarrow f\bar{f}$. The kernels associated with these splittings are

$$\left| \begin{array}{l} P_{q \rightarrow qg}(z) = \frac{4}{3} \left(\frac{1+z^2}{1-z} \right) \\ P_{g \rightarrow q\bar{q}}(z) = \frac{1}{2} (z^2 + (1-z)^2) \\ P_{g \rightarrow gg}(z) = 3 \left(\frac{(1-z)(1-z)^2}{z(1-z)} \right) \end{array} \right| \left| \begin{array}{l} P_{f \rightarrow f\gamma}(z) = Q_f^2 \left(\frac{1+z^2}{1-z} \right) \\ P_{\gamma \rightarrow f\bar{f}}(z) = N_C Q_f^2 (z^2 + (1-z)^2) \end{array} \right. \quad (3.8)$$

where Q_f is the charge of the fermion and N_C is the number of color states the fermion can occupy (3 for quarks and 1 for leptons). The cross section of a splitting is given by

$$\frac{d\sigma(ab \rightarrow \{c_i\}j)}{d\sigma(ab \rightarrow \{c_i\})} = P_{c_i \rightarrow c_ij}(z) \cdot \frac{\alpha_s}{2\pi} \cdot \frac{d\theta}{\theta} \cdot dz \quad (3.9)$$

where θ is the opening angle between c_i and j . These cross sections diverge as $\theta \rightarrow 0$ and $z \rightarrow 1$, meaning bare quarks producing many soft and collinear gluons. Then, these gluons further split to gg and $q\bar{q}$ pairs, which in turn emit even more soft and collinear gluons and photons. This process continues until the energy of the outgoing partons reaches Λ_{QCD} at which point hadronization occurs.

3.2.4 Hadronization

The QCD potential between two quarks can be approximated as $V(\vec{r}) \approx \kappa r$, where κ has been measured to be approximately 1 GeV/fm. The linear behavior of the potential is due to the attractive interactions between the gluons mediating the quark-quark interaction which confine the color field between the quarks into a tube 1 fm in diameter. As the quarks separate, the energy contained in this gluon tube increases linearly until it exceeds the mass of a $q\bar{q}$ pair. At this point, a new $q\bar{q}$ pair pops into existence through a quantum mechanical tunneling process, splitting the tube in two. Due to the difference in quark masses, only up, down, and strange quarks are produced, in a 10:10:3 ratio. This process continues until the energy of all the quarks have low enough energy to combine into stable hadrons.

The above procedure is a qualitative description of the Lund string model used. The Pythia event generator models hadronization using the Lund string model as

well as the parton shower effects described in the previous section. All results in this thesis use the Pythia 8.2 program to simulation the parton shower and hadronization processes.

Chapter 4

The CMS Detector

The Compact Muon Solenoid (CMS) detector is one of two hermetic, general purpose detectors at the Large Hadron Collider. The original motivation for the experiment was the discovery of the Higgs boson by observing its decays to photons, electrons, and muons. Towards this end, the detector was built to fulfill the following goals:

- Unambiguous charge identification of muons with momenta up to 1 TeV
- 1 GeV mass resolution on 100 GeV pairs of muons, electrons, and photons
- Efficient triggering and tagging of τ lepton and b quark decays
- Good resolution on the hadronic energy and missing transverse energy
- Sufficient time resolution to deal with 40 MHz of collisions

The CMS detector consists of four main subdetectors: the inner trackers, the electromagnetic calorimeter (ECAL), the hadronic calorimeter (HCAL), and the muon chambers. The first three are within the field volume of the eponymous 3.8 T superconducting NbTi solenoid magnet while the muon chambers are embedded in the return yoke of the magnet. Additionally, there is an online triggering system to reduce readout from 40 MHz to $\mathcal{O}(1)$ kHz for prompt reconstruction.

The overall layout of the CMS detector is shown in Figure 4-1. The CMS detector has a weight of 12500 tons, a length of 22 m, a diameter of 15 m, and a cylindrical

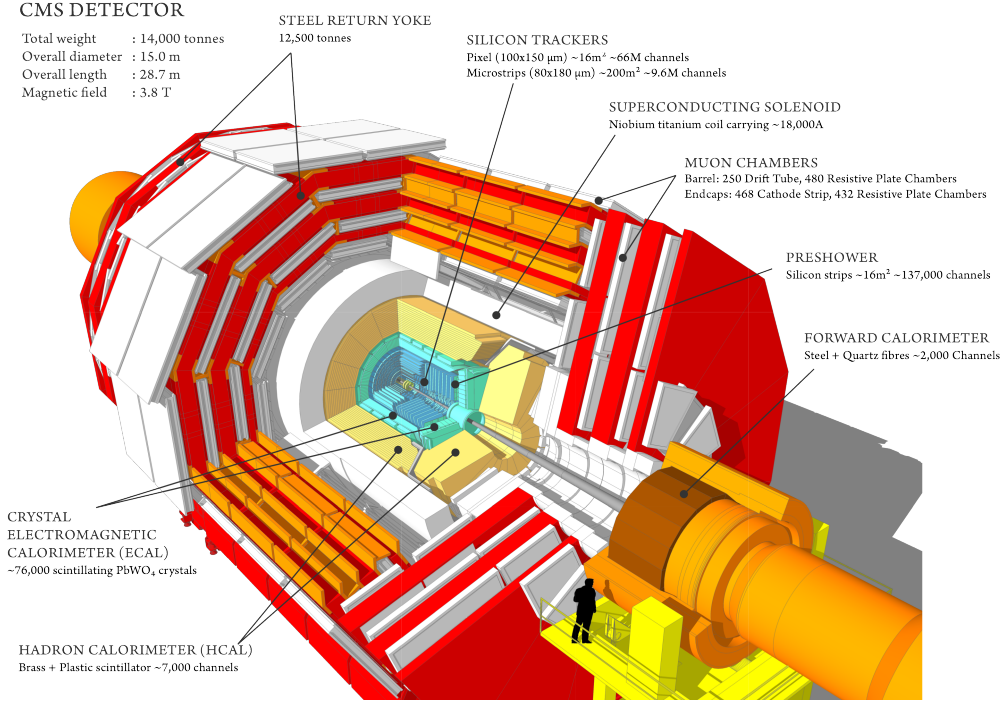


Figure 4-1: A cutaway view of the CMS detector. The labels identify the solenoid as well as the different subdetectors and their components. Reprinted from Reference [1].

geometry with concentric barrel shaped detectors in the central region and disc shaped detectors in the forward region. The following coordinate system is used when working with the CMS detector:

- distance z along the beam axis
 - $z = 0$ at the center of the detector
 - positive corresponds to counter-clockwise as seen from the sky
- distance r from the beam axis
- polar angle θ measured with respects to the positive z -axis
- azimuthal angle ϕ in the plane orthogonal to the beam axis

In addition to these four main coordinates, we define the right-handed cartesian x and y coordinates perpendicular to the beam axis, with the positive x -axis pointing

from the center of the detector to the center of the LHC ring and the positive y -axis pointing upwards.

The four-momentum of a particle is $p = (p_x, p_y, p_z, E)$ in the cartesian basis and a particle of mass m produced at rest in the center of the detector has $p = (0, 0, 0, m)$. While the momenta along the beam axis of the two incoming protons are equal, the momenta of the incoming partons involved in the hard scattering often are not as discussed in Section 3.2. Thus, we define two kinematic quantities that are Lorentz-invariant with respect to a boost along the beam axis: the transverse momentum $\vec{p}_T = p_x \hat{x} + p_y \hat{y}$ with magnitude $p_T = \sqrt{p_x^2 + p_y^2}$ and the pseudorapidity $\eta = -\ln \tan \theta/2$.

In terms of p_T , η , and ϕ , we have the following expressions for our cartesian variables: $p_x = p_T \cos \phi$, $p_y = p_T \sin \phi$, $p_z = p_T \sinh \eta$, and $E = p_T \cosh \eta$, with the last equality assuming the mass of the particle is negligible compared to its momentum. In terms of our Lorentz-invariant coordinates, the four-momentum of a given particle is $p = (p_T, \eta, \phi, E)$. Additionally, the spatial separation of two particles is given by $\Delta R = \sqrt{(\Delta\phi)^2 + (\Delta\eta)^2}$ and the fiducial acceptance of the CMS detector is from $0 \leq \phi < 2\pi$ and $-5 \leq \eta \leq 5$.

4.1 Inner Trackers

Closest to the interaction point, the inner trackers identify charged particles and measures their momenta. Additionally, high resolution tracks are used to identify primary and secondary vertices. The magnetic field in the tracker volume is uniform with strength 3.8 T and field lines parallel to the beam direction. The tracker volume extends to 1.2 m in r and 2.9 m in z , providing coverage for $|\eta| < 2.5$, and is instrumented with silicon pixels and strips. Each silicon sensor is a p - n semiconductor junction with a bias voltage applied. When a charged particle passes through the depletion region of the junction, electron-hole pairs are produced and collected by the readout electronics. A schematic of the inner tracker system is shown in Figure 4-2.

The 66 million individual pixel sensors, each measuring $285 \mu\text{m} \times 100 \mu\text{m} \times 150 \mu\text{m}$ in $r \times r\phi \times z$, are arranged into seven layers: three cylindrical barrels at $r =$

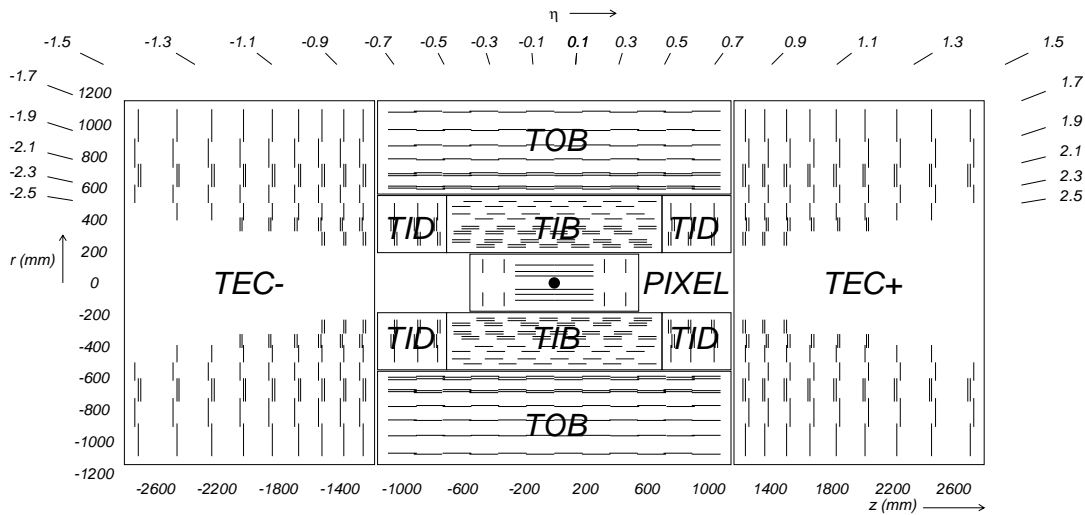


Figure 4-2: A schematic view of the CMS inner tracker system. Silicon pixel and strip detectors are shown. The volumes labeled TIB, TID, TOB, and TEC are all strip trackers. The double lines indicate back-to-back modules that deliver stereo hits. Reprinted from Reference [1].

4.4, 7.3, 10.2 cm and two bi-layer endcap annuli at $z = \pm 34.5, \pm 46.5$ cm. Due to the geometry of the pixel detector, tracks typically cross the sensor at a 20° angle, leading to the charge deposit from a single track to be shared among multiple pixels in the same layer. The exact position of a particle in each layer is determined by interpolating the signals from multiple adjacent pixels with an analog pulse height greater than a tuneable read-out threshold. Thus, each pixel hit is localized to an area of $\sim 15\text{ }\mu\text{m} \times 20\text{ }\mu\text{m}$ in $r\phi \times z$, providing a much higher spacial resolution than the raw pixel spacing.

The pixels are surrounded 9.3 million silicon strips measuring $10\text{ cm} \times 80\text{ }\mu\text{m}$ arranged in ten cylindrical layers in the barrel and twelve disks in each endcap. The Tracker Inner Barrel (TIB) consists of the first four layers and extends from 20 cm to 55 cm in the radial direction while out six layers constitute the Tracker Outer Barrel (TOB) with an outer radius of 116 cm and extent in $|z|$ of 118 cm. The remaining area in the barrel is covered by the Tracker Inner Disk (TID), consisting of the three disks located from 80 to 90 cm in $|z|$. The Tracker EndCaps (TEC) have nine disks each and cover the region $124\text{ cm} < |z| < 282\text{ cm}$.

The majority of the strips are oriented perpendicular to the ϕ direction: parallel to the beam pipe in the barrel region and radially aligned in the endcap region. The strip pitch varies from 80 to 184 μm with the smallest pitch in the innermost layer. This detector geometry provides good resolution in the r - ϕ plane for barrel and the z - ϕ plane for the endcap but little information on the orthogonal directions. To compensate for this, one third of the strips are double-layered with a stereo angle of 100 mrad between the layers. Matching hits between adjacent layers enables a measurement of the z and r coordinates in the barrel and endcap, respectively. The final spacial resolution is 10-50 μm in the direction perpendicular to the strips and 100-530 μm in the parallel direction on the stereo modules.

4.2 Electromagnetic Calorimeter

The electromagnetic calorimeter (ECAL) is a homogeneous, hermetic calorimeter composed of 76,000 lead tungstate (PbWO_4) crystals. High density (8.3 g/cm³) lead tungstate was chosen due to its radiation hardness, fast scintillation decay time constant of 25 ns, small Moliere radius $r_M = 21.9$ mm, and short radiation length $X_0 = 8.9$ mm. All of these factors combine to enable the construction of a compact calorimeter with high granularity and excellent energy resolution.

Figure 4-3 shows the layout of the ECAL. The central barrel region (EB) has 61200 crystals arranged in a 170×360 η - ϕ grid (0.0174 \times 0.0174 granularity) with a coverage up to $|\eta| = 1.44$ while the two endcap annuli (EE) each have 7324 crystals organized in a x - y grid with coverage in the range $1.479 < |\eta| < 3.0$. Each crystal in the EB has a truncated pyramidal shape with a length of 230 mm, a 22 mm \times 22 mm front-face cross-section, and a 26 mm \times 26 mm rear-face cross-section while a crystal in the EE has a cuboid-like shape with a length of 220 mm, a 28.6 mm \times 28.6 mm front-face cross-section, and a 30 mm \times 30 mm rear-face cross-section. The cross-sectional area of approximately one Moliere radius and length of approximately 25 radiation lengths allows just a few crystals to contain the entire transverse and longitudinal development of the shower. To reduce the likelihood of the primary photon or electron

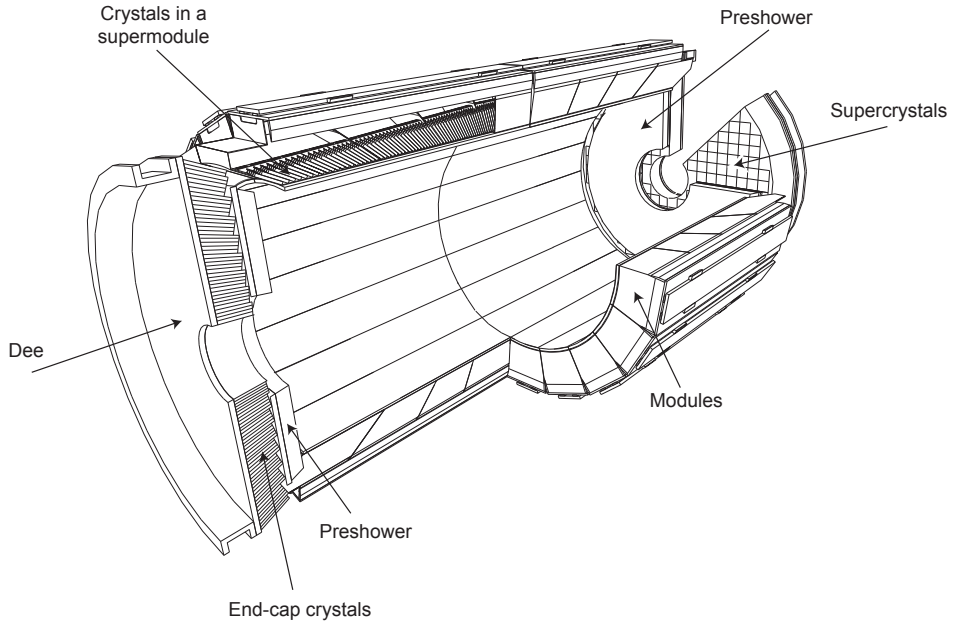


Figure 4-3: The layout of the CMS electromagnetic calorimeter. The barrel and endcap calorimeters are shown. The pre-shower detector sits in front of the endcaps. Reprinted from Reference [1].

emerging from the hard scattering depositing most of its energy in passive material, the crystals do not point directly to the interaction region.

The interactions between the 3.8 T magnetic field and the geometries of the ECAL lead to the selection of different photosensors in the barrel and endcaps. In the endcaps, the magnetic field is parallel to the path of the photoelectrons and has a negligible effect on the gain, while in the barrel, the magnetic field is perpendicular and reduces the gain by a factor proportional to the distance traveled by the photoelectrons. Thus, in the barrel, solid-state reverse-structure avalanche photodiodes (APDs) with a depletion layer of $6.0 \pm 0.5 \mu\text{m}$ are used, while photomultiplier tubes with a single gain stage and a very fine copper mesh anode called vacuum phototriodes (VPTs) are used in the endcaps. Two APDs with an active area of 25 mm^2 are glued to the rear of each crystal in the barrel while only one VPT with an active area of 280 mm^2 is needed per crystal in the endcap. The APDs and VPTs amplify the initial signal of approximately 4.5 photoelectrons per MeV of energy deposit per

crystal by a factor of 50 and 10, respectively.

The small signals from the photodetectors are shaped and amplified in the Multi-Gain Preamplifier (MGPA) and a 12-bit analog-to-digital converter (ADC) samples the pulse every 25 ns. Each output voltage pulse has a length of approximately 300 ns, with the maximum at approximately 75 ns and a slow decay afterwards. The MGPA has multiple gain modes of 12, 6, and 1, and the gain chosen for the output decreases once the signal has saturated the previous gain setting. After the pulse falls below the saturation threshold, the lower gain setting is maintained for the next five samples. This mechanism provides a dynamic signal range from a few MeV to a maximum of 1.5 TeV in the barrel and 3.1 TeV in the endcaps.

The energy resolution of the ECAL was measured using an electron beam to be

$$\frac{\sigma_E}{E} = \frac{2.8\%}{\sqrt{E/\text{GeV}}} \oplus \frac{12\%}{E/\text{GeV}} \oplus 0.3\%, \quad (4.1)$$

where E is the energy of the incident particle and the three terms on the RHS are the stochastic, noise, and constant terms, respectively. The stochastic term is dominated by event-to-event fluctuations in the lateral shower containment and a photo-statistics contribution of 2.1%. Electronic and digitization noise drive the noise term while the constant term comes from a non-uniform longitudinal light collection and intercalibration errors.

4.2.1 Preshower Detector

At high momenta and high $|\eta|$, the two photons from a π^0 decay can merge into a single ECAL crystal due to the large boost in the z -direction of the initial state. By forcing the initiation of an electromagnetic shower in a region with high spacial resolution in front of the ECAL endcaps, the preshower detector can differentiate between one- and two-photon deposits in the region $1.6 < |\eta| < 2.5$. The preshower detector consists of two alternating layers of passive lead absorbers and active silicon strip sensors. The first (second) lead layer is two (one) radiation lengths thick and the subsequent sensor plane has vertical (horizontal) strips of 6 cm length and 1.9 mm

pitch. The silicon strips resolve the shower with a resolution of $\mathcal{O}(1\text{--}10)$ mm, enabling the disambiguation of two nearly collinear photons and the identification of π^0 decays.

4.3 Hadronic Calorimeter

The hadronic calorimeter (HCAL) is a set of four heterogenous calorimeters that provide hermetic coverage when combined: the barrel calorimeter (HB) covering $|\eta| < 1.3$, the endcap calorimeter (HE) covering $1.3 < |\eta| < 3$, the outer calorimeter (HO) covering $|\eta| < 1.3$, and the forward calorimeter (HF) covering $3 < |\eta| < 5$. The region covering $|\eta| < 3$ shall be referred to as the central HCAL. The granularity of the HCAL in $\eta\text{-}\phi$ is 0.087×0.087 for $|\eta| < 1.6$, 0.17×0.17 for $1.6 < |\eta| < 3.0$, and 0.175×0.175 for $3 < |\eta| < 5$. The layout of the HCAL is shown in Figure 4-4.

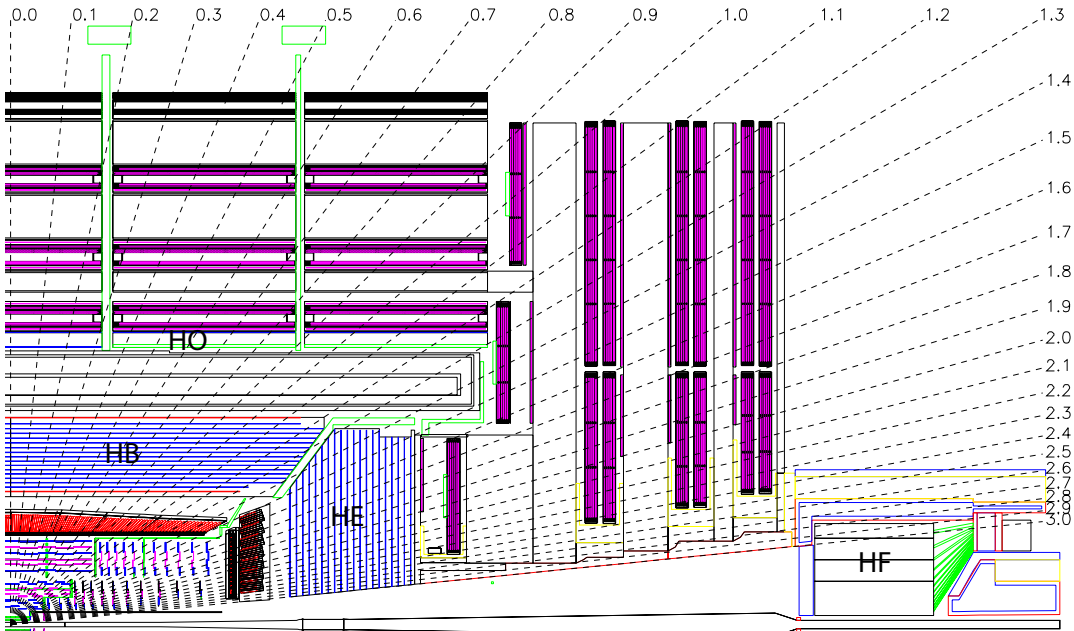


Figure 4-4: The layout of the CMS hadronic calorimeter. The barrel, endcap, outer, and forward calorimeters are shown and labeled. The muon chambers are shown but not labeled. The dashed lines denote different values of pseudorapidity. Reprinted from Reference [1].

The HB and HE are sampling calorimeters with 16 and 17 thin plastic scintillator

layers, respectively, interleaved with thick absorber layers made of a non-magnetic brass alloy with an interaction length $\lambda_I = 1.5$ cm. The layers range in thickness from 40 to 75 mm providing a total absorber depth ranging from a minimum of 5.82 λ_I at $|\eta| = 0$ to a maximum of 10.6 λ_I at $|\eta| = 1.3$ in the barrel and approximately nine interaction lengths throughout the endcaps, with the ECAL contributing another interaction length worth of material. The dimensions of the HB and HE are determined by the requirement that they reside between the ECAL and the solenoid. To circumvent this constraint, an additional layer of scintillator located in the return yoke of the magnet, the HO, utilizes the solenoid material as an additional interaction length of absorber. Hybrid photodiodes (HPDs) are used to read out the scintillator light in the HB and HE while silicon photomultipliers (SiPMs) are used in the HO.

Located 11 meters from the interaction point, the HF is a sampling calorimeter covering the region of phase-space with high pseudorapidity. Since the particle flux here is much higher than in the central region, the HF uses radiation-hard steel absorber instrumented with two sets of scintillating quartz fibers. Charged particles produced by showers in the steel traverse the quartz fibers and emit Cherenkov radiation that is recorded by photomultiplier tubes. To distinguish hadrons from photons and electrons, the second set of fibers starts at a depth of 22 cm.

Since hadrons interact with the ECAL as well as the HCAL, the energy resolution of the detectors must be considered in tandem in the central region. Using a charged particle test beam, the combined ECAL+HCAL energy resolution was measured to be

$$\frac{\sigma_E}{E} = \frac{0.847}{\sqrt{E/\text{GeV}}} \oplus 0.074 \quad (4.2)$$

and the standalone HF energy energy resolution is

$$\frac{\sigma_E}{E} = \frac{1.98}{\sqrt{E/\text{GeV}}} \oplus 0.09. \quad (4.3)$$

4.4 Muon Chambers

The outer most components of CMS are the muon triggering, identification, and detection chambers. These muon detectors are interleaved with the steel return yoke of the magnet resulting in a characteristic *S*-shape for the muon trajectories due to the reversal of magnetic field direction across the solenoid. Signal purity in the muon detectors is high as hadrons, electrons, and photons are stopped by the calorimeters while muons are minimum ionizing particles (MIPs) that lose little energy while traversing the detector. Taking advantage of the large detector volumes required by the outer solenoid radius of 3.5 m, three types of gas ionization chambers are used: drift tubes (DTs) in the barrel covering $|\eta| < 1.2$, cathode strip chambers (CSCs) in the endcaps covering $0.9 < |\eta| < 2.4$, and resistive plate chambers (RPCs) in both covering $|\eta| < 2.1$. The layout of the muon detectors is shown in Figure 4-5.

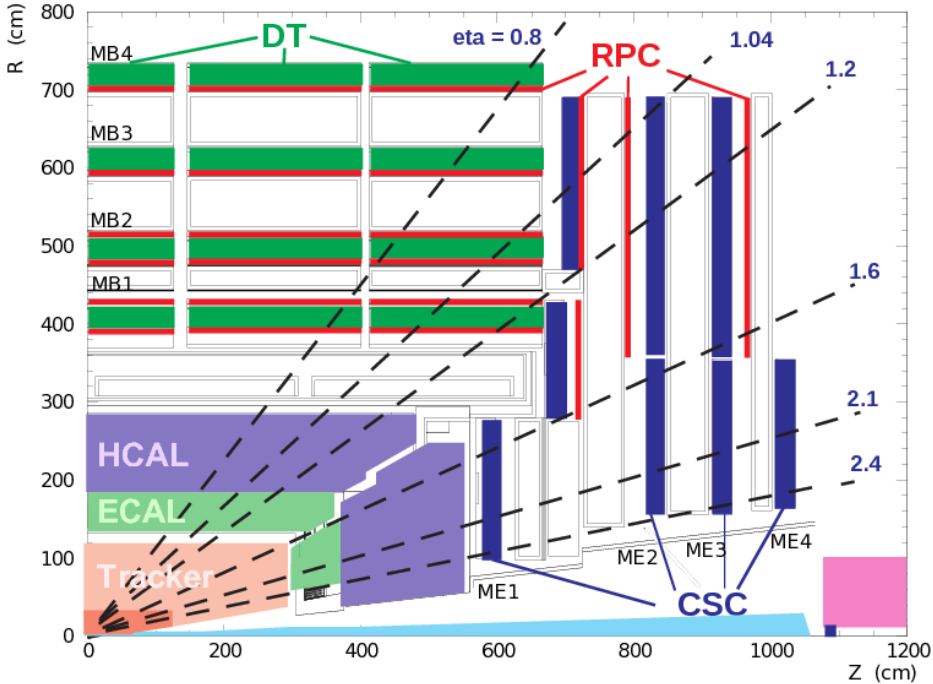


Figure 4-5: The layout of the CMS muon chambers. The four DT stations are labeled MB1-MB4, the four CSC stations are labeled ME1-ME4, and the RPC stations are shown in red. The dashed lines denote different values of pseudorapidity. Reprinted from Reference [1].

The DT chambers consist of rectangular drift cells with transverse dimensions of $42\text{ mm} \times 13\text{ mm}$ filled with a 85:15 Ar/CO₂ mix and a gold/steel anode wire held at a voltage of 3.6 kV. The maximum drift time per cell of 400 ns provides a spatial resolution of approximately 250 μm . A single chamber is made out of superlayers which are in turn made out of four individual cells for a combined resolution of 100 μm . The chambers are arranged into four 2.4 m thick dodecagonal rings called the muon barrel stations. All four stations have two superlayers per chamber that measure position in the $r\text{-}\phi$ plane while the chambers in the inner three stations have an additional superlayer that measures position in the $r\text{-}z$ plane. Together, the four muon stations and iron yokes form a wheel with one between the solenoid and the first iron layer, two in between the yokes, and one outside. The outer barrel is composed of five wheels in total.

Due to their faster response time and better spatial resolution, CSCs are used to handle the higher muon and background fluxes in the endcap region. Each CSC is filled with a 50:40:10 CO₂/Ar/CF₄ mix and instrumented with 80 cathode strips held at voltages of 2.9–3.6 kV relative to the gold-plated tungsten anode wires. The strips run radially outward to measure position in the $r\text{-}\phi$ plane while the wires run perpendicular measure the η and beam-crossing time of the muons. The four muon stations in each endcap are made of CSCs arranged into annuli oriented perpendicular to the beam axis and interspersed between the flux return plates. The three inner stations have multiple annuli with smaller ones fitting inside the larger ones while the fourth station only has one close to the beamline.

An RPC is a parallel-plate double-gap chamber with a time resolution of one nanosecond and a poor spatial resolution. The RPCs are interspersed throughout the DT and CSCs to provide an independent muon trigger system that can identify the correct bunch crossing time.

4.5 Online Trigger System

To achieve an instantaneous luminosity of $\mathcal{O}(10^{34}) \text{ cm}^{-2} \text{ s}^{-1}$, the LHC has bunch crossings every 25 ns for a total data rate of 40 MHz, much higher than the 100 kHz readout rate for the detector and the $\mathcal{O}(1)$ kHz data reconstruction and tape writing rates. Fortunately, uninteresting elastic scattering and QCD inelastic scattering events dominate the approximately $100 \mu\text{b}$ total proton-proton cross-section at the LHC. Meanwhile, most new physics processes have a predicted on the order of picobarns or femtobarns and even the highest rate SM EWK cross-sections are $\mathcal{O}(10)$ nb, so not every event needs to be readout, reconstructed, and written to tape.

A two-stage trigger system selects the events to keep for permanent storage and analysis. The Level 1 hardware-based trigger (L1) selects interesting events based on incomplete detector information to reduce readout and computation times. Events selected by the L1 trigger are fully readout and passed to the high level software-based trigger (HLT) where the full event is reconstructed using the data acquisition system (DAQ), a computing farm with over 20k CPU cores. Events selected by the HLT are sent to the offline computing resources for full reconstruction followed by storage on disk and tape.

The L1 trigger uses field programmable gate arrays (FPGAs) and application specific integrated circuits (ASICs) to make decisions within $4 \mu\text{s}$ of each collision. Each subdetector module has a hardware trigger that reconstructs objects called trigger primitives (TPs). In the two calorimeters, clustered energy deposits from each tower are sent to a regional calorimeter trigger (RCT) which correlates the information from adjacent towers and between the ECAL and HCAL into electron, photon, and jet candidates. The outputs from the RCT are passed to the global calorimeter trigger (GCT) which computes global event variables such as the total transverse energy, the hadronic transverse energy, and the momentum imbalance. Muon track candidates are produced from a simple segment-finding and tracking algorithm in each of the three types of muon chambers. The global muon trigger (GMT) receives the candidates and combines them with information from the GCT

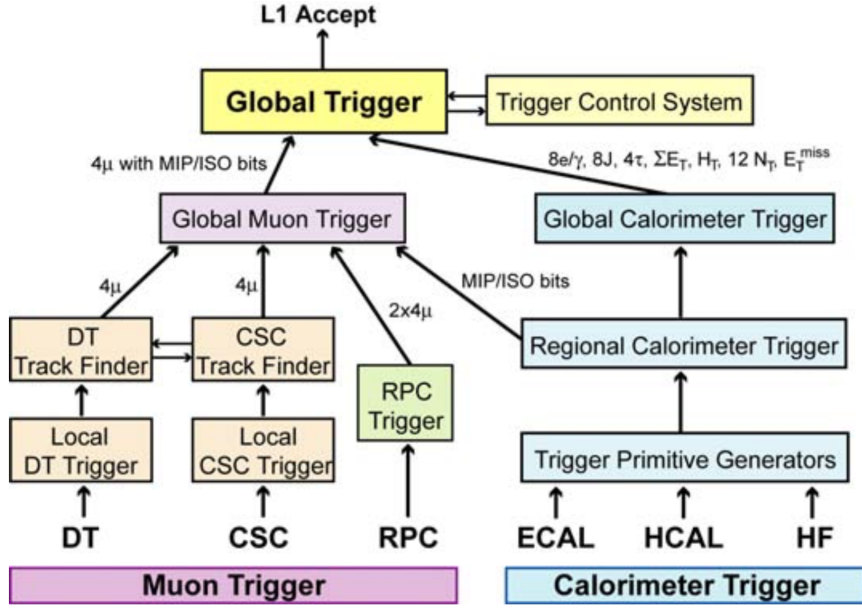


Figure 4-6: The Level-1 trigger architecture with components labeled and information flow indicated. Reprinted from Reference [1].

to produce the final set of muon candidates. The global trigger (GT) decides if an event should be sent to the HLT based on the information it receives from the GCT, the GMT, and the Timing, Trigger, and Control (TTC) system that monitors the readiness of the sub-detectors and the DAQ. The inner tracker is not included because the detector readout and reconstruction process take longer than the time allotted. Figure 4-6 shows a schematic description of the full L1 trigger process.

The HLT uses a version of the offline reconstruction software optimized to process a single event within 200 ms at the cost of some precision. The reconstruction is split into a series of filters that make decisions within regions of interest defined by the L1 trigger information. The HLT implements the desired trigger logic by constructing trigger paths out of these filters. For example, three filters relevant for dark matter searches are (1) a single photon, (2) large momentum imbalance, and (3) large hadronic energy. Combining the first two yields a trigger path targeting the monophoton channel while combining the latter two yields one for the monojet channel. To reduce CPU usage, simple decisions such as those using only the calorimeters or muon information are computed before complex decisions such as tracking.

An event must pass all the filters in a given path to be recorded in an output primary dataset (PD). Trigger paths are organized into PDs such that each PD contains events with similar topologies. Some examples are the SinglePhoton, DoubleMuon, and Jet/HT datasets. A single event that exhibits multiple different physics signatures can pass multiple trigger paths and end up in multiple PDs. These overlaps must be considered in the offline analysis.

4.6 Detector Simulation

The Geant4 program is used to simulate the detector response to the particles produced in collisions. Starting with the output of the particle-level MC described in Section 3.2, final state particles are propagated through the solenoid’s magnetic field into the passive and active elements of the detector where energy deposition, decay, and showering are simulated. Additional inelastic proton-proton collision are overlaid into an event to simulate the effects of pileup. As the particles interact with the detector, the response of the readout electronics is simulated, including the effects of noise. In order to minimize differences between simulated events and those from collisions, the reconstruction software and output format are the same for both up to the retention of additional truth information from the generators.

Chapter 5

Reconstruction

How do we turn electrical signals into physics.

5.1 Tracks

5.2 Primary Vertex

5.3 Particle Flow

5.4 Photons

We select high- E_T photons from the ECAL Barrel. First, we apply the following cuts to select high- E_T photon candidates:

- Super cluster $E_T > 175 \text{ GeV}$
- Super cluster $|\eta| < 1.4442$.

We use the uncorrected E_T of the supercluster as photon E_T . The use of supercluster raw E_T is motivated by an observation that this energy correction causes photon objects with large cluster shower width to exhibit unphysical energies. Figure 5-1 is a profile of the magnitude of the energy correction in bins of $\sigma_{inj\eta}$. As an illustration, an unphysically large correction is causing the transverse momentum of the photon

object in the event shown in Fig. 5-2 to be nearly twice as large as the E_T^{miss} , which is supposed to balance the visible, i.e., photon momentum. Photon objects with wide showers are used to estimate the hadron-to-photon misidentification background, while the photon energy resolution has an insignificant effect. Therefore, unbiased supercluster energy was chosen over the corrected photon energy.

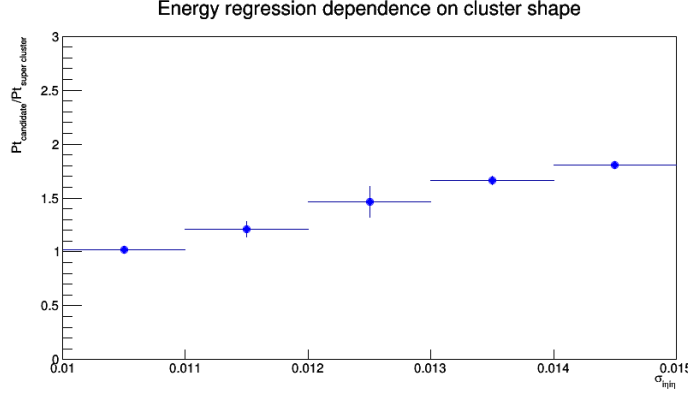


Figure 5-1: Magnitude of the energy correction on the photon object in bins of $\sigma_{i\eta i\eta}$.

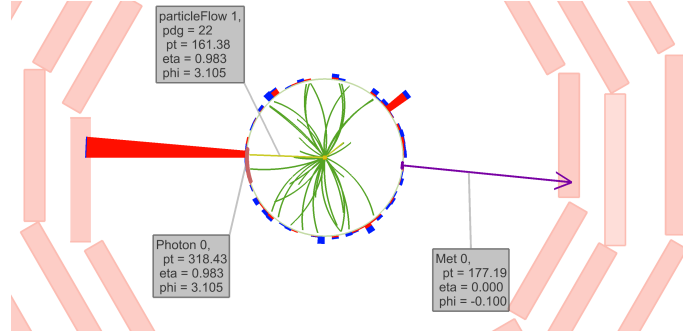


Figure 5-2: An example event where a photon with a wide shower receives a large energy correction.

To reduce hadron-to-photon misidentification rate, we apply the following collection of isolation and shower shape cuts, which will hereby be referred to as the e/γ ID:

- $H/E < 0.0260$
- $\sigma_{i\eta i\eta} < 0.01040$

- ρ -corrected maximum PF charged hadron isolation $I_{\text{CH}}^{\max} < 1.146 \text{ GeV}$
- ρ -corrected PF neutral hadron isolation $I_{\text{NH}} < 2.792 \text{ GeV} + 0.0112 \times E_{\text{T}}^{\gamma} + 0.000028 \times (E_{\text{T}}^{\gamma})^2 / \text{GeV}$
- ρ -corrected PF photon isolation $I_{\gamma} < 2.176 \text{ GeV} + 0.0043 \times E_{\text{T}}^{\gamma}$

In the identification criteria, the maximum PF charged hadron isolation I_{CH}^{\max} is the maximum of the standard PF charged hadron isolation computed for all reconstructed vertices. Standard PF charged hadron isolation is computed with respect to the primary vertex. Since the object with the highest p_{T} in the selected events is typically a photon, which has no intrinsic association to a vertex, it is possible that the identified primary vertex does not correspond to the pp interaction from which the photon object originate. In such cases, the photon object can be surrounded by charged hadrons, i.e., a part of a jet, and still appear isolated under the standard charged hadron isolation. The use of maximum isolation is a conservative measure to address such misidentification.

Effective areas for isolations are also recomputed to maintain flat pileup dependence as given in Table 5.1

Table 5.1: Effective areas for isolations.

Isolation	$ \eta < 1.0$	$1.0 < \eta < 1.479$
maximum PF charged hadron isolation	0.01064	0.1026
PF neutral hadron isolation	0.0597	0.0807
PF photon isolation	0.1210	0.1107

To reject electrons from the candidate sample, we require that no electron track seeds can be associated to the super cluster. This is known as the pixel seed veto.

To clean the candidate sample from photon objects originating from non-collision sources. we apply the following collection of cuts, which combined with the pixel seed veto constitutes the γ -specific ID:

- Beam halo tagger $E_{\text{MIP}} < 4.9 \text{ GeV}$
- $\sigma_{i\eta i\eta} > 0.001$

- $\sigma_{i\phi i\phi} > 0.001$
- Cluster seed time $|t_{\text{seed}}| < 3 \text{ ns}$.

Beam halo tagger is the total energy deposited in ECAL by a hypothetical beam halo muon that passes through the photon cluster. Lower bounds for $\sigma_{i\eta i\eta}$ and $\sigma_{i\phi i\phi}$ as well as the requirement on the cluster seed time are employed to reject spurious photon objects arising from “ECAL spikes”, or anomalous electronic signal induced at the ECAL Barrel photodetectors by nuclear or ionizing interactions in the photocathode.

5.5 Electrons

Electrons must have $p_T^e > 10 \text{ GeV}$ and $|\eta^e| < 2.5$ to be considered. Additionally, electrons must pass further cuts on the following observables:

- the $\sigma_{i\eta i\eta}$ of the corresponding SC,
- the $\Delta\eta$ and $\Delta\phi$ between the SC seed crystal and the GSF track at the PV,
- H/E of the corresponding ECAL and HCAL towers,
- the relative combined PF Isolation $(I_{\text{CH}} + I_{\text{NH}} + I_\gamma)/p_T^e$,
- the difference in energy measured in the tracker and the calorimeter $|1/E - 1/p|$,
- the number of missing hits in the inner tracker,
- and the existence of a pair of tracks originating at a displaced vertex, indicating photon conversion.

The exact values of the cuts are tuned based on whether the electron is in the barrel or the endcap and to give desired signal efficiencies and background acceptance. The loose ID is tuned to 90% signal efficiency and 0.5% background acceptance, while the tight ID is tuned to 70% signal efficiency and 0.1% background acceptance.

5.6 Muons

Muons must have $p_T^\mu > 10 \text{ GeV}$ and $|\eta^\mu| < 2.5$ to be considered. The veto muon ID is simply the requirement that a PF muon also be a Global muon, e.g., that the muon is linked between a muon signature from the inner tracker and the outer muon chambers. The loose muon ID adds the requirement that the relative combined PF Isolation $(I_{\text{CH}} + I_{\text{NH}} + I_\gamma)/p_T^\mu$ must be less than 0.25. In order for a muon to pass the tight ID, it must satisfy the following additional requirements:

- $p_T^\mu > 30 \text{ GeV}$
- Relative combined PF Isolation $(I_{\text{CH}} + I_{\text{NH}} + I_\gamma)/p_T^\mu < 0.15$.
- χ^2/ndof of the global-muon track fit < 10 ,
- At least one muon-chamber hit included in the global-muon track fit,
- Muon segments in at least two muon stations,
- The corresponding racker track has transverse impact parameter $d_0 < 2 \text{ mm}$ with respects to the primary vertex,
- The longitudinal distance of the tracker track with respects to the primary vertex is $d_z < 5 \text{ mm}$,
- At least one pixel hit,
- and more than five tracker layers with hits.

5.7 Hadrons and jets

5.8 Missing Transverse Energy

5.8.1 ECAL gain-switch effect

The “multi-fit” algorithm for ECAL hit reconstruction was found to have an unexpected behavior when there is a large energy deposit onto a single ECAL crystal,

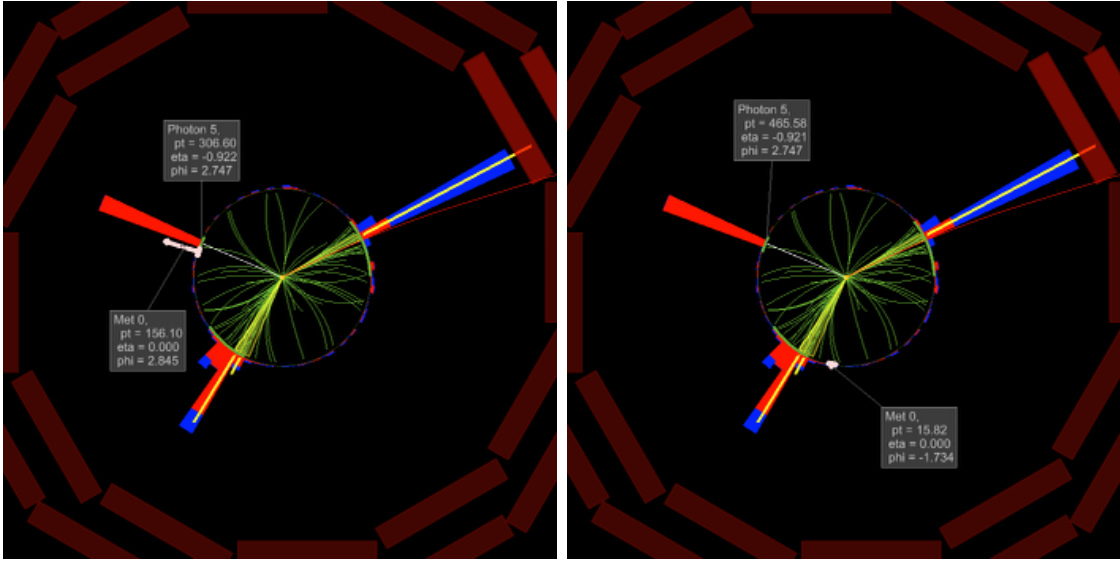


Figure 5-3: Two event displays comparing the same event, reconstructed without (left) and with (right) the fix for ECAL gain-switch effect.

such that the electronic signal converted at the frontend electronics is sourced partially from channels of the preamplifier with lower gains (6 or 1) than the default (12) channel. In the most dramatic cases, pulse misreconstruction would result in underestimation by hundreds of GeV of photon p_T . This effect is mitigated in the reprocessed data set used for this analysis by identifying ECAL clusters whose seed crystal hit had a switch of gains, and performing an alternative pulse reconstruction when possible.

The gain-switch problem affected the analyses documented in this thesis, since large underestimation of the energy of a photon in an otherwise typical $\gamma + \text{jets}$ event would introduce large missing transverse momentum to the event, typical collinear to the affected photon. Figures 5-3 and 5-4 are the visualization of how the new dataset changes the reconstructed photon energy and $E_{\text{T}}^{\text{miss}}$.

5.9 Beam Halo Phenomenology

Bremsstrahlung photons emitted by beam halo muons in the ECAL volume generate a physical EM shower in the ECAL crystals. Large deposits energy are rare, but the rate of beam halo penetration during the 2016 run was substantial. The characteristic

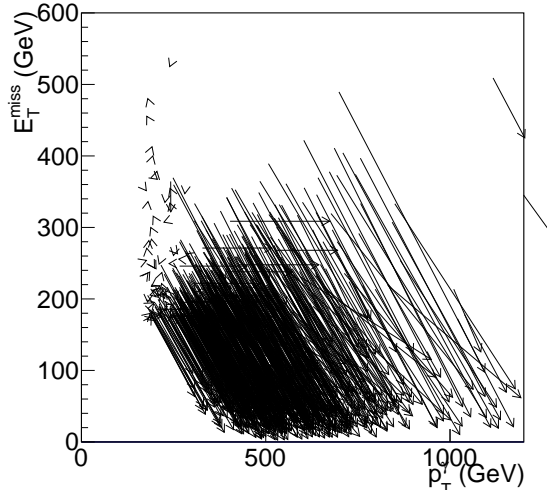


Figure 5-4: The change in reconstructed photon p_T and E_T^{miss} for events in the bin $\Delta\phi(\gamma, p_T^{\text{miss}}) < 0.05$ of the distribution in Figure ???. Each arrow represents a single event, the tail (head) of the arrow corresponding to $(E_T^\gamma, E_T^{\text{miss}})$ coordinates in the datasets without (with) the fix for the gain-switch problem.

features of a shower caused by a halo particle include coincident hits in the barrel muon system and a “trail” of low-energy clusters in ECAL along the particle trajectory. The beam halo MET filter described in Section 5.8 exploits the former, while the E_{MIP} variable described in Section 5.4 captures the latter.

Because beam halo particles are produced through complex LHC machine effects, it is natural that the observed distribution of the halo showers is not symmetric in the azimuthal angle in the detector coordinates. Figure 5-5 is a ϕ^γ distribution of the halo showers obtained from the Single Photon data set, requiring $E_T^{\text{miss}} > 140 \text{ GeV}$. Here, halo showers are defined as those that fail the MIP-tagging and in the event tagged by the CSC beam halo tagger. On the other hand reconstructed shower from all other sources are symmetric in ϕ^γ as demonstrated in Fig. 5-6.

For the distribution of Fig. 5-5 to be a valid template for halo showers, it must be first confirmed that its shape is invariant under photon selection requirements. However, further study of the ϕ^γ distribution of the halo showers indicates that the relative strength of the two prominent peaks in the distribution may change under the σ_{inj} selection requirement. To explain this phenomenon, one needs to look at

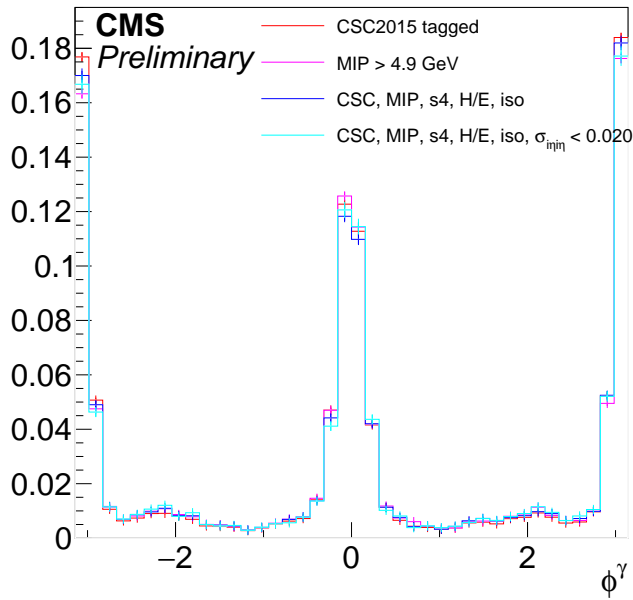


Figure 5-5: The ϕ^γ distribution of the halo-like showers, tagged in multiple ways. Histograms are normalized to unity. The cyan histogram is the ϕ^γ distribution after applying photon identification selections except for the shower shape. It can be seen that the ϕ^γ distribution is highly stable against the listed identification selections.

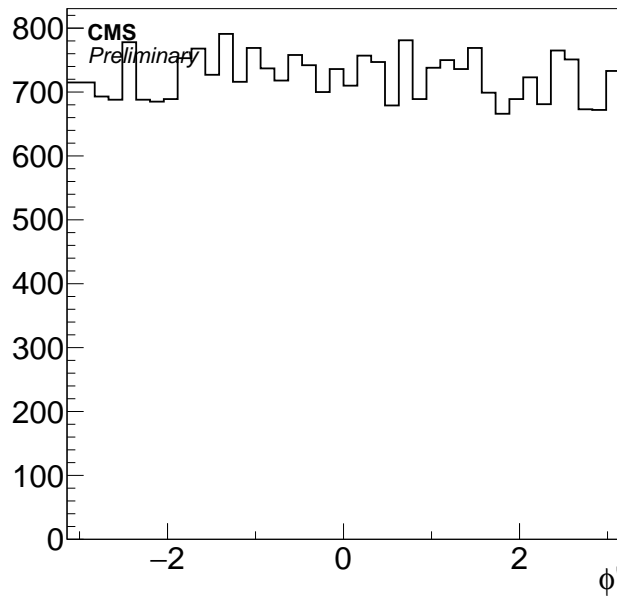


Figure 5-6: The ϕ^γ distribution from $Z(\rightarrow \nu\bar{\nu})+\gamma$ MC simulation.

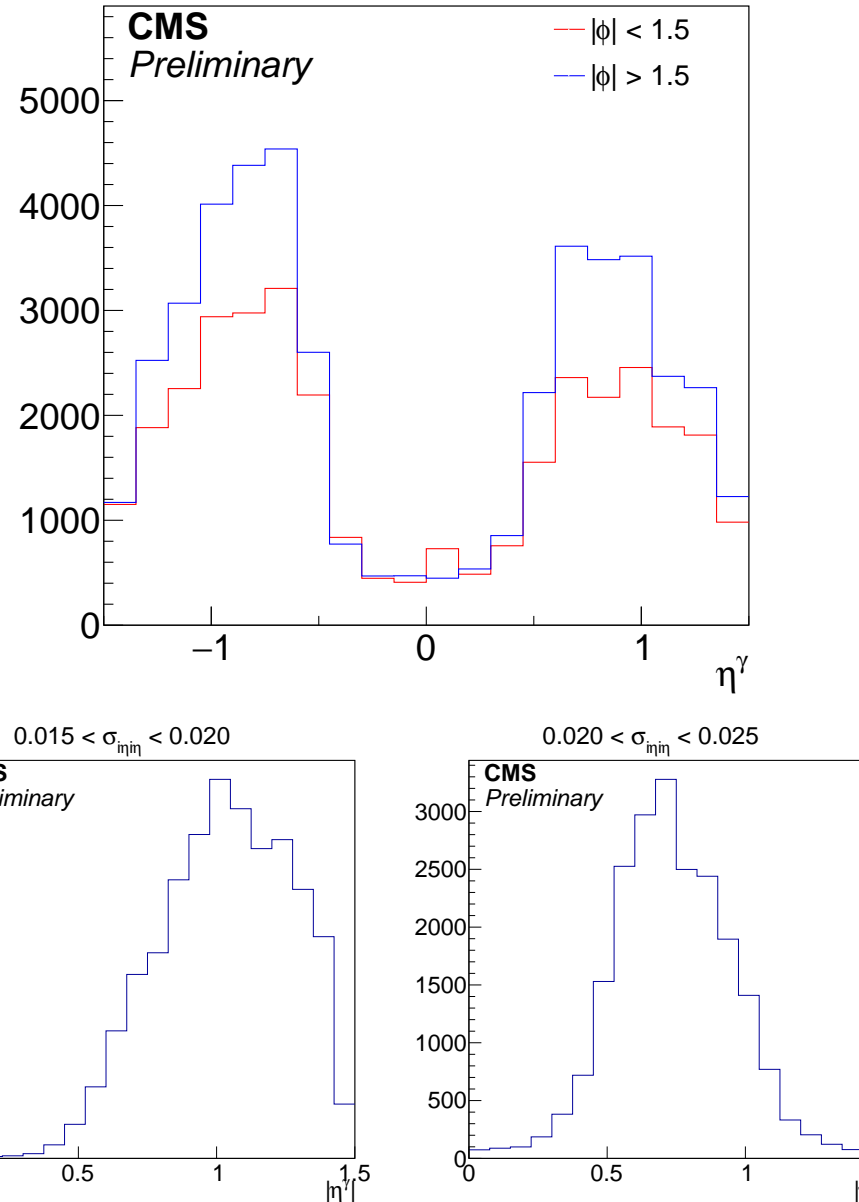


Figure 5-7: Top: η distribution of the halo-like showers with $|\phi| < \pi/2$ and $|\phi| > \pi/2$. Bottom: shift in the η distribution of the halo-like showers with respect to the requirement on $\sigma_{inj\eta}$.

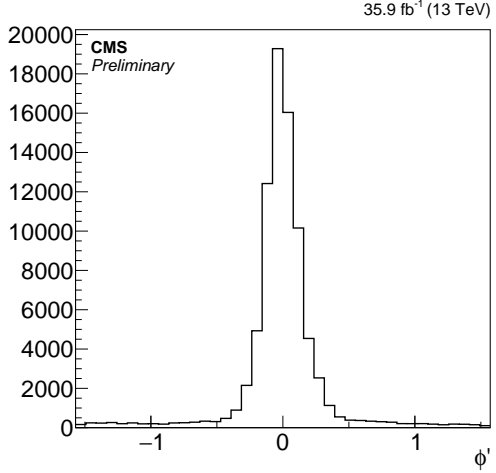


Figure 5-8: Folded ϕ' distribution of the halo sample.

the the η^γ distribution of the shower populations near $\phi^\gamma \sim 0$ and $\phi^\gamma \sim \pi$, shown in the top portion of Figure 5-7. Meanwhile, halo showers tend to have narrower shape in the η direction when occurring at high η , due to the projective geometry of the ECAL crystals, visible in the bottom portion of Figure 5-7 bottom). Combining the two observations, the conclusion is that the stringent requirement on the narrowness of the shower in the photon selection will preferentially reduce the $\phi \sim 0$ population.

Nevertheless, the invariance under photon selection is recovered by folding the ϕ^γ distribution such that the two peaks of the halo showers coincide. To match the positions of the peaks in the halo template, the distribution is shifted by 0.005 and then folded along 0. The new angular variable ϕ'

$$\phi' := \left| \left[[\phi^\gamma + 0.005]_{-\pi}^{\pi} - \frac{\pi}{2} \right]_{-\pi}^{\pi} \right| - \frac{\pi}{2}, \quad (5.1)$$

where $[\cdot]_\pi^\pi$ signifies casting the content into range $[-\pi, \pi]$, exhibits a unimodal distribution for the halo template, as shown in Fig. 5-8.

The contribution of real photons into the halo control sample is negligible. This is confirmed from the $\sigma_{i\eta i\eta}$ distribution of the halo control sample and the correlation between $\sigma_{i\eta i\eta}$ and E_{MIP} in a MC true-photon sample. The $\sigma_{i\eta i\eta}$ distribution of the halo control sample features a small peak at $\sigma_{i\eta i\eta} \sim 0.01$, which can be attributed

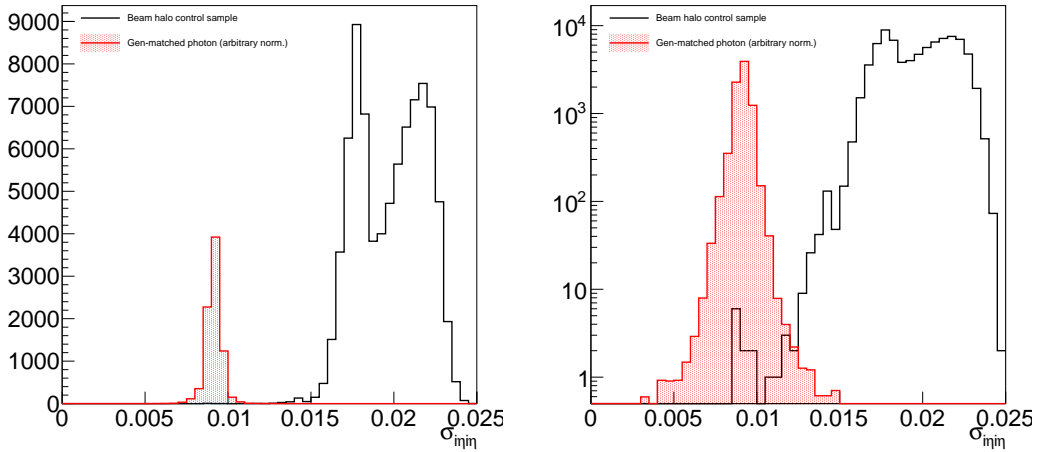


Figure 5-9: The $\sigma_{i\eta i\eta}$ distribution of the beam halo control sample and a reference distribution from truth-matched MC photons. Left: linear scale, Right: log scale. There is a small peak at $\sigma_{i\eta i\eta} \sim 0.01$ in the beam halo control sample, which is not visible in linear-scale.

to contributions from true photons, as the photon $\sigma_{i\eta i\eta}$ distribution overlaid in Figure 5-9 suggests. However, the contribution of true photons diminishes rapidly with increasing $\sigma_{i\eta i\eta}$. Additionally, Figure 5-10 illustrates that the shape of the true-photon $\sigma_{i\eta i\eta}$ does not change significantly with respect to E_{MIP} . From these two observations, we can see that there are only a negligible number of true photons in the halo control sample.

While the peaking behavior is a robust feature of the halo showers, their rate is not easily predictable. Therefore, the contribution from beam halo processes is estimated by a direct fit to the observed data during the signal extraction process, described in Section 7.5

5.10 ECAL Barrel Spikes Phenomenology

Noise in the photodetector or the detector electronics can result in spurious photon signals. Most of the time, such spurious signal is filtered out by multiple layers of protection, starting from the so-called “spike killer” algorithm at the level-1 trigger [?]. Nevertheless, in rare cases, noise in a single ECAL channel coincides with pileup

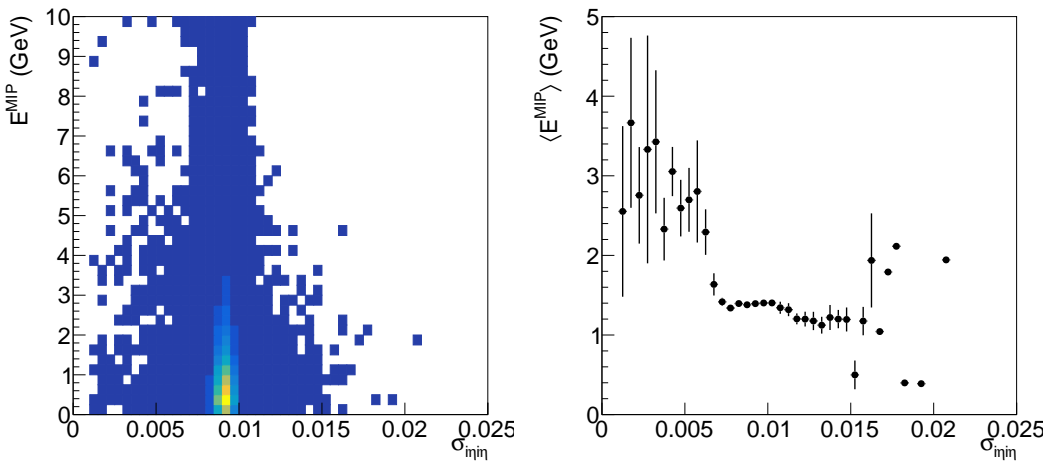


Figure 5-10: Correlation between $\sigma_{i\eta i\eta}$ and E_{MIP} in truth-matched MC photons. Left: $E_{\text{MIP}}-\sigma_{i\eta i\eta}$ distribution. Right: average E_{MIP} in bins of $\sigma_{i\eta i\eta}$.

or other energy deposit in the nearby crystals and appear as a high-energy photon cluster.

The origin of ECAL spikes is believed to be interactions of neutrons and other hadronic particles (collectively called neutral hadrons hereafter) with the photocathode material of the ECAL avalanche photo diodes (APD). Nuclear fission at the APD surface then causes a large electron avalanche, which is mistaken as a large photon yield scintillation in the ECAL crystal. Evidences supporting this hypothesis is documented in Ref. [?]. In Figure 5-11, scaling of the rate of spikes with the instantaneous luminosity is confirmed, up to much higher luminosity values than was observed at the time when Ref. [?] was written.

A known feature of such spurious photon clusters is that the recorded pulse shape of the seed crystal, i.e., the channel with the noise, is not what is expected from a real electromagnetic shower in ECAL. In particular, this translates to a distinctive early rec hit time distribution, since the rec hit time is extracted from a fit to the pulse shape assuming a normal pulse.

In the normal CMS data reconstruction, rec hits that are tagged as spike-like are ignored in clustering. Rec hits are tagged as spikes if there is very little energy deposit recorded in the surrounding crystals, or if the reconstructed time is out of an allowed

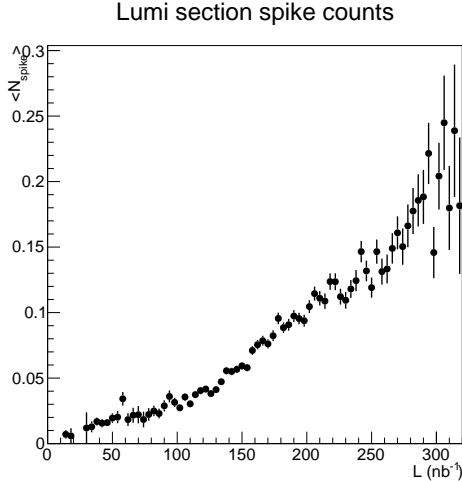


Figure 5-11: Average number of spike clusters in a luminosity section, identified by $\sigma_{i\eta i\eta} < 0.001$ and $E > 50$ GeV, in muon-triggered events, versus integrated luminosity of the luminosity section.

window. Identical algorithms are employed in the HLT and offline reconstructions.

To study an unbiased spike sample, ECAL DIGI samples stored in the SingleMuon AOD datasets are reconstructed into ECAL clusters with no spike cleaning applied. DIGIs associated with the standard and “uncleaned” photon objects are stored in AOD, and ones for the uncleaned photons is rich in spike-like hits. Figure 5-12 shows how narrow clusters are cleaned away in the normal reconstruction.

Figure 5-13 shows the spacial and temporal distributions of the rec hits seeding narrow ($\sigma_{i\eta i\eta} < 0.001$) clusters. The spacial distribution appears mostly random, indicating that there is no single source of spike-like rec hits. The two highest peaks in the time distribution at $t \sim -15$ ns and $t \sim 10$ ns are characteristic of pulse shapes, which rise faster than the pulse from the normal scintillation. The second peak is understood to come from the next bunch crossing.

The small peak at $t \sim 0$ in the time distribution of Fig. 5-13 is due to actual “physical” clusters that happened to have a very narrow cluster shape. By processing the γ +jets MC simulation events through this special reconstruction, we see that about 0.5% of ECAL clusters from prompt photons have $\sigma_{i\eta i\eta} < 0.001$ as shown in Figure 5-14.

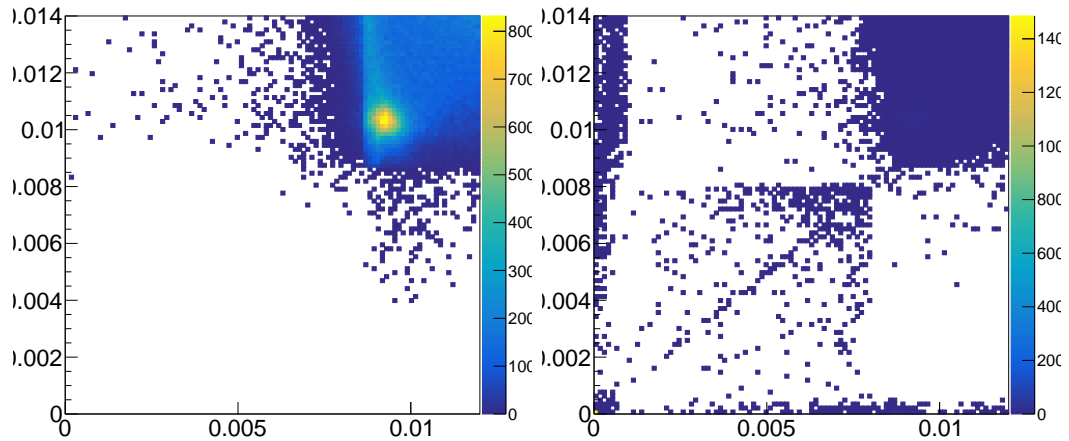


Figure 5-12: Two-dimensional distributions in $\sigma_{i\phi i\phi}$ and $\sigma_{i\eta i\eta}$ of ECAL clusters in the standard reconstruction (left) and the special reconstruction with no spike cleaning (right).

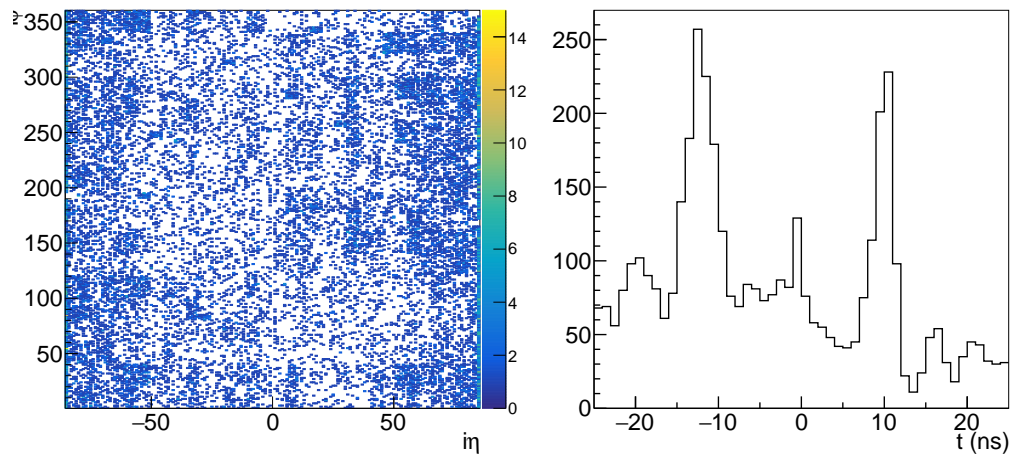


Figure 5-13: $\eta-\phi$ and time distributions of seed hits of narrow ($\sigma_{i\eta i\eta} < 0.001$) clusters.

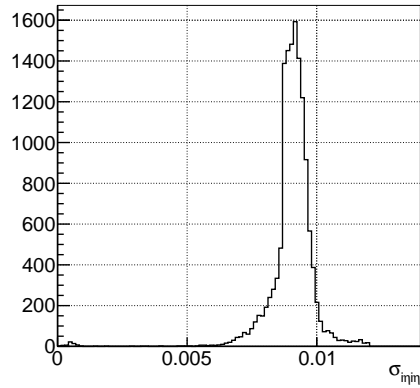


Figure 5-14: $\sigma_{inj\eta}$ distribution of uncanceled clusters from $\gamma + \text{jets}$ MC simulation.

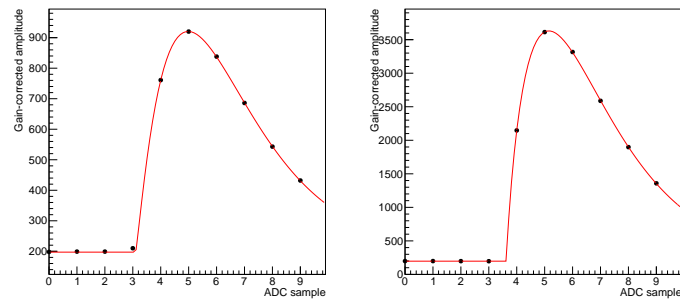


Figure 5-15: Example ECAL DIGIs and corresponding pulse shapes reconstructed through χ^2 fits of Equation 5.2, for normal (left) and spike-like (right) hits.

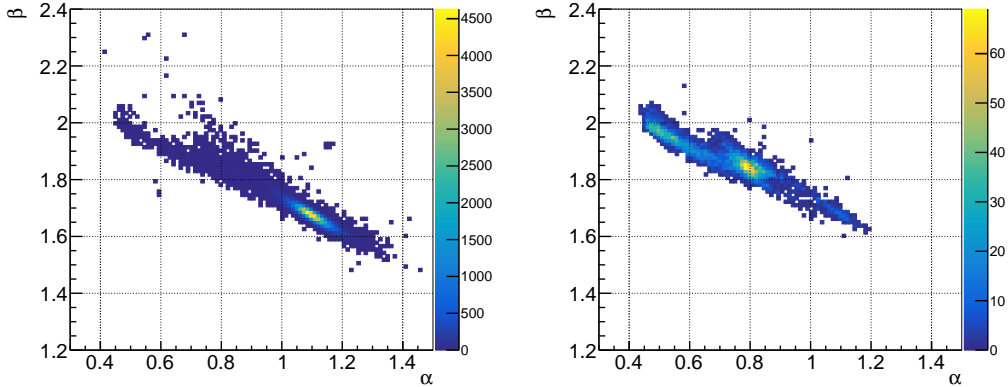


Figure 5-16: α - β distributions of the seed hits of physical wide clusters (left) and spike-like clusters (right).

To understand the time distribution, one can investigate the original DIGI samples from which rec hits are made. At each event readout, a single ECAL channel outputs 10 ADC signals corresponding to a sampling of the analog pulse output of multi-gain preamplifier (MGPA) in range $t_0 - 125 \text{ ns} < t < t_0 + 100 \text{ ns}$, where t_0 is the time of the triggering bunch crossing. These 10 signal points can be described well by the formula

$$f(t) = A \left(1 - \frac{t - \tau}{\alpha\beta}\right)^\alpha \exp\left(-\frac{t - \tau}{\beta}\right). \quad (5.2)$$

In the formula, parameters A and τ correspond to the pulse amplitude and peak time, whereas α and β control the shape of the pulse. Figure 5-15 illustrates various observed pulse shapes fit with the above formula with all parameters floating. A χ^2 fit is employed using the average noise amplitude of each MGPA channel as the errors on the data points. The noise is measured in ECAL calibration cycles in the inter-fill period and is recorded in the conditions database.

In the α - β parameter space, seed rec hits of wide clusters concentrate around $(\alpha, \beta) \sim (1.1, 1.7)$, while spike-like hits populate the region $\alpha < 0.9$ as shown in Figure 5-16. In fact, the pulse amplitude distribution of narrow-cluster seeds with $\alpha > 0.9$ is unlike that of the narrow-cluster seeds with $\alpha < 0.9$, and resembles the amplitude distribution of wide-cluster seeds shown in Figure 5-17. This suggests that

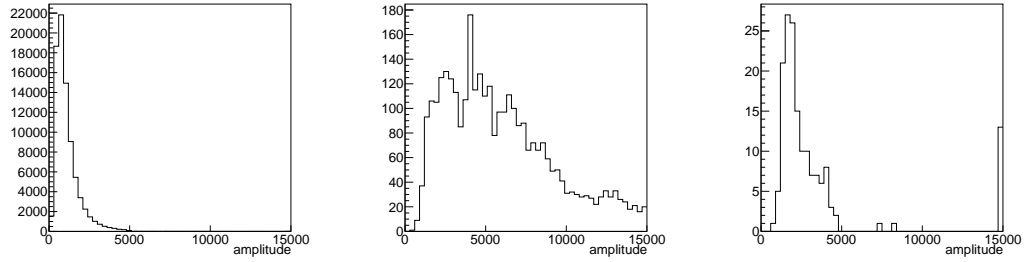


Figure 5-17: Seed crystal pulse amplitude distributions of physical wide clusters (left), narrow clusters with $\alpha < 0.9$ (center), and narrow clusters with $\alpha > 0.9$ (right).

the population $\alpha > 0.9$ correspond to the clusters of physical, prompt photons. It then follows that spike hits can be regarded to exclusively have sharp pulse shapes.

Chapter 6

Calibration

The differences between data and MC efficiencies for various object selections have to be corrected to achieve accurate signal and background predictions. The efficiencies of individual object selections are measured in data and applied to the MC.

6.1 Trigger Efficiency

The candidate events were recorded with the HLT_Photon165_HE10 trigger. The high-level trigger algorithm is relatively simple, with only a requirement of at least one e/γ object, reconstructed only around a L1 jet or egamma object, with $E_T > 165 \text{ GeV}$ and $H/E < 0.1$, where transverse energy E_T is defined as the reconstructed energy deposit in the calorimeter cluster multiplied by the sine of the polar angle of the position of the cluster measured from the center of the detector. The variable H/E is the ratio of the energy deposit in the HCAL to that in the ECAL for a single calorimetric shower. Only the HCAL deposit in the tower behind the center of the ECAL energy deposit is considered.

Because the trigger decisions both in the L1T and HLT are based on the existence of a single object in the event, their efficiency can be measured by looking for trigger objects that match the candidate photon object in an appropriate data set. Trigger objects are the four-momenta of the objects reconstructed at the trigger level that are relevant for making trigger decisions. The match is defined by $\Delta R = \sqrt{\Delta\eta^2 + \Delta\phi^2}$

between the two objects being less than a threshold. For the offline photon object, a line that connects the detector origin and the cluster position was used to define its direction.

The trigger efficiency measurement is performed on the SingleMuon data set, exploiting events mostly from leptonic $t\bar{t}$ ($e\mu$) topology. Events with a candidate-quality photon without electron veto requirement (see Section 5.4) and a muon object that passes the “tight” identification requirement defined in Section 5.6 and matches the trigger object of the HLT_IsoMu24 or HLT_IsoTkMu24 triggers are used. The matching rate of the photon object and the trigger object is the trigger efficiency. Figure 6-1 shows the L1+HLT combined efficiency as a function of the photon E_T . It can be seen that the trigger is fully efficient for $E_T > 175$ GeV.

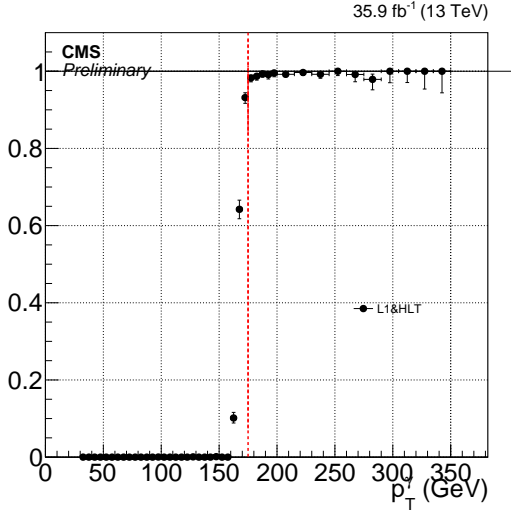


Figure 6-1: Efficiency turn-on of HLT_Photon165_HE10 for photons passing the candidate selection, measured using $\mu+e/\gamma$ events from the SingleMuon data set. Red vertical line corresponds to $E_T = 175$ GeV.

For the first period of data taking, the HLT_Photon165_HE10 trigger was seeded only by an isolated egamma L1 trigger. This L1 seed becomes inefficient at high E_T due to a misconfiguration in the H/E computation algorithm. The effect is visible when plotting the efficiency for a wide E_T range (Figure 6-2 left). To mitigate the effect, in the later periods, the trigger was seeded by the logical OR of SingleEG40 and SingleJet level-1 triggers. SingleJet triggers with multiple p_T threshold are combined.

Even with this addition, the measured trigger efficiency is not 100% at the plateau, but is flat with respect to E_T (Figure 6-2 right). In principle, the efficiency should be applied to all simulation-based background estimate whose normalization is fixed by theoretical calculation of the cross section. However, as discussed in Chapter 7, the dominant background in the analysis are given floating normalization that is fit to observed data, and the only simulation-based background processes with absolute normalization are those that contribute at $\mathcal{O}(1)\%$, with large systematic uncertainties. Therefore we deem the slight discrepancy of the trigger efficiency from unity as irrelevant.

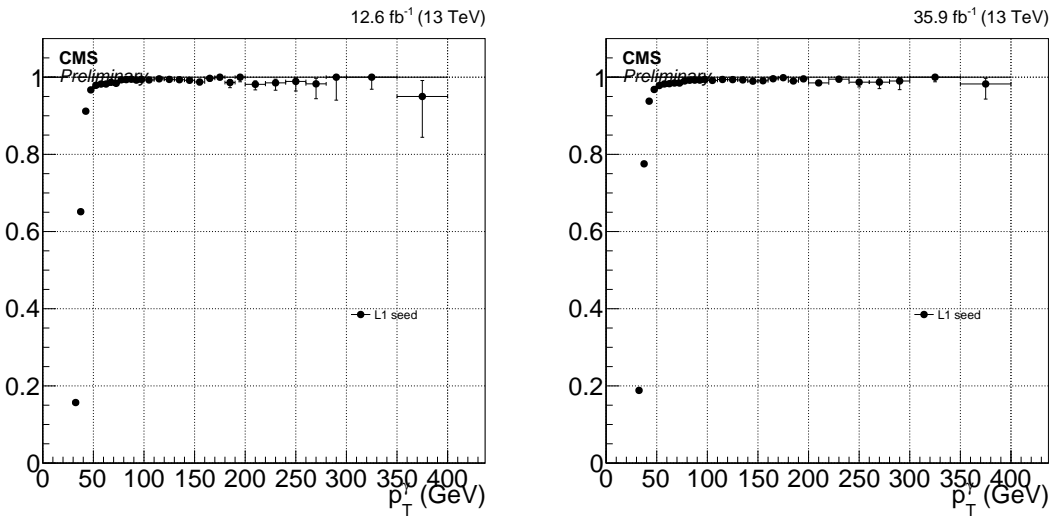


Figure 6-2: Efficiency of L1 seed for the signal trigger in periods B and C (left) and the full data set (right).

6.2 Photon Identification Efficiency

When measuring the photon efficiency scale factor, we split the photon ID described in Section 5.4 into two parts, which we call the e/γ portion and the γ -specific portion. The e/γ portion of the ID consists of the H/E, σ_{inj} , and PF isolation cuts and is measured using the “tag-and-probe” (TP) method as these variables have similar efficiencies for physical electrons and photons. The γ -specific portion of the ID consists of the pixel seed veto and non-collision rejection cuts. We measure the efficiency of

γ -specific portion on a sample of physical photons using a $\sigma_{i\eta i\eta}$ template fit method.

We perform both efficiency estimates as a function of p_T with the binning [175,200], [200,250], [250,300], [300,350], [350,400] and [400, ∞). This binning was chosen based on the number of available events in data for the failing probes fit in the TP method and the background template for the $\sigma_{i\eta i\eta}$ fits.

6.2.1 e/γ ID Efficiency

The efficiency corresponding to the e/γ part of the photon ID is estimated by exploiting the Z boson decay into an e^+e^- pair. In this “tag-and-probe” (TP) method, a high-quality electron object (tag) is identified in a single photon data sample, and the accompanying electron is sought for in the pool of electromagnetic objects (probes) in the event. The area of the peak in the mass distribution of the tag-probe system around the Z boson mass (between 81 GeV and 101 GeV) is then measured once applying the $e\gamma$ ID requirements on the probe and once inverting the requirements. Denoting the two areas N_{pass} and N_{fail} , respectively, the resulting efficiency $\epsilon_{e/\gamma}$ is given by

$$\epsilon_{e/\gamma} = \frac{N_{\text{pass}}}{N_{\text{pass}} + N_{\text{fail}}}. \quad (6.1)$$

The TP measurement is performed on a subset of the single photon triggered events where there is an electron object (tag) passing the “tight” identification criteria in addition to the triggering photon (probe). All possible tag-probe combinations are considered; if the tag object can also serve as a probe and the probe object as a tag, which is a common occurrence in the case when the probe is electron-like (passes the $e\gamma$ ID), then the two combinations are considered independently to avoid the bias caused by somehow preferring one object over another to use as the probe.

The tag-probe mass distributions are then fit to extract N_{pass} and N_{fail} . The fit model is composed of two templates, where one template describes a pure $Z \rightarrow ee$ line shape and the other describes the background contributions. The backgrounds to the fits include $W+\text{jets}$, diboson, and $t\bar{t}$ productions, which are all negligible and estimated to contribute by less than 1%. Minor contribution from processes that do

not involve true electrons, such as diphoton production with a strongly asymmetric conversion on one of the photons and misidentification of a QCD jet as an electron, are predicted to be negligible from MC studies.

The $Z \rightarrow ee$ template is given by an analytic shape of Breit-Wigner distribution convoluted with the Crystal Ball function. The mass and width parameters of Breit-Wigner distribution are fixed to PDG values. Crystal Ball parameters are allowed to float in the fit. It is well known that Breit-Wigner distribution usually does not describe the mass distribution well when the tag or the probe is under kinematically exclusive selections. However, at this high probe p_T scale, selected events are mostly of $Z + \text{jets}$ topology with a boosted Z boson, which makes the selection rather inclusive in terms of the tag-probe invariant mass.

The background template is taken from events collected by the single photon trigger where an additional muon object is present, making use of the fact that the most of the background processes in both fits are symmetric in lepton flavor. In order to mitigate the statistical fluctuation in the background sample, the actual template is constructed by a Gaussian kernel estimation of the mass distribution of this muon-probe sample.

The floating parameters of the fits are therefore the normalizations of the $Z \rightarrow ee$ and background templates and the Crystal Ball smearing parameters. Selected example fits are shown in Figure 6-3.

The statistical uncertainty of the fits is estimated by generating toy data from the nominal fit result with the same number of entries as the fit target distribution. The mass distribution of the toy data is then fit with the same model with the parameters floating. This procedure is repeated 100 times to obtain a distribution of the $Z \rightarrow ee$ event yields, and its standard deviation is taken as the statistical uncertainty of the fit. Relative statistical uncertainty on the efficiency is 10%.

To estimate the effect of potential mismodeling in the fits, alternative fits varying the background and signal templates are performed first. In the alternative-background fit, a simple linear function is tested. In the alternative-signal fit, no Crystal Ball convolution is performed to the signal template and the mass and width

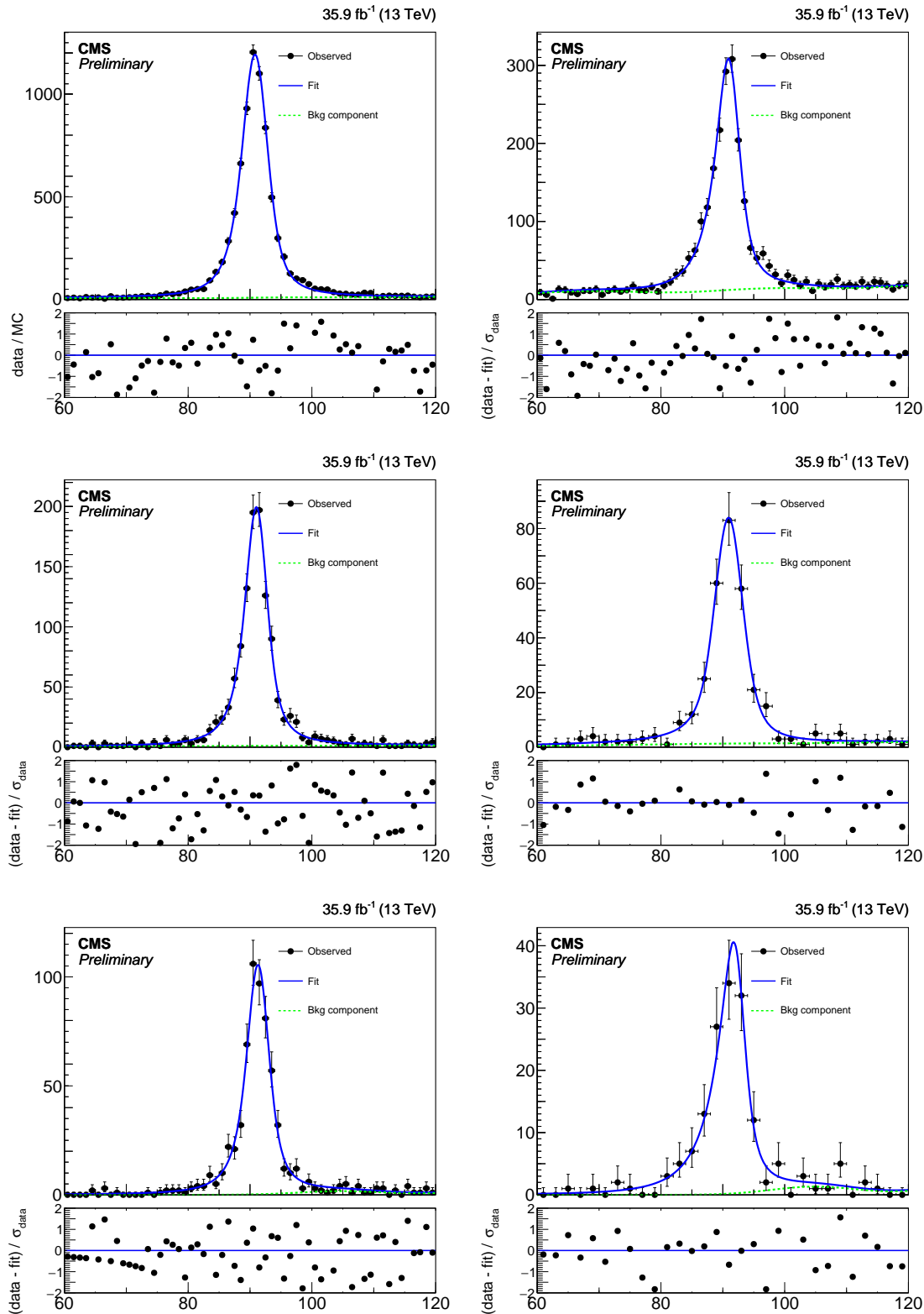


Figure 6-3: Fits to the mass distributions for pass (left) and fail (right) selections, in bins of probe p_T : $175 < p_T < 200 \text{ GeV}$ (top), $300 < p_T < 350 \text{ GeV}$ (middle), $p_T > 400 \text{ GeV}$ (bottom). The blue solid line represents the full fit model, and the green dashed line its background component.

of the Breit-Wigner function are allowed to vary. Resulting best-fit distributions of these alternative models are then used to generate a large number of toy distributions, which are fit by the nominal model. The average shift of the fit result from the nominal value is then taken as the uncertainty. The relative uncertainty on the efficiency varies from 2 to 4% depending on the probe p_T bin.

The MC efficiency is taken from counting the number truth-matched electrons passing and failing the e/γ part of the ID from a $Z \rightarrow ee$ sample. Additionally, the MC efficiency is computed using the same procedure as in data as a cross-check. The two methods are consistent within their uncertainties.

The data efficiencies, MC efficiencies, and resulting scale factors as a function of p_T are shown in Figure 6-4. The scalefactors are consistent with unity within the uncertainties. The numerical values are given in Table 6.1. We use the bin by bin scale factor corresponding to the truth values in the analysis.

Table 6.1: e/γ scale factors as a function of photon p_T .

p_T^{probe} (GeV)	MC Fit	Truth
(175, 200)	1.014 ± 0.008	1.009 ± 0.016
(200, 250)	1.003 ± 0.008	0.999 ± 0.014
(250, 300)	1.014 ± 0.010	1.016 ± 0.019
(300, 350)	1.002 ± 0.014	0.997 ± 0.022
(350, 400)	0.986 ± 0.012	0.987 ± 0.022
(400, 6500)	0.988 ± 0.011	0.999 ± 0.016

6.2.2 γ -specific ID Efficiency

To measure the efficiency of the γ -specific component of the photon ID, we use a $\sigma_{i\eta i\eta}$ template fit to extract the number of true photons from a pool of photon objects passing the e/γ ID.

The measurement is performed over a EM object+jet control sample where we require one jet passing with $p_T > 100$ GeV and $|\eta| < 2.5$ which passes the loose jet ID. The EM object passes the e/γ ID with the exception of the following relaxed cuts:

- $\sigma_{i\eta i\eta} < 0.015$

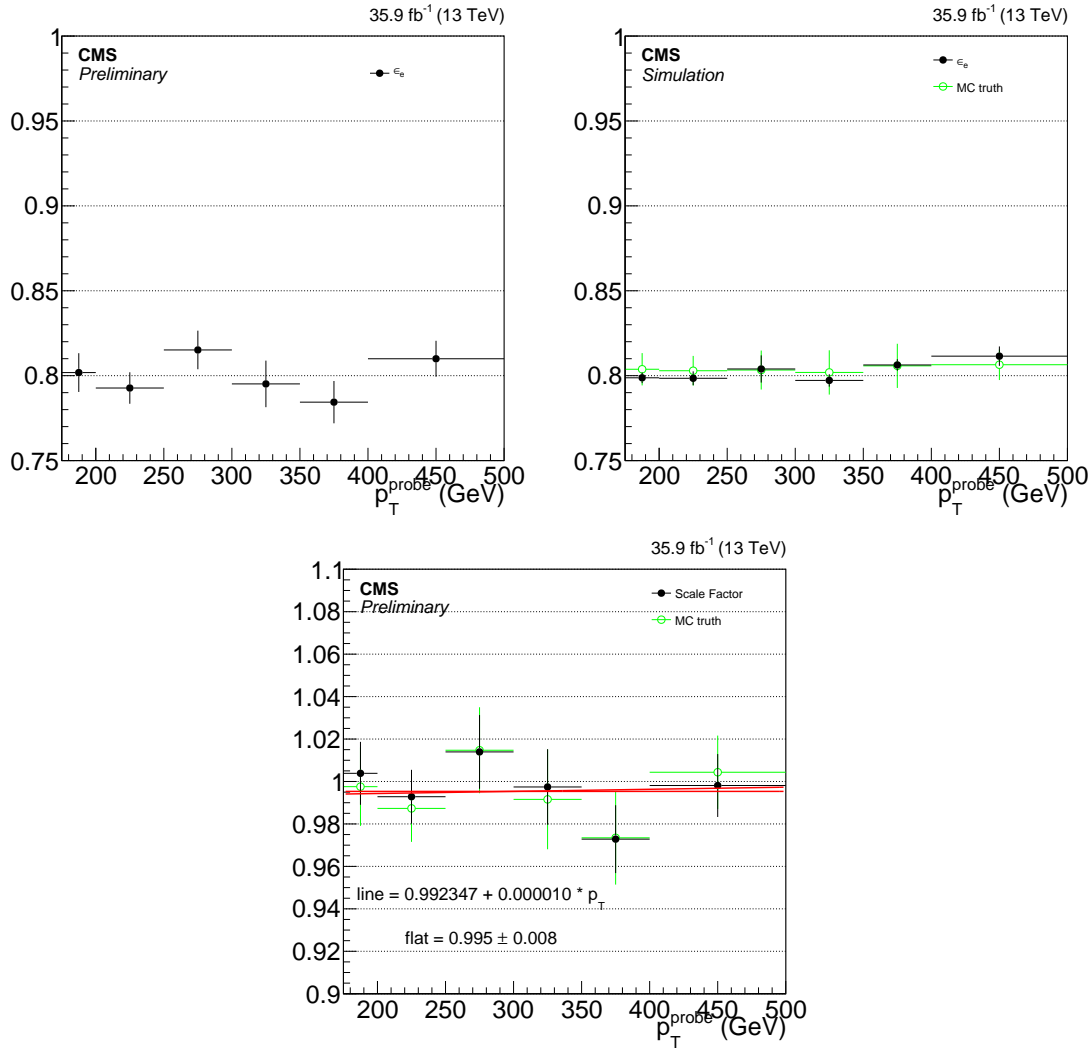


Figure 6-4: e/γ component of the photon identification efficiency for data (top-left) and MC (top-right) and corresponding scale factor (bottom) as a function of photon p_T .

- $I_{\text{CH}} < 11.0 \text{ GeV}$.

Additionally, we apply a $E_{\text{T}}^{\text{miss}} < 60 \text{ GeV}$ cut to make this region orthogonal to the signal region of the analysis.

We then fit the $\sigma_{i\eta i\eta}$ distribution of the EM object with a template describing the $\sigma_{i\eta i\eta}$ shape of true photons and another describing the hadronic background. The real photon template is taken from $\gamma + \text{jets}$ MC requiring the photon to pass the e/γ ID except for the $\sigma_{i\eta i\eta}$ requirement. The fake photon template is taken from the same data control sample, requiring $5 \text{ GeV} < I_{\text{CH}} < 7 \text{ GeV}$. The integral of the post-fit real photon template below $\sigma_{i\eta i\eta} = 0.0104$ is the number of true photons in the target sample.

The fit is performed once for all EM objects and then once for EM objects passing the γ -specific ID criteria. The ratio of the numbers of true photons obtained in the two fits is the efficiency.

The $\sigma_{i\eta i\eta}$ template fit method in its simplest form fits the observed distribution with the following fit function:

$$P(f; \sigma_{i\eta i\eta}) = f \cdot h_s(\sigma_{i\eta i\eta}) + (1 - f) \times h_b(\sigma_{i\eta i\eta}), \quad (6.2)$$

where h_s is the signal template, h_b is the background template, and f is the fraction of true photons in the target sample. Both the target template and the fit function are normalized to unity, removing the number of photon candidates in the target sample N as a fit parameter and leaving f as the only free parameter.

However, the hadronic background template, taken from the data control sample, has contributions from real photons. The amount of this “photon contamination” depends on the sideband choice, but is finite even for a sideband with very large I_{CH} . As described below, we perform additional fits with the background templates from alternative sidebands $3.5 \text{ GeV} < I_{\text{CH}} < 5 \text{ GeV}$ (“near”) and $7.5 \text{ GeV} < I_{\text{CH}} < 9 \text{ GeV}$ (“far”) to assess the systematic uncertainty. The photon contamination of the nominal and far sideband is 10-15%, and in the near sideband, it can go up to approximately 20% (see Figure 6-5).

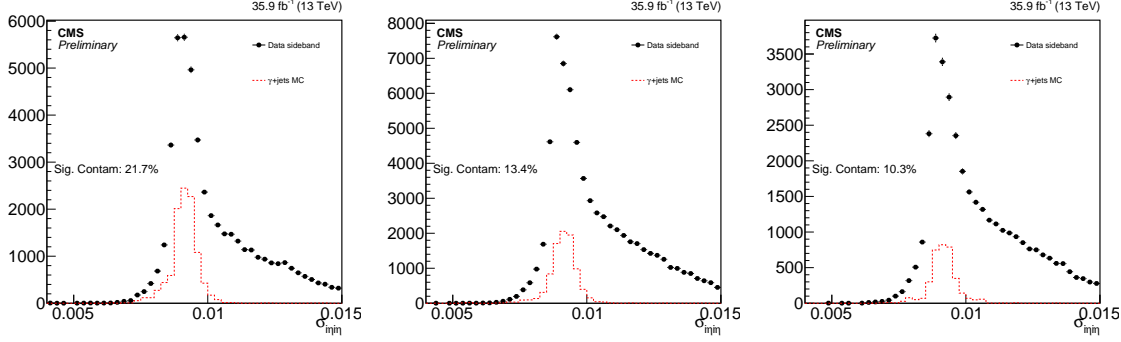


Figure 6-5: Signal contamination in the [3.5,5.0] (left), [5.0,7.5] (middle), and [7.5,9.0] (right) isolation sidebands.

To remove the photon contamination from the background templates, we modify the method and create a new background template h_b^{sub} from the original background template h_b by subtracting the true photon shape in the sideband $h_{S'}$. After normalization to unity, we obtain the expression

$$h_b^{\text{sub}}(\sigma_{i\eta i\eta}) = \frac{h_b(\sigma_{i\eta i\eta}) - S'/B \cdot h_{S'}(\sigma_{i\eta i\eta})}{1 - S'/B}, \quad (6.3)$$

where B is the number of photon candidates in the sideband and S' is the number of true photons in the sideband.

To determine S' , we start with the number of true photons in the target sample, $f \cdot N$. We then scale this by the ratio of the relative fractions of true MC photons in the I_{CH} sideband r_{sb} and in the signal region r_{sig} , giving us the expression

$$S' = f \cdot \frac{r_{\text{sb}}}{r_{\text{sig}}} \cdot N. \quad (6.4)$$

Going back to our original fit function and replacing h_b with h_b^{sub} gives us

$$P(f; \sigma_{i\eta i\eta}) = f \cdot h_s(\sigma_{i\eta i\eta}) + (1 - f) \times \frac{h_b(\sigma_{i\eta i\eta}) - S'(f)/B \cdot h_{S'}(\sigma_{i\eta i\eta})}{1 - S'(f)/B}, \quad (6.5)$$

which converges to the original fit function if $S' = 0$, i.e., if there is no photon contamination in the sideband. Note that f is still the only free parameter for this new function as S' only depends on f and $r_{\text{sb}}/r_{\text{sig}}$ is set constant in the fit (see

discussion of systematics for more detail).

There are four main sources of systematic uncertainty for this measurement. The first comes from the sideband choice, as the relative rates of different types of fake photons varies with I_{CH} . The second comes from the true photon I_{CH} shape, as this is used to determine the normalization of true photons in the sideband. Currently, this shape is taken from MC and thus there is the potential to mismodel the effects of the underlying event and pile-up. The third comes from the true photon $\sigma_{i\eta i\eta}$ distribution. As we take this from MC as well, we can mismodel the signal template shape. Finally, at high p_T , we suffer from low yields in our I_{CH} sidebands, which can lead to fluctuations that unduly influence the fit.

The uncertainty due to sideband choice is simply the larger of the differences of the purities measured using the near and far sidebands versus the nominal sideband. Figure 6-6 shows fits using the three sidebands for the $[400, \infty)$ p_T bin.

To measure the uncertainty due to the I_{CH} shape, we look at the I_{CH} for electrons in $Z \rightarrow ee$ events in both data and MC. Using these distributions, we obtain a data/MC scale factor which we apply to the MC true photon I_{CH} distribution to obtain a scaled MC distribution. This process is shown in Figure 6-7. Then, we recount the photons using this new distribution and take the difference in the values obtained using the raw MC and scaled MC distributions as a systematic uncertainty.

To measure the uncertainty due to the signal template $\sigma_{i\eta i\eta}$ shape, we look at the $\sigma_{i\eta i\eta}$ distributions for electrons in both data and MC. Again we compare $Z \rightarrow ee$ events in data and MC. From the $\sigma_{i\eta i\eta}$ distributions of high-purity electron samples, obtain a data/MC scale factor which we apply to the MC true photon $\sigma_{i\eta i\eta}$ distribution to obtain a scaled MC distribution. Then, we recount the photons using this new distribution and take the difference in the values obtained using the raw MC and scaled MC distributions as a systematic uncertainty. The difference between fits with and without the $\sigma_{i\eta i\eta}$ scaling are shown in Figure 6-8.

To estimate the uncertainty due to statistical fluctuations in our background templates, we generate toys from the background template from data. We then repeat the fit with each of these toys and plot the distribution of the difference between

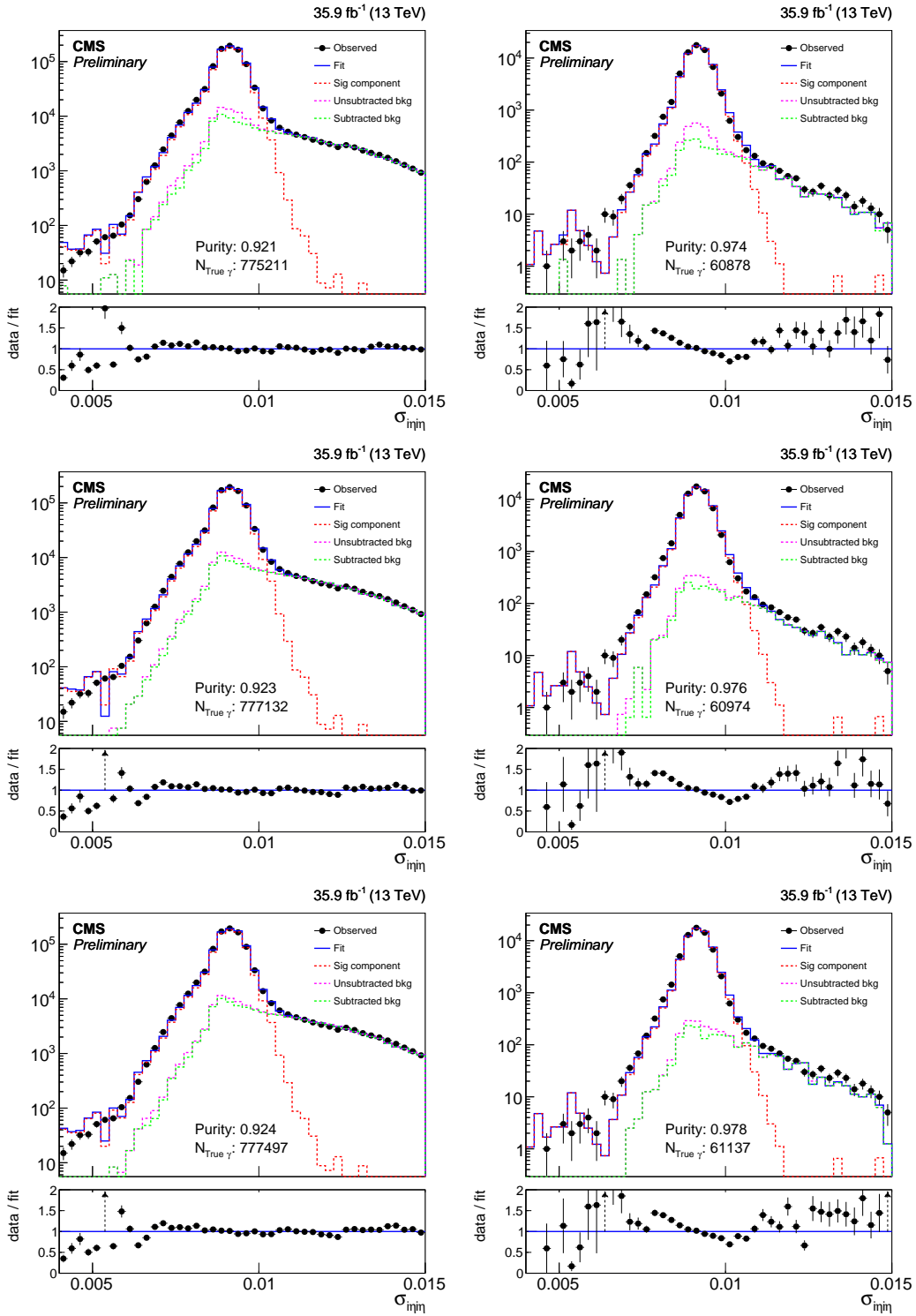


Figure 6-6: Fits to the $\sigma_{\text{inj}\eta}$ distributions for the $[175, 200]$ (left) and $[400, \infty)$ (right) p_T bins using the $[3.5, 5.0]$ (top), $[5.0, 7.5]$ (middle), and $[7.5, 9.0]$ (bottom) isolation sidebands. The blue solid line represents the full fit model, the red dashed line its signal component, and the green dashed line its background component.

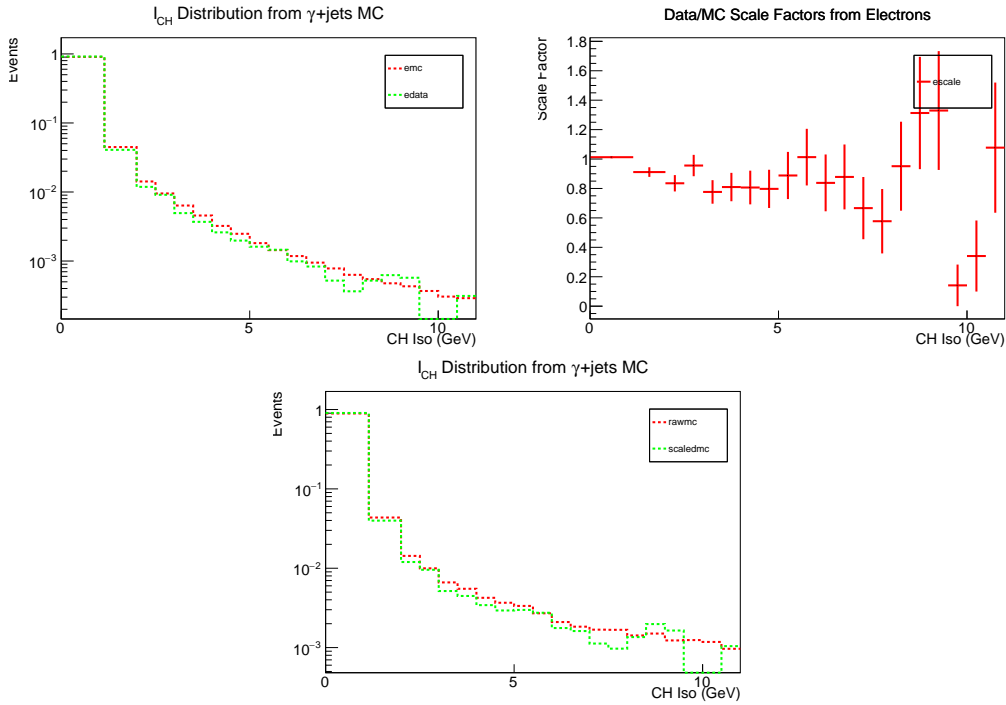


Figure 6-7: Top left: I_{CH} distributions of electrons in data and MC in $Z \rightarrow ee$ events. Top right: data/MC scale factor obtained from the electron I_{CH} distributions. Bottom: I_{CH} distributions of the MC photon objects used to estimate the amount of photon contamination in the background template, before and after applying the data/MC scale factor.

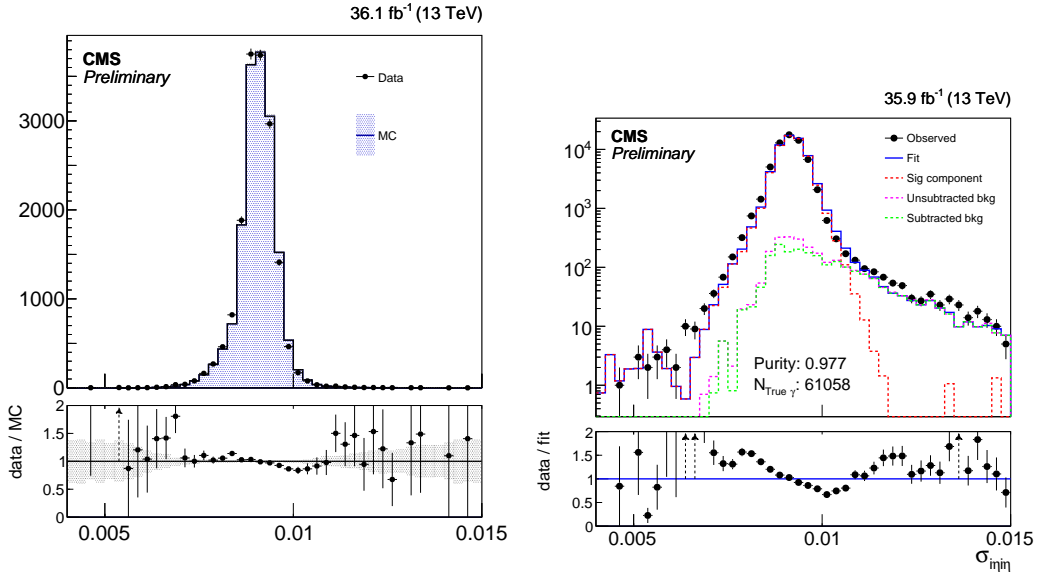


Figure 6-8: Left: Comparison of $\sigma_{i\eta i\eta}$ distributions between data and MC in $Z \rightarrow ee$ events. Lower panel shows the data/MC $\sigma_{i\eta i\eta}$ scale factor. Right: Result of the fit with true-photon template with the data/MC $\sigma_{i\eta i\eta}$ scale factor applied to the true-photon template.

the purity value obtained from the toy templates versus the nominal template. We take the standard deviation of this distribution, shown in Figure 6-9, as a systematic uncertainty.

The values obtained for each systematic uncertainty on the true photon count of the denominator are shown in Table 6.2 in bins of p_T . The relative uncertainties on the numerator are similar, and in the efficiency, each uncertainty source is considered as fully correlated.

Table 6.2: Relative uncertainties on the estimated number of true photons in the denominator sample.

p_T Range (GeV)	Sources of Systematic Uncertainty			
	Sideband	I_{CH} Shape	Signal Shape	Bkfd. Stats
(175, 200)	0.09	0.18	0.05	0.04
(200, 250)	0.01	0.16	0.06	0.03
(250, 300)	0.14	0.16	0.06	0.05
(300, 350)	0.12	0.16	0.07	0.08
(350, 400)	0.23	0.11	0.05	0.10
(400, ∞)	0.27	0.09	0.05	0.05

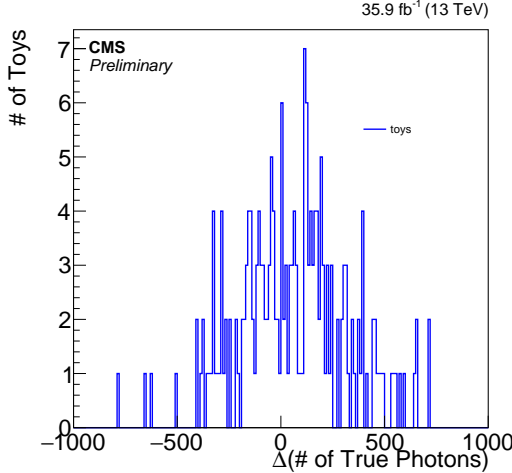


Figure 6-9: Shift in true-photon yields, extracted from alternative fits varying the background template within its statistical uncertainty. Nominal photon count in this specific E_T^γ bin is 6.64×10^5 .

The MC efficiency of the γ -specific ID is determined by counting the number of truth-matched photons passing e/γ part of the ID and the full ID. However, there is a complication, the $\gamma+jets$ region in data has approximately 5% contamination from electrons before applying the pixel veto, as shown in Figure 6-10. Thus, we combine appropriately cross-section weighted $\gamma+jets$, $W+jets$, and $t\bar{t}$ samples and truth match to both electrons and photons. Additionally, we apply a 14% uncertainty on the $W+jets$ and $t\bar{t}$ yields to account for the NLO cross-section ratio uncertainties with respect to $\gamma+jets$ at this p_T range that is uncorrelated between the numerator and denominator as a negligible amount of electron events survive the pixel veto.

The data efficiency, MC efficiency, and the scale factor for the γ -specific ID as a function of p_T are shown in Figure 6-11. As there is no significant trend in the scale factor as a function of p_T we apply a flat scale factor of 0.984 ± 0.009 for all of the MC-based background and signal models in the analysis.

6.3 Lepton Efficiency

The electron and muon efficiencies are measured using a similar method to the “tag-and-probe” method described in Section 6.2.1. For these measurements, the tag object

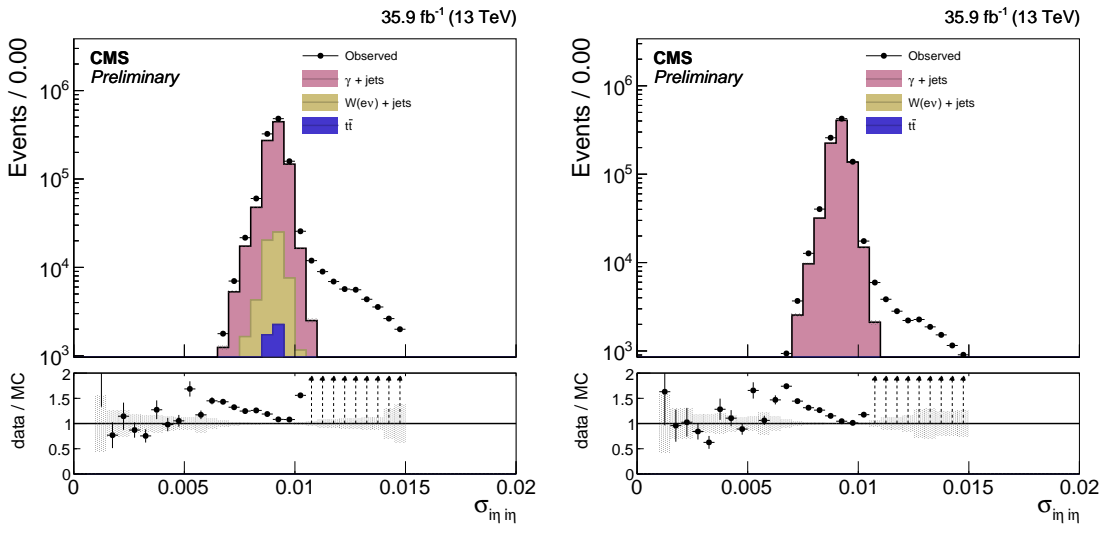


Figure 6-10: Electron contamination in $\gamma + \text{jets}$ region before (left) and after (right) applying the pixel seed veto.

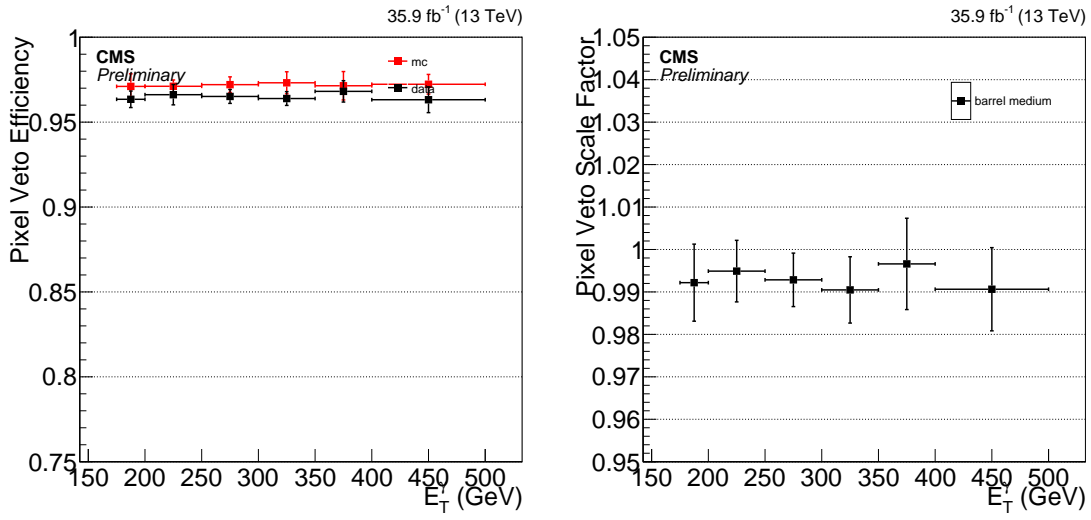


Figure 6-11: Photon pixel veto efficiencies (left) and corresponding scale factor (right) as a function of photon p_T .

is an electron (muon) object passing the tight ID described in Section 5.5 (Section 5.6) and matched to a SingleElectron (SingleMuon) trigger while the probe object is an PF electron (muon) without any ID applied. The passing (failing) categories are defined by events with probes passing (failing) the ID definition in question (see Sections 5.5 and 5.6 for details). The electron (muon) scale factors are approximately unity with a flat 2% (1%) systematic uncertainty.

6.4 Pileup Reweighting

The distribution of the number of pileup interactions inserted into MC events differ from the true pileup distribution, estimated from the measurement of instantaneous luminosity, beam intensity of each proton bunch, and the total cross section of proton inelastic scattering (69.2 mb^{-1}).

Figure 6-12 shows the pileup distributions in data and MC and their ratio. Each simulation event has its weight multiplied by the value of the ratio evaluated at the number of true pileup interaction injected into the event.

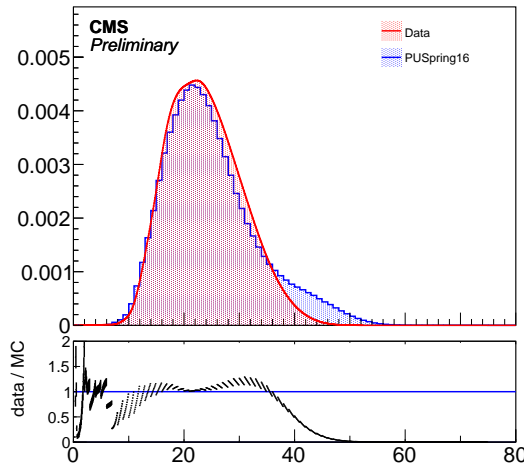


Figure 6-12: The pileup distributions in data and MC.

6.5 Lepton Veto Efficiency (Events with “Fake Leptons”)

The lepton veto requirement in the signal region has a non-unity efficiency over events that do not have genuine leptons, because particles such as pions and protons can mimic leptons (become “fake leptons”) and cause the event to be rejected. To measure the possible difference between data and MC of this lepton veto efficiency, we compare dimuon events in data and MC. In a high-purity $Z \rightarrow \mu\mu$ sample with the dimuon mass close to M_Z , events with a genuine third lepton is negligibly rare, and therefore the efficiency loss from rejecting events with a third lepton is dominantly due to fake leptons.

For this measurement, collision events are taken from the SingleMuon data set and the MC events from a mixture of DY, $t\bar{t}$, WW , WZ , and ZZ samples. We require two muons passing the “tight” identification working point defined in Section 5.6 with the mass between 61 and 121 GeV. These events are then checked for additional electron or muon objects passing the loose selection criteria defined in Sections 5.5 or 5.6, respectively. The efficiency is inspected as a function of number of vertices, number of jets, and H_T in the event, and in all cases data and MC are consistent as shown in Figure 6-13.

It should be noted, however, that the absolute lepton veto efficiency in MC dimuon sample is significantly different from that of the $Z(\rightarrow \nu\bar{\nu})+\gamma$ sample, which more closely features the properties of the signal candidate sample. The full difference in the efficiencies between the dimuon and $Z(\rightarrow \nu\bar{\nu})+\gamma$ samples is tentatively taken as the systematic uncertainty in the lepton veto scale factor, which is therefore 1.00 ± 0.02 .

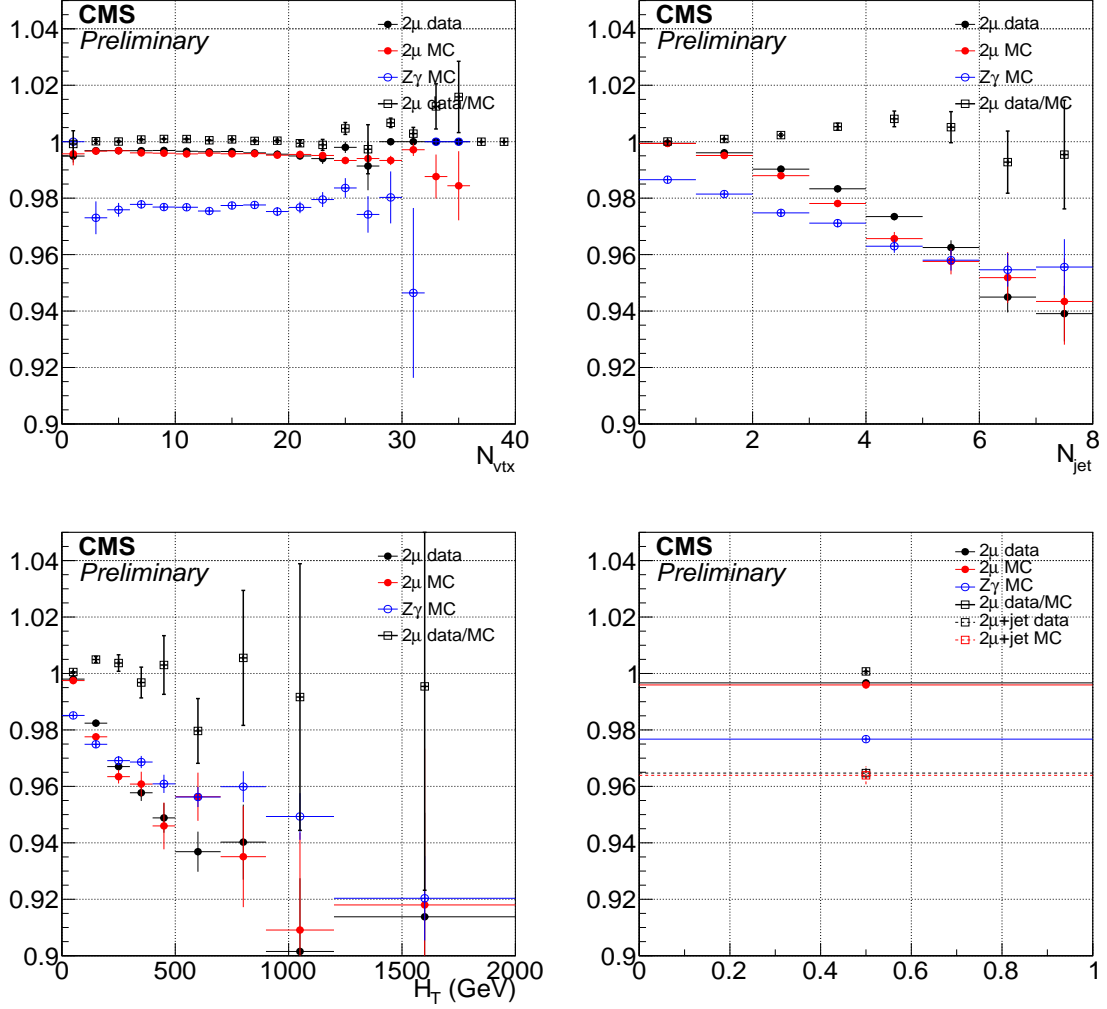


Figure 6-13: Lepton veto efficiencies and data/MC scale factors as functions of N_{vtx} , N_{jet} , and H_T , and the corresponding inclusive values. While dimuon and $Z(\rightarrow \nu\bar{\nu})+\gamma$ samples have significantly different efficiencies, data and MC agree well within dimuon samples, giving scale factors consistent with 1 almost everywhere. This is true even when additionally requiring a high- p_T jet in the event, as seen in the inclusive efficiency plot. Thus, the difference between $Z(\rightarrow \nu\bar{\nu})+\gamma$ and dimuon efficiencies itself is taken as the uncertainty.

6.6 Lepton Veto Efficiency (Events with “Real Leptons”)

Additionally, a small fraction of events with real leptons pass the lepton veto due to the leptons failing the loose ID requirements. This effect is most relevant for $W(\rightarrow \ell\nu)+\gamma$ events in the signal region and for $Z(\rightarrow \ell\bar{\ell})+\gamma$ events in the single lepton control regions. We account for this effect in the following way:

Using the data and MC efficiencies from Section 6.3 for the loose IDs, we compute a scalefactor $SF_{\text{veto}} = (1. - \epsilon_{\text{data}})/(1. - \epsilon_{\text{MC}})$ and apply this to MC events with a reconstructed lepton that fails the loose ID. If there are multiple such leptons in an event, we apply this scalefactor only for the hardest muon and electron. We apply a flat 1% (5%) uncertainty for the muon (electron) efficiencies.

The veto scale factors for electrons (muons) range from 0.55 to 1.38 (0.34 to 73.5) with uncertainties ranging from 0.15 to 1.46 (2.7 to 126.8). All scale factors are consistent with unity within the uncertainties. After applying the scale factors, the final MC yields for $W(\rightarrow \ell\nu)+\gamma$ in the signal region and $Z(\rightarrow \ell\bar{\ell})+\gamma$ in the single lepton control regions change by less than 0.5%.

Chapter 7

The Monophoton Analysis

There are multiple distinct sources of SM background to this analysis. The most significant of them are the irreducible backgrounds, which are the associated production of a high-energy γ with either a Z boson that subsequently decays to a pair of neutrinos or a W boson that decays to a charged lepton and a neutrino. These two processes are denoted as $Z(\rightarrow \nu\bar{\nu})+\gamma$ and $W(\rightarrow \ell\nu)+\gamma$, respectively, and together they account for approximately 70% of the SM background, with 50% from the former and 20% from the latter. The total irreducible background rate is estimated using simultaneous fits to the signal and control regions defined in Section 7.1 and the details of the modeling are given in Section 7.2.

Less significant but non-negligible backgrounds arise from events where the candidate photon object is a misidentified electron (Section 7.3) or electromagnetic shower caused by hadrons (Section 7.4). The background events from electron misidentification are mostly W boson production ($W \rightarrow e\nu$), whereas those from hadron misidentification can be due to multiple sources such as $Z(\rightarrow \nu\nu) + \text{jets}$ and QCD multijets with grossly mismeasured jet energy. Misidentification itself is rare, but all of the above processes have high cross sections. Since object misidentification rates depend on subtle details of the detector, the MC simulation cannot be expected to model it reliably. Therefore, data-driven techniques are employed to estimate the contributions from these background events.

After the full selection described in Section 7.1, the SM $\gamma+\text{jets}$, $t\bar{t}\gamma$, $VV\gamma$, $Z(\rightarrow$

$\ell\bar{\ell})+\gamma$, and $W \rightarrow \ell\nu$ processes are minor ($\sim 10\%$) background processes in the signal region. These processes, collectively denoted as minor SM backgrounds, can contribute in the signal region if the jet energy is severely mismeasured or the leptons fail to be reconstructed resulting in large E_T^{miss} in the signal region. However, the E_T^{miss} is typically aligned with the photon or one of the jets in such cases, and therefore various selections on the kinematic relations between the E_T^{miss} , photons, and jets are used to reduce these backgrounds to a manageable rate. The estimates for all five processes are taken from MADGRAPH5_aMC@NLO simulations at LO in QCD and can be found in Tables 7.4 and 7.5.

Finally, apparent large energy deposits in ECAL from non-collision processes can mimic $\gamma+E_T^{\text{miss}}$ events and therefore need to be controlled. Known sources of such background include bremsstrahlung of beam halo or cosmic ray muons and anomalous ECAL energy deposits resulting from the interaction of particles in the ECAL photodetectors referred to as “ECAL spikes”. These processes are described in detail in Sections 7.5 and 5.10, respectively.

All background processes except for the two irreducible ones and beam halo are given absolute estimates from data-driven methods or MC cross section calculations. The estimates of the contributions from $Z(\rightarrow \nu\bar{\nu})+\gamma$, $W(\rightarrow \ell\nu)+\gamma$, and beam halo processes are allowed to float in the final fit to data performed to extract the potential signal contribution described in Section 7.7.

7.1 Event Selection

The integrated luminosity of the analyzed data sample is $(35.9 \pm 0.9) \text{ fb}^{-1}$ [?]. The data sample is collected with a single-photon trigger that requires at least one photon candidate with $p_T > 165 \text{ GeV}$. The photon candidate must have $H/E < 0.1$ to discriminate against jets, where H/E is the ratio of HCAL to ECAL energy deposits in the central calorimeter tower corresponding to the candidate. The photon energy reconstructed at the HLT is less precise relative to that derived later in the offline reconstruction. Therefore, the thresholds in the trigger on both H/E and E_T^γ , are

less restrictive than their offline counterparts. The trigger efficiency is measured to be about 98% for events passing the analysis selection with $E_T^\gamma > 175 \text{ GeV}$.

From the recorded data, events are selected by requiring $E_T^{\text{miss}} > 170 \text{ GeV}$ and at least one photon with $E_T^\gamma > 175 \text{ GeV}$ in the fiducial region of the ECAL barrel ($|\eta| < 1.44$) passing the selected presented in Section 5.4.

Events with a high- p_T photon and large E_T^{miss} are subjected to further requirements to suppress SM background processes that feature a genuine high-energy photon, but not a significant amount of E_T^{miss} . One such SM process is $\gamma + \text{jets}$, where an apparent large E_T^{miss} is often the result of a mismeasured jet energy. In contrast to signal processes, E_T^{miss} is typically smaller than E_T^γ in these events, so requiring the ratio of E_T^γ to E_T^{miss} to be less than 1.4 rejects this background effectively with little effect on signal efficiency. Events are also rejected if the minimum opening angle between \vec{p}_T^{miss} and the directions of the four highest p_T jets, $\min\Delta\phi(\vec{p}_T^{\text{jet}}, \vec{p}_T^{\text{miss}})$, is less than 0.5. Only jets with $p_T > 30 \text{ GeV}$ and $|\eta| < 5$ are considered in the $\min\Delta\phi(\vec{p}_T^{\text{jet}}, \vec{p}_T^{\text{miss}})$ calculation. In the $\gamma + \text{jets}$ process, rare pathological mismeasurement of E_T^γ can also lead to large E_T^{miss} . For this reason, the candidate photon \vec{p}_T and \vec{p}_T^{miss} must be separated by more than 0.5 radians. Another SM process to be rejected is $W(\rightarrow \ell\nu) + \gamma$, for which events are vetoed if they contain an electron or a muon with $p_T > 10 \text{ GeV}$ that is separated from the photon by $\Delta R > 0.5$. Furthermore, using features described in Section 7.5, the signal region is split into two parts according to ϕ to constrain the beam halo normalization. The region defined by $|\sin(\phi)| < \sin(0.5)$ is called the horizontal region, and its complement in ϕ is called the vertical region.

The residual contributions from the $W(\rightarrow \ell\nu) + \gamma$ process, where the lepton could not be identified or was out of the detector acceptance, are modeled by fitting to observed data, as described in Section 7.2. The same method is employed to model the contribution from the $Z(\rightarrow \nu\bar{\nu}) + \gamma$ process to the signal region. This method utilizes control regions where one or two leptons (electrons or muons) are identified in addition to the photon, as defined in the following.

The single-electron (single-muon) control region is defined by a requirement of exactly one electron (muon) with $p_T > 30 \text{ GeV}$ and $|\eta| < 2.5$ (2.4) in addition to a

photon requirement that is identical to the one for the signal region. To suppress the contributions from large- $E_{\mathrm{T}}^{\text{miss}}$ processes other than $W(\rightarrow \ell\nu)+\gamma$, the transverse mass $m_{\mathrm{T}} = \sqrt{2E_{\mathrm{T}}^{\text{miss}} p_{\mathrm{T}}^{\ell} [1 - \cos \Delta\phi(\vec{p}_{\mathrm{T}}^{\text{miss}}, \vec{p}_{\mathrm{T}}^{\ell})]}$ must be less than 160 GeV. Additionally, for the single-electron control region, $E_{\mathrm{T}}^{\text{miss}}$ must be greater than 50 GeV to limit the contribution from the $\gamma+\text{jets}$ process, where a jet is misidentified as an electron. Finally, the recoil vector $\vec{U} = \vec{p}_{\mathrm{T}}^{\text{miss}} + \sum \vec{p}_{\mathrm{T}}^{\ell}$, which serves as this region’s analogue for $\vec{p}_{\mathrm{T}}^{\text{miss}}$ in the signal region, must satisfy identical requirements to those for the $\vec{p}_{\mathrm{T}}^{\text{miss}}$ in the signal region.

The dielectron (dimuon) control region is defined by exactly two electrons (muons) in addition to the photon, with $60 < m_{\ell\ell} < 120$ GeV, where $m_{\ell\ell}$ is the invariant mass of the dilepton system. The recoil vector of this region is $\vec{U} = \vec{p}_{\mathrm{T}}^{\text{miss}} + \sum \vec{p}_{\mathrm{T}}^{\ell}$ and must satisfy identical requirements to those for the $\vec{p}_{\mathrm{T}}^{\text{miss}}$ in the signal region.

7.2 Irreducible backgrounds

7.2.1 Simulation of $V+\gamma$ Processes

The $Z(\rightarrow \nu\bar{\nu})+\gamma$ and $W(\rightarrow \ell\nu)+\gamma$ background contributions are modeled using MC simulations. Samples generated at the leading order (LO) in QCD by MADGRAPH 5 with up to two additional partons and a generator-level requirement of $E_{\mathrm{T}}^{\gamma} > 130$ GeV are employed for this purpose.

A study using a privately generated aMC@NLO sample with high E_{T}^{γ} threshold confirms that the predicted kinematic distributions would not change drastically by using the NLO sample. Figures 7-1 and 7-2 show the comparisons of the private aMC@NLO samples and the MADGRAPH 5 samples used for the background estimation in the key kinematic distributions.

To approximate the QCD higher-order effects, $Z(\rightarrow \nu\bar{\nu})+\gamma$ and $W(\rightarrow \ell\nu)+\gamma$ events are reweighted with E_{T}^{γ} by the factors given in Tab. 7.1. These factors are the ratios of QCD next-to-next-to leading order (NNLO) differential cross sections calculated by Grazzini et al. [?] to the LO cross sections given in the centrally pro-

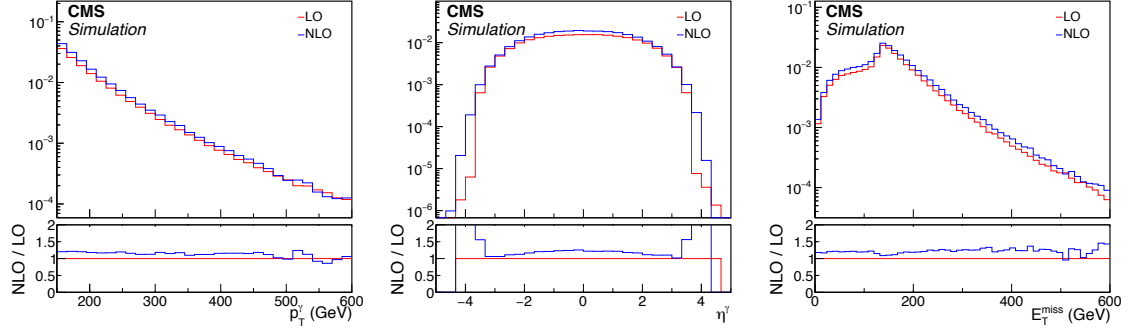


Figure 7-1: Distributions of E_T^γ (left), η^γ (middle), and p_T^Z (right) in $Z(\rightarrow \nu\bar{\nu}) + \gamma$ process from the private aMC@NLO sample (blue) and the LO sample used for background prediction (red) along with the NLO / LO ratios.

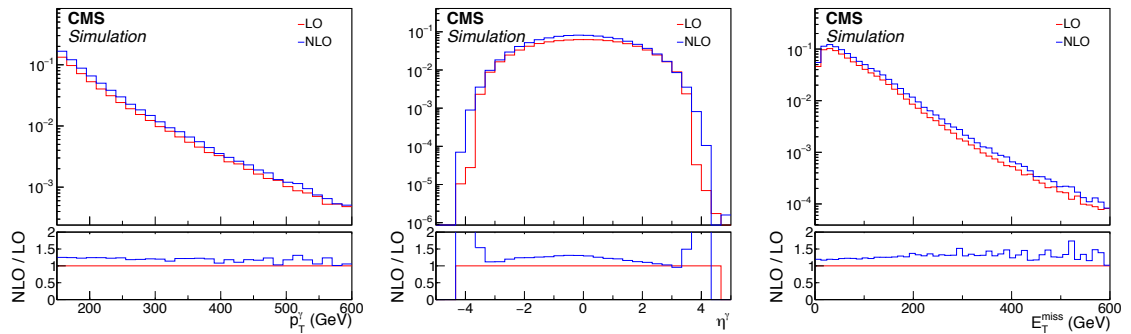


Figure 7-2: Distributions of E_T^γ (top left), η^γ (top right), and p_T^W (bottom left) in $W(\rightarrow \ell\nu) + \gamma$ process from the private aMC@NLO sample (blue) and the LO sample used for background prediction (red) along with the NLO / LO ratios.

Table 7.1: NNLO / LO correction factors for $Z(\rightarrow \nu\bar{\nu})+\gamma$ and $W(\rightarrow \ell\nu)+\gamma$ samples.

E_T^γ range (GeV)	$Z(\rightarrow \nu\bar{\nu})+\gamma$	$W(\rightarrow \ell\nu)+\gamma$
[175, 190]	1.44	1.40
[190, 250]	1.41	1.37
[250, 400]	1.35	1.31
[400, 700]	1.29	1.26
[700, inf]	1.15	1.15

duced samples. (Note that the denominator cross section includes contributions from processes with up to two additional partons, and is therefore not a LO cross section in the strict sense of the word. $V\gamma$ k-factors found in literature can be $\gg 1$ at high E_T^γ , if the denominator only accounts for the cross section of $q\bar{q} \rightarrow V\gamma$ process.)

Additionally, higher-order electroweak correction factors are also applied as a function of E_T^γ . Out of various electroweak higher-order effects, ones that can give sizeable ($\gg \mathcal{O}(\alpha)$) corrections to the cross section are Sudakov suppression at high boson p_T and potentially the addition of photon-induced scattering processes [?, ?]. We apply the correction factors shown in Figure 7-3, which are combinations of Sudakov suppression factors and photon-induced enhancements, and are provided by the authors of Ref. [?] in addition to the NNLO QCD correction.

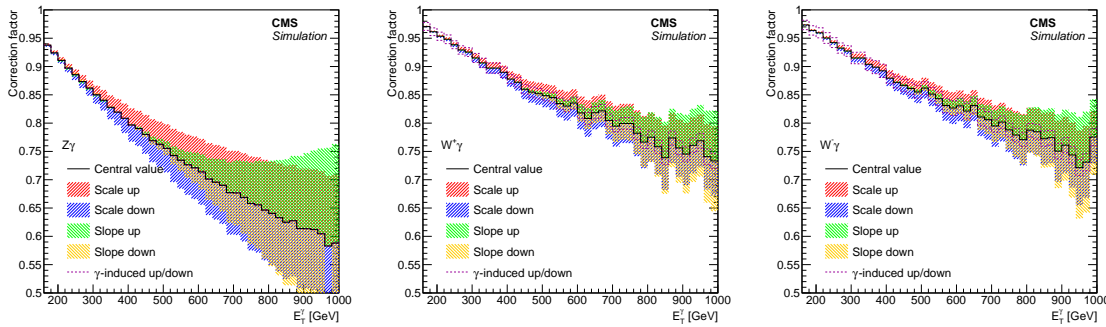


Figure 7-3: Electroweak NLO cross section corrections as a function of photon p_T for $Z(\rightarrow \nu\bar{\nu})+\gamma$ (left), $W^+ + \gamma$ (middle), and $W^- + \gamma$ (right) processes, overlaid with uncertainty bands. See text for descriptions of the individual components of the uncertainty. The uncertainty due to γ -induced production is negligible in $Z(\rightarrow \nu\bar{\nu})+\gamma$ production.

The differential cross section after the full higher-order corrections is therefore

denoted as

$$d\sigma^{\text{NNLO QCD+NLO EW}} = d\sigma^{\text{LO}} k^{\text{NNLO QCD}} (1 + \kappa^{\text{EW Sudakov}} + \kappa^{\text{EW}q\gamma}), \quad (7.1)$$

where $k^{\text{NNLO QCD}} = d\sigma^{\text{NNLO QCD}}/d\sigma^{\text{LO}}$, and the two κ terms are the Sudakov suppression and photon-induced enhancement components of the electroweak correction, respectively.

Furthermore, subtle differences between simulation and observation in the reconstruction and identification efficiencies for various particle candidates are accounted for with the set of selection efficiency correction factors ρ . The value of an individual ρ typically lies within a few percent of unity. Further details on the measurement and values of various ρ are found in Chapter 6.

Four sources of systematic uncertainties considered for E_T^γ distribution ratios of the $V+\gamma$ processes are higher-order QCD corrections, higher-order EWK corrections, choice of PDF set, and data-to-simulation correction factors ρ . The four uncertainties are all considered as correlated between the E_T^γ bins.

The higher-order QCD renormalization and factorization scale uncertainties on the NNLO cross sections are assessed by varying the respective scales by factor 2 and 0.5 during the cross section computation. These uncertainties are between 7-8%, varying bin by bin, and are considered uncorrelated in the ratio between the $Z(\rightarrow \nu\bar{\nu})+\gamma$ and $W(\rightarrow \ell\nu)+\gamma$ processes.

Theoretical uncertainties on the electroweak corrections are not well understood to date. We estimate the magnitude of the uncertainty on $\kappa^{\text{EW Sudakov}}$ and $\kappa^{\text{EW}q\gamma}$ to be $(\kappa^{\text{EW Sudakov}})^2$ and $\kappa^{\text{EW}q\gamma}$, i.e., square of the correction for Sudakov suppression and the 100% of the correction itself for the photon-induced enhancement. The choice of using the square of $\kappa^{\text{EW Sudakov}}$ is motivated by the fact that fully resummed leading-log Sudakov suppression is an exponential of $\kappa^{\text{EW Sudakov}}$.

For the Sudakov suppression, which is the dominant term in the electroweak correction, we further consider two types of systematic variations, inspired by ref. [?], which provides a prescription for electroweak correction uncertainties for $V + \text{jets}$

processes. In this paper, electroweak correction as a function of the boson p_T is varied in overall scale and in slope. The slope variation is realized by selecting a point in the boson p_T spectrum and letting the shift in correction cross over at the point (see Figure 7-4). Following this prescription, we let the Sudakov suppression vary in overall scale and in slope, where we choose our crossover point for the slope variation to be at $E_T^\gamma = 590 \text{ GeV}$.

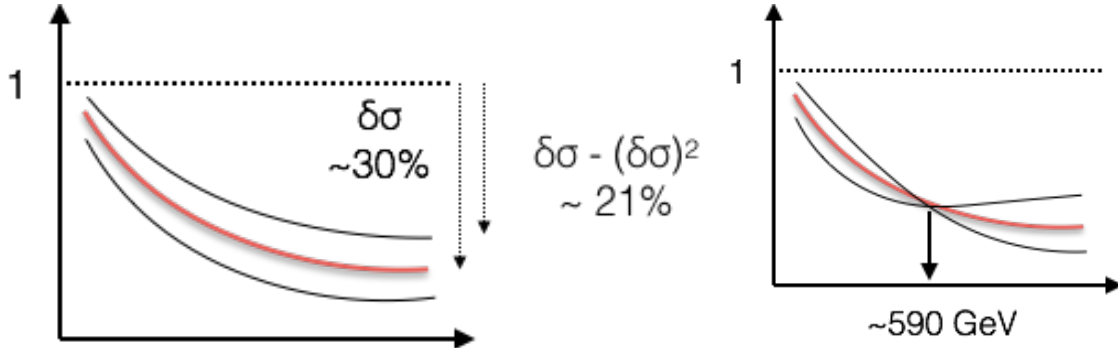


Figure 7-4: Electroweak correction variation scheme to cover the scale (left) and shape (right) uncertainties.

The PDF uncertainty is evaluated by varying the weight of each event using the weights provided in the NNPDF set, and taking the standard deviation of the resulting E_T^γ distributions. This uncertainty is considered fully correlated in the ratio between the $Z(\rightarrow \nu\bar{\nu})+\gamma$ and $W(\rightarrow \ell\nu)+\gamma$ processes, i.e., the variation of the ratio is bounded by the ratios of the upward and downward variations.

Finally, data-to-simulation correction factors ρ for the lepton identification efficiencies have associated uncertainties that do not cancel when taking ratios between regions defined by different lepton selection requirements.

7.2.2 Data-driven Control Regions

Contributions from the $Z(\rightarrow \nu\bar{\nu})+\gamma$ and $W(\rightarrow \ell\nu)+\gamma$ processes are estimated using observed data in four mutually exclusive single-electron, single-muon, dielectron, and dimuon control regions defined in Section 7.1. The ratios between the expected yields of these processes are constrained by MC simulations of $V+\gamma$ processes. This background estimation method exploits cancellation of some of the systematic uncertain-

ties, both experimental and theoretical, in the ratios of the photon E_T^γ distributions of $V+\gamma$ processes, from here on referred to as “transfer factors”.

For example, in the transfer factor between the $Z(\rightarrow \nu\bar{\nu})+\gamma$ and $Z(\rightarrow \ell\bar{\ell})+\gamma$ processes, denoted $R_{\ell\ell\gamma}^{Z\gamma}$, the uncertainties due to photon energy calibration, jet energy resolution, and higher-order QCD effects are significantly reduced compared to when such effects are considered for individual processes. The only uncertainties in the transfer factor $R_{\ell\ell\gamma}^{Z\gamma}$ that do not largely cancel are those on lepton identification efficiency and the statistical uncertainty due to the limited MC sample size. Figure 7-5 shows the transfer factor $R_{ee\gamma}^{Z\gamma}$ ($R_{\mu\mu\gamma}^{Z\gamma}$) between the dielectron (dimuon) control region and the combined signal regions, for which the numerator is the expected $Z(\rightarrow \nu\bar{\nu})+\gamma$ yield in the combined signal regions and the denominator is the expected $Z(\rightarrow \ell\bar{\ell})+\gamma$ yield in the relevant control region.

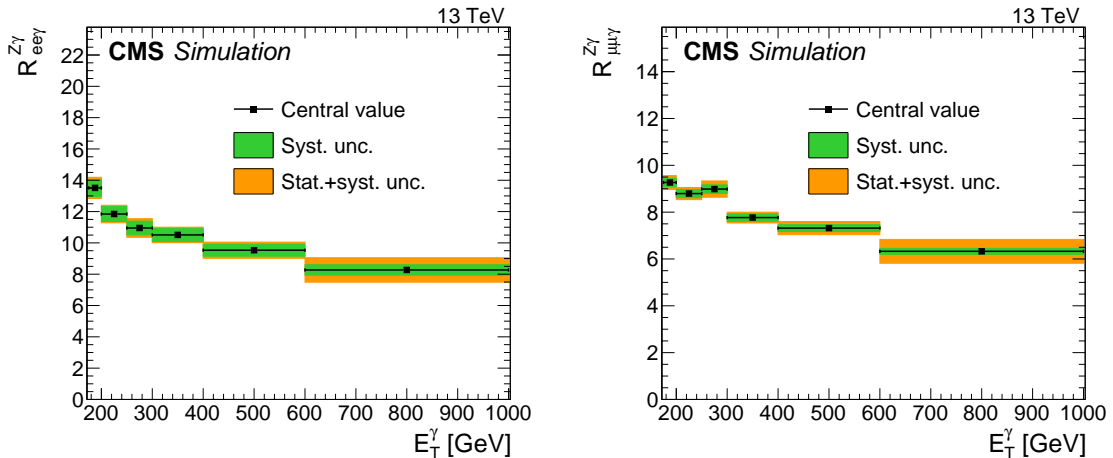


Figure 7-5: Transfer factors $R_{ee\gamma}^{Z\gamma}$ (left) and $R_{\mu\mu\gamma}^{Z\gamma}$ (right). The uncertainty bands in green (inner) and orange (outer) show the systematic uncertainty, and the combination of systematic and statistical uncertainty arising from limited MC sample size, respectively. The systematic uncertainties considered are the uncertainties in the data-to-simulation correction factors ρ for the lepton identification efficiencies.

For increasing E_T^γ , the Z boson in a $Z(\rightarrow \ell\bar{\ell})+\gamma$ event tends to emerge with lower rapidity, and hence so do its decay products. As a consequence, the charged leptons are more likely to fall within the inner tracker acceptance, which increases the dilepton control region selection efficiency of these events. In contrast, the signal

region selection efficiency of $Z(\rightarrow \nu\bar{\nu})+\gamma$ events is unaffected by the rapidity of the final state neutrinos, as long as the observed E_T^{miss} has the appropriate magnitude and azimuthal direction. This causes the distinctive drop in the ratio $R_{\ell\ell\gamma}^{Z\gamma}$ with increasing E_T^γ .

Using the transfer factor $R_{\ell\ell\gamma}^{Z\gamma}$, the total estimated event yield $T_{\ell\ell\gamma}$ in each dilepton control region in the i^{th} bin of the E_T^γ distribution can be expressed as

$$T_{\ell\ell\gamma,i} = \frac{N_i^{Z\gamma}}{R_{\ell\ell\gamma,i}^{Z\gamma}} + b_{\ell\ell\gamma,i}, \quad (7.2)$$

where $N^{Z\gamma}$ is the number of $Z(\rightarrow \nu\bar{\nu})+\gamma$ events in the combined signal regions and $b_{\ell\ell\gamma}$ is the predicted contribution from other background sources in the dilepton control region, namely $t\bar{t}\gamma$, $VV\gamma$, and misidentified hadrons. The subscript i indicates that the quantities are evaluated in bin i of the E_T^γ distribution.

Similar considerations apply to events arising from $W(\rightarrow \ell\nu)+\gamma$ processes. A large fraction of such events are rejected by the electron and muon vetoes in the signal region selection and end up in the control regions instead. However, hadronic tau events and events where the leptons are out of acceptance or fail to be reconstructed will remain in the signal region, on top of the vetoes having imperfect efficiencies. In the ratio of these two classes of events, denoted $R_{\ell\gamma}^{W\gamma}$, the only uncertainties that remain non-negligible are those associated with the lepton identification efficiency and the MC statistical uncertainty.

Table 7.2 gives the breakdown of the $W(\rightarrow \ell\nu)+\gamma$ background passing the full event selection for the signal region, categorized by the lepton flavor and, for the case of electrons and muons, the lepton pseudorapidity at the parton-level. From this breakdown, one sees that events where the W boson decays to a τ and a neutrino constitutes approximately 60% of the $W(\rightarrow \ell\nu)+\gamma$ background. The remaining 40% of the $W(\rightarrow \ell\nu)+\gamma$ background comes from events where W boson decays to a μ or e and a neutrino. Events containing an electron are more likely to be within the detector acceptance, while those with a muon are more likely to be out of acceptance. For the in-acceptance background ($|\eta| < 2.5$), the identification efficiency, which is lower

Table 7.2: The breakdown of simulated $W + \gamma$ events passing the full event selection. Events are categorized in the W decay mode. Events with $e\nu$ and $\mu\nu$ final states are further divided into those where the lepton was roughly within acceptance ($|\eta| < 2.5$) but failed the lepton veto, and those where the lepton was out of acceptance ($|\eta| > 2.5$). For each W decay mode, the fraction out of total generated ($A \times \epsilon$) is shown.

Subprocess	$A \times \epsilon \times 10^3$
$W \rightarrow e\nu + \gamma$	1.68
$ \eta^e < 2.5$	1.35
$ \eta^e > 2.5$	0.32
$W \rightarrow \mu\nu + \gamma$	1.83
$ \eta^\mu < 2.5$	0.74
$ \eta^\mu > 2.5$	1.08
$W \rightarrow \tau\nu + \gamma$	5.03

for electrons than for muons, which translates to a larger background contribution from the electrons. Meanwhile, the E_T^{miss} requirement explains the behavior of the out-of-acceptance background ($|\eta| > 2.5$). A large fraction of electrons that are out of tracker acceptance are still captured by the calorimeters, while out-of-acceptance muons directly contribute to missing momentum leading to a larger background contribution from muons.

Figure 7-6 shows the transfer factor $R_{e\gamma}^{W\gamma}$ ($R_{\mu\gamma}^{W\gamma}$) between the single-electron (single-muon) control region and the combined signal regions, for which the numerator is the estimated $W(\rightarrow \ell\nu) + \gamma$ yield in the combined signal regions, and the denominator is the estimated $W(\rightarrow \ell\nu) + \gamma$ yield in the relevant control region. The ratio $R_{e\gamma}^{W\gamma}$ decreases with increasing E_T^γ in a similar manner to $R_{\ell\ell\gamma}^{Z\gamma}$. The underlying logic is the same; e.g., that the signal region selection efficiency is unaffected by E_T^γ while the control region acceptances increase with increasing E_T^γ due to increased lepton efficiency resulting from lower W rapidity.

Finally, to benefit further from the larger statistical power that the single-lepton control samples provides, an additional transfer factor $f_{W\gamma}^{Z\gamma} = N^{Z\gamma}/N^{W\gamma}$ is defined to connect the $Z(\rightarrow \nu\bar{\nu}) + \gamma$ and $W(\rightarrow \ell\nu) + \gamma$ background yields in the signal regions, where the quantity $N^{W\gamma}$ is the number of $W(\rightarrow \ell\nu) + \gamma$ events in the combined signal regions. When calculating the ratio $f_{W\gamma}^{Z\gamma}$, all experimental uncertainties associated

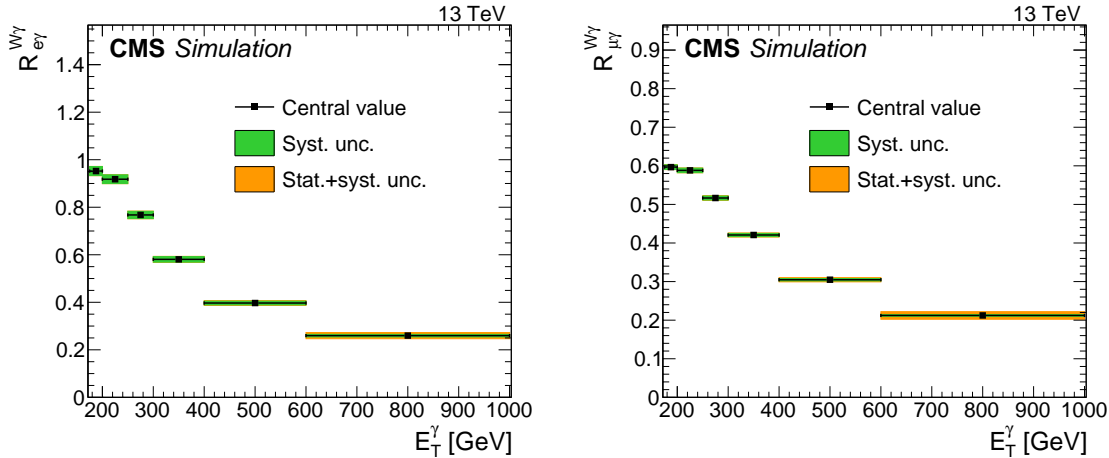


Figure 7-6: Transfer factors $R_{e\gamma}^{W\gamma}$ (left) and $R_{\mu\gamma}^{W\gamma}$ (right). The uncertainty bands in green (inner) and orange (outer) show the systematic uncertainty, and the combination of systematic and statistical uncertainty arising from limited MC sample size, respectively. The systematic uncertainties considered are the uncertainties in the data-to-simulation correction factors ρ for the lepton identification efficiencies.

with the data-to-simulation correction factors ρ cancel since both processes result in very similar event configurations. The main uncertainties in $f_{W\gamma}^{Z\gamma}$ are those from higher-order theoretical corrections, discussed in Section 7.2.1. Figure 7-7 shows the effect of each systematic uncertainty in $f_{W\gamma}^{Z\gamma}$ with respects to its nominal value for $Z(\rightarrow \nu\bar{\nu})+\gamma$ and $W(\rightarrow \ell\nu)+\gamma$ respectively.

The ratio $f_{W\gamma}^{Z\gamma}$ rises rather than falls with increasing E_T^γ because $W(\rightarrow \ell\nu)+\gamma$ events have a lower rather than higher signal region selection efficiency if the charged lepton falls within the tracker acceptance while the $Z(\rightarrow \nu\bar{\nu})+\gamma$ efficiency is independent of E_T^γ . Figure 7-8 shows the transfer factor $f_{W\gamma}^{Z\gamma}$ between the $Z(\rightarrow \nu\bar{\nu})+\gamma$ and $W(\rightarrow \ell\nu)+\gamma$ processes in the combined signal region.

Using $R_{e\gamma}^{W\gamma}$ and $f_{W\gamma}^{Z\gamma}$, the total estimated event yield $T_{\ell\gamma}$ in each single-lepton control region in the i^{th} bin of the E_T^γ distribution can be expressed as

$$T_{\ell\gamma,i} = \frac{N_i^{Z\gamma}}{R_{\ell\gamma,i}^{W\gamma} f_{W\gamma,i}^{Z\gamma}} + b_{\ell\gamma,i}, \quad (7.3)$$

where $b_{\ell\gamma}$ is the predicted contribution from other background sources in the single-lepton regions, namely misidentified electrons and hadrons and other minor SM pro-

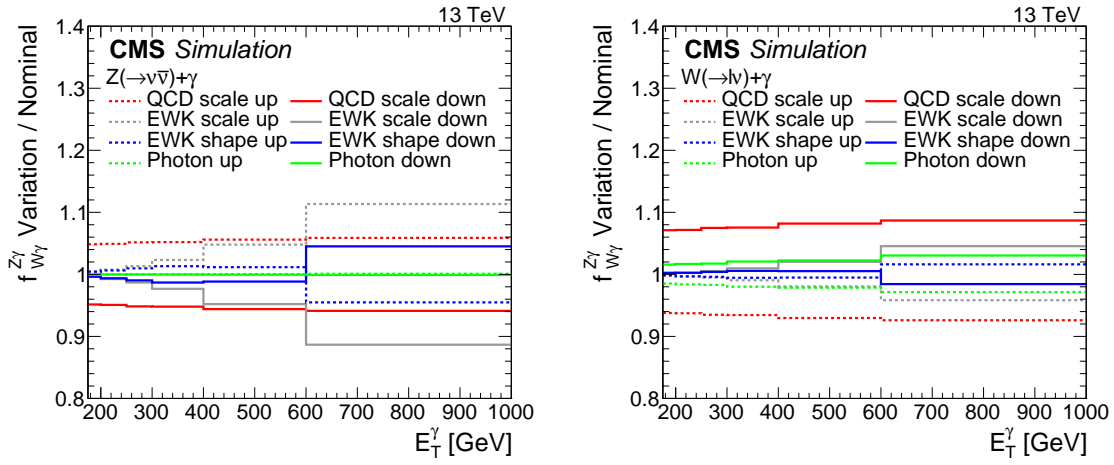


Figure 7-7: Systematic uncertainty in the transfer factors for $Z(\rightarrow \nu\bar{\nu})+\gamma$ (left) and $W(\rightarrow \ell\nu)+\gamma$ (right). The last bin includes all events with $E_T^\gamma > 1000$ GeV.

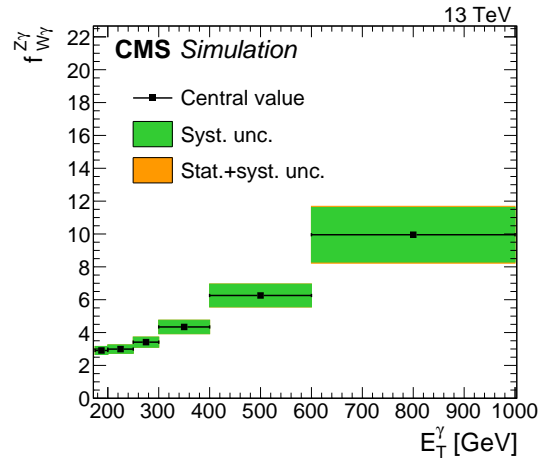


Figure 7-8: Transfer factor $f_{W\gamma}^{Z\gamma}$. The uncertainty bands in green (inner) and orange (outer) show the systematic uncertainty, and the combination of systematic and statistical uncertainty arising from limited MC sample size, respectively. The systematic uncertainties considered are the uncertainties from higher-order theoretical corrections.

cesses.

7.3 Misidentified electrons

An electron can be misidentified as a photon if the association of tracks or track seeds to the supercluster in ECAL fails in the reconstruction step. The production of a single W boson decaying to an electron and a neutrino is a high-rate process, and it mimicks the photon plus E_T^{miss} signature if the electron is misidentified.

The rate at which this misidentification occurs is proportional to the inefficiency $1 - \epsilon_e^{\text{track}}$ of the tracking, defined over the electrons passing the photon identification criteria described in Sec. 5.4 except the electron veto. This partial identification is denoted as $e\gamma$ ID in the following. If one assumes that the kinematic and other critical properties of the electron plus E_T^{miss} events are unaffected by the electron misidentification, it is possible to model the electron misidentification background by taking a proxy sample with well-identified electrons and scaling this sample by $R_e = (1 - \epsilon_e^{\text{track}})/\epsilon_e^{\text{track}}$.

The “tag-and-probe” method described in Section 6.2.1 with appropriate changes is used to measure the efficiency corresponding to the factor R_e in data.

The first such change is that the sample is split into $e\gamma$ and ee categories depending on whether the probe passes or fails the electron veto requirement. Probes in both categories must also pass the $e\gamma$ ID. Denoting the area of the peak in each category $N_{e\gamma}$ and N_{ee} , respectively, the ratio $N_{e\gamma}/N_{ee}$ is equal to R_e up to minor systematic corrections.

The second such change is in the background model used in the TP fits. The backgrounds to the $e\gamma$ fit consist of processes with actual electron and photon in the final state, such as $W\gamma$ and $Z \rightarrow ee$ with a hard radiation off one of the electrons. Because of this, we scale the mass distribution of the $\mu + \gamma$ sample by the ratio of electron-probe to muon-probe events taken from MC to account for the different rates of FSR and bremsstrahlung between muons and electrons. As an alternative template to assess the systematic effect introduced by the choice of the background template,

the unscaled mass distribution is also tested.

Figure 7-9 shows the six fits performed on ee and $e\gamma$ in bins of probe p_T , from which the R_e factor used for the estimation of the electron misidentification background is derived.

The proxy sample for the background estimation is obtained by identical event selection as that described in Sec. 7.1, but with the pixel-seed veto inverted on the photon candidate object.

Figure 7-10 shows the derived R_e factor as a function of E_T^γ . The electron proxy sample is reweighted by R_e depending on the p_T of the electron object.

7.4 Misidentified hadrons

The estimation of hadron misidentification background proceeds in multiple steps. First, the fraction of hadronic objects within a pool of photon candidate objects in the photon plus jet control region is measured. This measurement is described in detail in Section 6.2.2. Figure 7-11 and Table 7.3 show the final impurity and associated uncertainties as a function of p_T .

p_T (GeV)	Nominal	Sources of Systematic Uncertainty				
		Sideband	CH	Iso	Shape	Bgkd. Stats
(175, 200)	4.31 ± 0.21	0.09	0.18	0.05	0.04	
(200, 250)	3.39 ± 0.17	0.01	0.16	0.06	0.03	
(250, 300)	2.44 ± 0.22	0.14	0.16	0.06	0.05	
(300, 350)	1.99 ± 0.23	0.12	0.16	0.07	0.08	
(350, 400)	1.43 ± 0.28	0.23	0.11	0.05	0.10	
(400, ∞)	0.63 ± 0.30	0.27	0.09	0.05	0.05	

Table 7.3: Impurities for photons as a function of p_T .

Following this measurement, another control sample is formed where the photon in the photon plus jet sample is replaced by a hadronic proxy object. The hadronic proxy object is a reconstructed photon object which pass the photon ID described in Section 5.4 with the exception of failing at least one of the following cuts:

- $\sigma_{i\eta i\eta} < 0.01022$

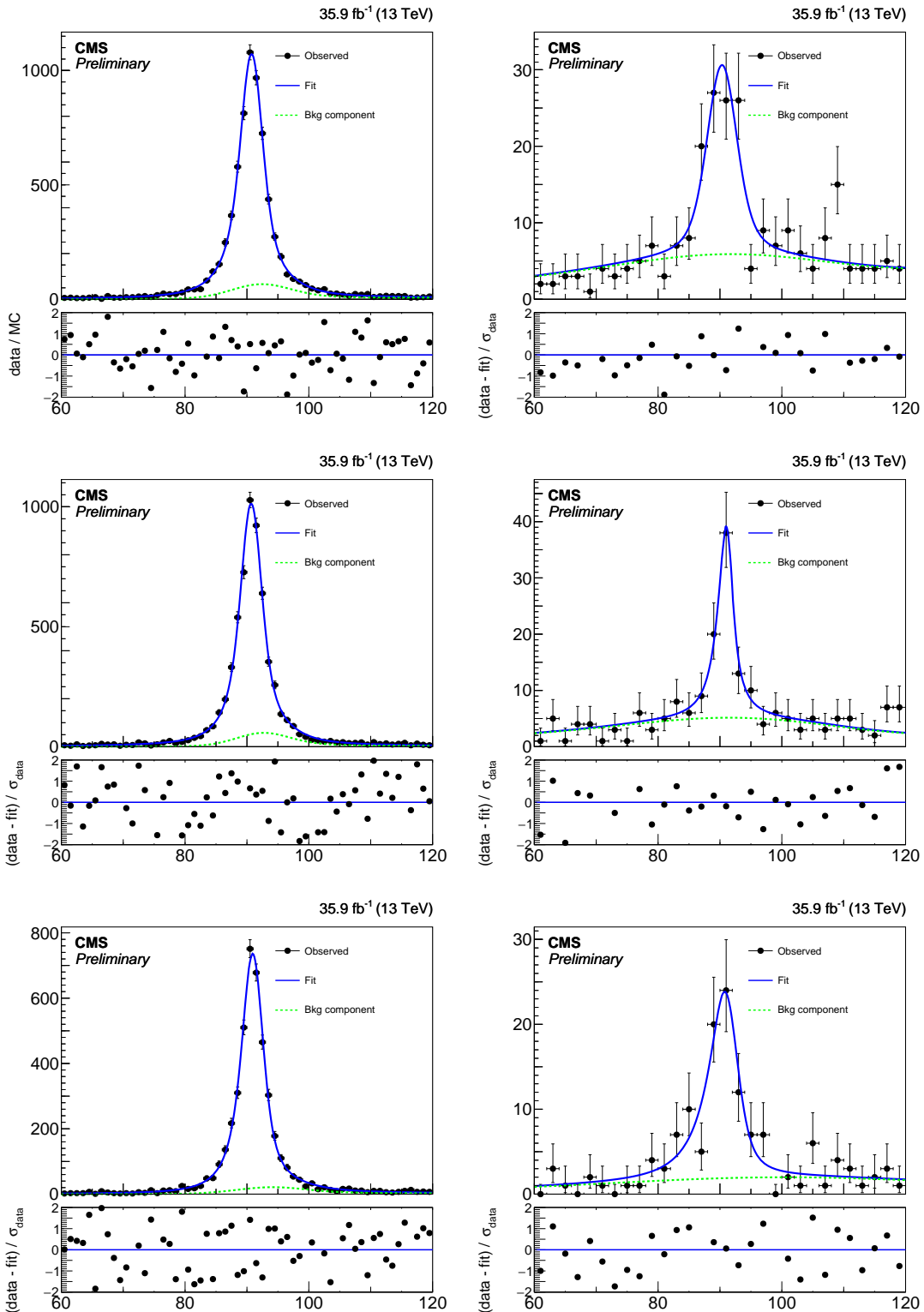


Figure 7-9: Fits to the mass distributions for ee (left) and $e\gamma$ (right) selections, in bins of probe p_T : $175 < p_T < 200$ GeV (top), $200 < p_T < 250$ GeV (middle), $p_T > 250$ GeV (bottom). The blue solid line represents the full fit model, and the green dashed line its background component.

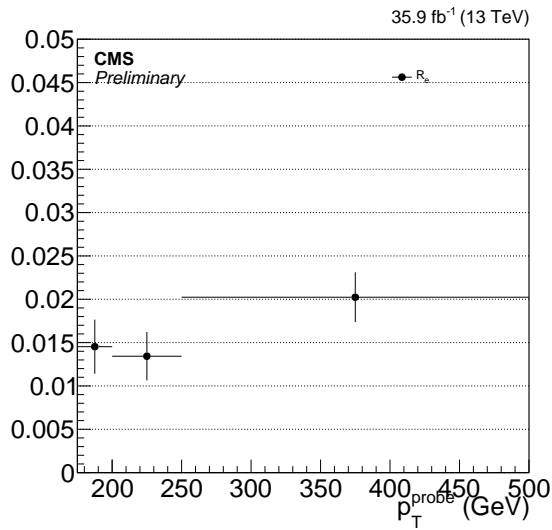


Figure 7-10: Electron to photon fake rate R_e .

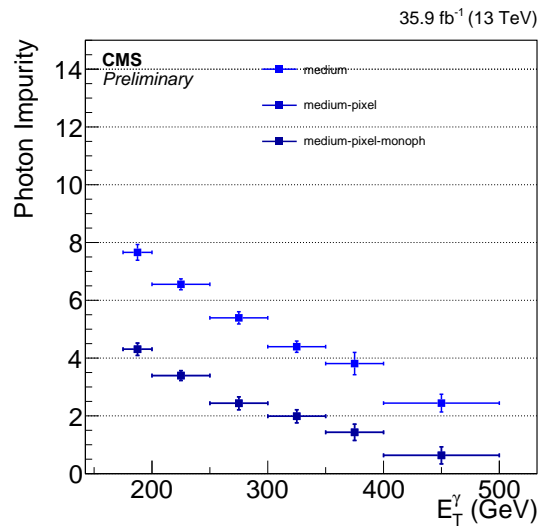


Figure 7-11: Impurities for photons as a function of p_T . The different bands show the effects of adding different stages of the full ID, starting with the baseline ID and isolation and successively adding the pixel seed veto.

- PF Charged Hadron isolation < 0.441 GeV .

Additionally, we apply a $E_T^{\text{miss}} < 60$ GeV cut to make this region orthogonal to the signal region of the analysis.

The hadronic transfer factor R_h , which measures the rate at which hadronic proxy objects result in hadrons that are misidentified as candidate photons, is obtained by dividing the estimated number of misidentified hadrons in the photon plus jet sample by the number of events in the hadron proxy + jet control region as a function of p_T . Figure 7-12 shows the transfer factor R_h along with the various distributions used for its derivation.

Finally, a third control sample of events with a hadronic proxy object and $E_T^{\text{miss}} > 170$ GeV is prepared. Under the assumption that the R_h stays constant regardless of whether the event has a high- p_T jet or E_T^{miss} , this proxy plus E_T^{miss} sample is then weighted by R_h to arrive at an estimate of the misidentified hadron plus E_T^{miss} background of this analysis.

To estimate the uncertainty on this background, we repeat the above method using tighter and looser definitions of the hadron proxy object. The tighter definition differs from the nominal by the following cuts:

- ρ -corrected PF Neutral Hadron isolation $< 0.264 + 0.014 \times p_T^\gamma + 0.000019 \times (p_T^\gamma)^2$.
- ρ -corrected PF Photon isolation $< 2.362 + 0.0053 \times p_T^\gamma$,

and the looser definition differs from the nominal by the following cuts:

- ρ -corrected PF Neutral Hadron isolation $< 10.910 + 0.014 \times p_T^\gamma + 0.000019 \times (p_T^\gamma)^2$.
- ρ -corrected PF Photon isolation $< 3.630 + 0.0053 \times p_T^\gamma$.

The different distributions from the nominal, tight, and loose selections are shown in Figure 7-13. The tight and loose shapes are taken as the one sigma band around the nominal estimate. Additionally, there is an uncertainty coming from the estimation of the photon purity. Figure 7-14 shows the resulting shapes from moving the shapes generated by a one sigma shift in the purity.

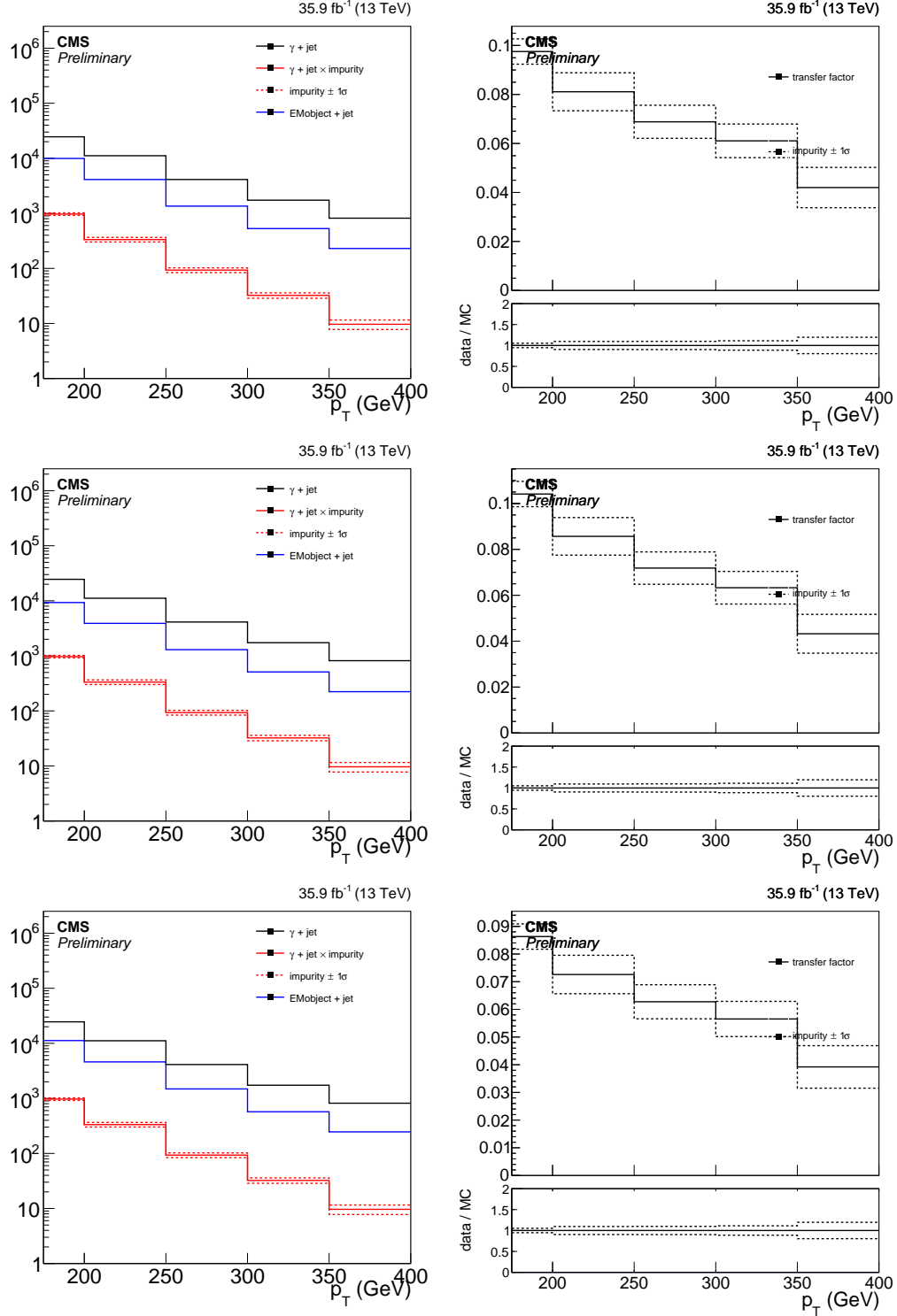


Figure 7-12: Left: The p_T distribution of the candidate photon object in the photon + jet control sample (black), the result of scaling it with the impurity (red), and the p_T distribution of the hadronic proxy object in the proxy + jet control sample (blue). Right: Hadronic transfer factor R_h , which is the ratio of the red and blue distributions in the left plot. Top: Nominal hadron proxy object. Middle: Tighter hadron proxy object. Bottom: Looser hadron proxy object.

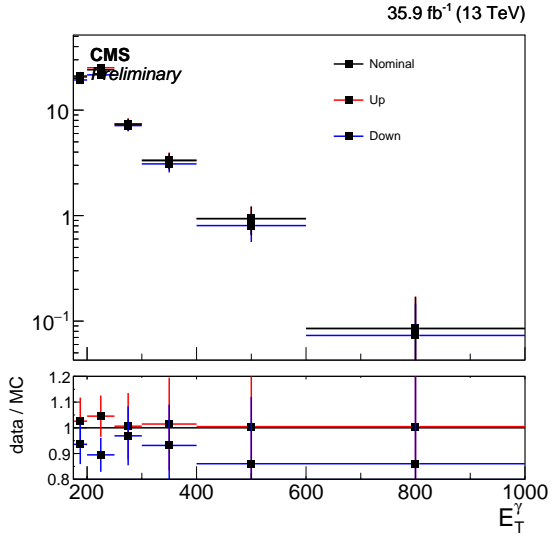


Figure 7-13: The p_T distribution of the estimated contribution from hadronic fakes in the signal region. The distribution labeled Up (Down) comes from the tighter (looser) selection. The systematic uncertainty resulting from this variation is around 5% at the low end of our p_T range and increases to 15% after $p_T > 400$ GeV.

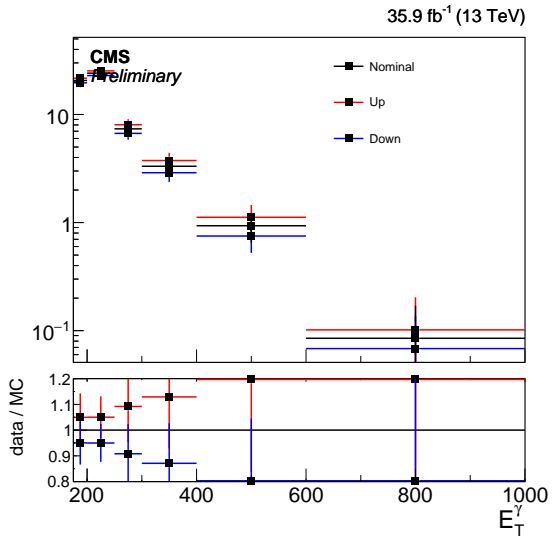


Figure 7-14: The p_T distribution of the estimated contribution from hadronic fakes in the signal region. The distribution labeled Up (Down) comes from varying the purity one sigma up (down). The systematic uncertainty resulting from this variation is around 5% at the low end of the p_T range and increases to 20% after $p_T > 400$ GeV.

7.5 Beam halo

Based on the beam halo features discussed in Section 5.9, a two-template fit to the ϕ' distribution of the photons in the candidate sample, where the templates are that of the halo shower and a uniform distribution, accurately estimates the amount of beam halo background present in the signal region. For this analysis, the splitting of the signal region functions in a similar manner, enabling us to determine the beam halo contribution during the signal extraction procedure.

In the horizontal (H) and vertical (V) signal regions, collision processes occupy the relative fractions of phase space $C_H = 1/\pi$ and $C_V = (\pi - 1)/\pi$, respectively. The corresponding fractions for beam halo events are determined by selecting a halo-enriched sample where the halo identification is inverted. Thus, a fit of the two signal regions provides an estimate of the overall normalization of the beam halo background, denoted h .

The E_T^γ dependence of the halo background is encoded in $n_{K,i}^{\text{halo}}$, the unit-normalized beam halo prediction in the i^{th} bin of the signal region $K \in \{H, V\}$. Using the notation introduced in Section 7.2, the total estimated background T_K in the two signal regions are

$$\begin{aligned} T_{K,i} &= C_K(N_i^{Z\gamma} + N_i^{W\gamma}) + hn_{K,i}^{\text{halo}} + C_K b_{K,i} \\ &= C_K(1 + f_{W\gamma i}^{Z\gamma -1})N_i^{Z\gamma} + hn_{K,i}^{\text{halo}} + C_K b_{K,i}, \end{aligned} \tag{7.4}$$

where $b_{K,i}$ is the total contribution to bin i of region K from electron and hadron misidentification, ECAL spikes, and other minor SM background processes.

7.6 Spikes

Given the observations in Section 5.10, the time distribution of spike-like rec hits outside of the window $-15 < t < -10$ ns (and the equivalent with one-bunch-crossing shift) is understood to be due to delayed interactions of neutral hadrons with the APDs, as documented also in Ref. [?]. In other words, ECAL spike clusters which

survive the time cleaning cut of the standard reconstruction are a part of a broad tail of a distribution, and there is no evidence of spike signals that specifically populate the “in-time” region $-3 < t < 3$ ns.

Having established that there is no special population of ECAL spikes in the in-time region, we can estimate the number of ECAL spike events present in the signal candidate sample by an “ABCD” method, where

- A = Number of clusters with $\sigma_{i\eta i\eta}$ or $\sigma_{i\phi i\phi}$ less than 0.001 and seed time $-15 < t < -10$ ns, counted in the special-reconstruction sample,
- B = Number of clusters with both $\sigma_{i\eta i\eta}$ and $\sigma_{i\phi i\phi}$ greater than 0.001 and seed time $-15 < t < -10$ ns, counted in the special-reconstruction sample,
- C = Number of clusters with $\sigma_{i\eta i\eta}$ or $\sigma_{i\phi i\phi}$ less than 0.001 but an in-time seed, counted in the standard-reconstruction sample passing all other signal event selection,

and D is the estimated number of spike events in the signal region, obtained by

$$D = C \times \frac{B}{A}. \quad (7.5)$$

The special-reconstruction samples for A and B are from the SinglePhoton datasets, with only the timing cleaning removed from the offline reconstruction. In this way, the selection bias over spikes from the L1T, HLT, and offline reconstruction is equally applied to samples A, B, and C.

Plugging in the observed numbers, we have

$$A = 4969$$

$$B = 1180$$

$$C = 54$$

$$\therefore D = 12.8 \pm 1.8(\text{stat.})$$

There are, however, at least two reasons to believe that this method overestimates

the number of spike events in the signal region. One is that the population C contains some physical, prompt photon clusters that just happens to be narrow, as observed in Fig. 5-14. Another reason is that there is likely a correlation between the cluster width and the seed time such that the ratio of true D to C is smaller than B/A . This statement is based on the standard hypothesis that the wide-cluster spike is an ECAL spike embedded in a physical EM shower cluster. Under this model, spikes in wide clusters are mainly caused by prompt neutral hadrons in a jet, which implies that they strongly prefer seed time $-15 < t < -10$ ns. Given that this is a minor background with a relatively large uncertainty, as described below, we will still use this estimate as the nominal value of predicted spike contribution in the signal region.

The uncertainty in the estimate of D is evaluated by two modifications to A, B, and C. First, the three values are recomputed with using $\sigma_{i\eta i\eta} < 0.001$ as the only definition of narrow cluster. This results in a minor change of the value of D of 12.1 ± 1.7 . Next, A and B are computed using a lower- p_T SinglePhoton sample, requiring triggers Photon135_PFMET100 or Photon120_R9Id90_HE10_IsoM to have fired, instead of the signal trigger. The second modification gives $D = 9.1 \pm 1.3$. We then take twice the discrepancy between the nominal D and the D value from the second modification as the systematic uncertainty in the spike background estimate.

7.7 Statistical Interpretation

The potential signal contribution is extracted from the data via simultaneous fits to the E_T^γ distributions in the signal and control regions defined in Section 7.1. Uncertainties in various quantities are represented by nuisance parameters in the fit. Predictions for $Z(\rightarrow \nu\bar{\nu})+\gamma$, $W(\rightarrow \ell\nu)+\gamma$, and the beam halo backgrounds are varied in the fit. Beam halo is not a major background, but the extraction of its rate requires a fit to the observed distributions in the signal region.

Free parameters of the fit are the yield of $Z(\rightarrow \nu\bar{\nu})+\gamma$ background in each bin of the signal regions ($N_i^{Z\gamma}$) and the overall normalization of the beam halo background (h). Bin-by-bin yields of $W(\rightarrow \ell\nu)+\gamma$ and $Z(\rightarrow \ell\bar{\ell})+\gamma$ samples in all regions are

related to the yield of $Z(\rightarrow \nu\bar{\nu}) + \gamma$ through the MC prediction through the transfer factors defined in Section 7.2. The transfer factors are allowed to shift within the aforementioned theoretical and experimental uncertainties.

The background-only likelihood that is maximized in the fit is

$$\begin{aligned}
\mathcal{L} &= \prod_i \{ \mathcal{L}_{\text{signal}} \times \mathcal{L}_{\text{single-lepton}} \times \mathcal{L}_{\text{dilepton}} \} \times \mathcal{L}_{\text{nuisances}} \\
&= \prod_i \left\{ \prod_{K=H,V} \mathcal{P}(d_{K,i} \mid T_{K,i}(\vec{\theta})) \times \prod_{\ell=e,\mu} \mathcal{P}(d_{\ell\gamma,i} \mid T_{\ell\gamma,i}(\vec{\theta})) \times \prod_{\ell=e,\mu} \mathcal{P}(d_{\ell\ell\gamma,i} \mid T_{\ell\ell\gamma,i}(\vec{\theta})) \right\} \times \prod_j \mathcal{N}(\theta_j) \\
&= \prod_i \left\{ \prod_{K=H,V} \mathcal{P}\left(d_{K,i} \mid \left(1 + f_{W\gamma,i}^{Z\gamma}{}^{-1}(\vec{\theta})\right) C_K N_i^{Z\gamma} + h n_{K,i}^{\text{halo}}(\vec{\theta}) + C_K b_{K,i}(\vec{\theta})\right) \right. \\
&\quad \times \prod_{\ell=e,\mu} \mathcal{P}\left(d_{\ell\gamma,i} \mid \frac{N_i^{Z\gamma}}{R_{\ell\gamma,i}^{W\gamma}(\vec{\theta}) f_{W\gamma,i}^{Z\gamma}(\vec{\theta})} + b_{\ell\gamma,i}(\vec{\theta})\right) \\
&\quad \left. \times \prod_{\ell=e,\mu} \mathcal{P}\left(d_{\ell\ell\gamma,i} \mid \frac{N_i^{Z\gamma}}{R_{\ell\ell\gamma,i}^{Z\gamma}(\vec{\theta})} + b_{\ell\ell\gamma,i}(\vec{\theta})\right) \right\} \times \prod_j \mathcal{N}(\theta_j), \\
\end{aligned} \tag{7.6}$$

following the notation introduced in Section 7.2, and where $\mathcal{P}(n|\lambda)$ is the Poisson probability of n for mean λ , \mathcal{N} denotes the unit normal distribution, and $d_{X,i}$ is the observed number of events in bin i of region X. Systematic uncertainties are treated as nuisance parameters in the fit and are represented by $\vec{\theta}$. Each quantity Q_j with a nominal value \bar{Q}_j and a standard deviation of the systematic uncertainty σ_j appears in the likelihood function as $\bar{Q}_j \exp(\sigma_j \theta_j)$.

7.8 Results

7.8.1 Pre-fit and post-fit distributions

Figure 7-15 shows the observed E_T^γ distributions in the four control regions compared with the results from simulations before and after performing the simultaneous fit across all the control samples and signal region, and assuming absence of any signal. Figure 7-16 shows the observed E_T^γ distributions in the horizontal and vertical signal regions compared with the results from simulations before and after performing a

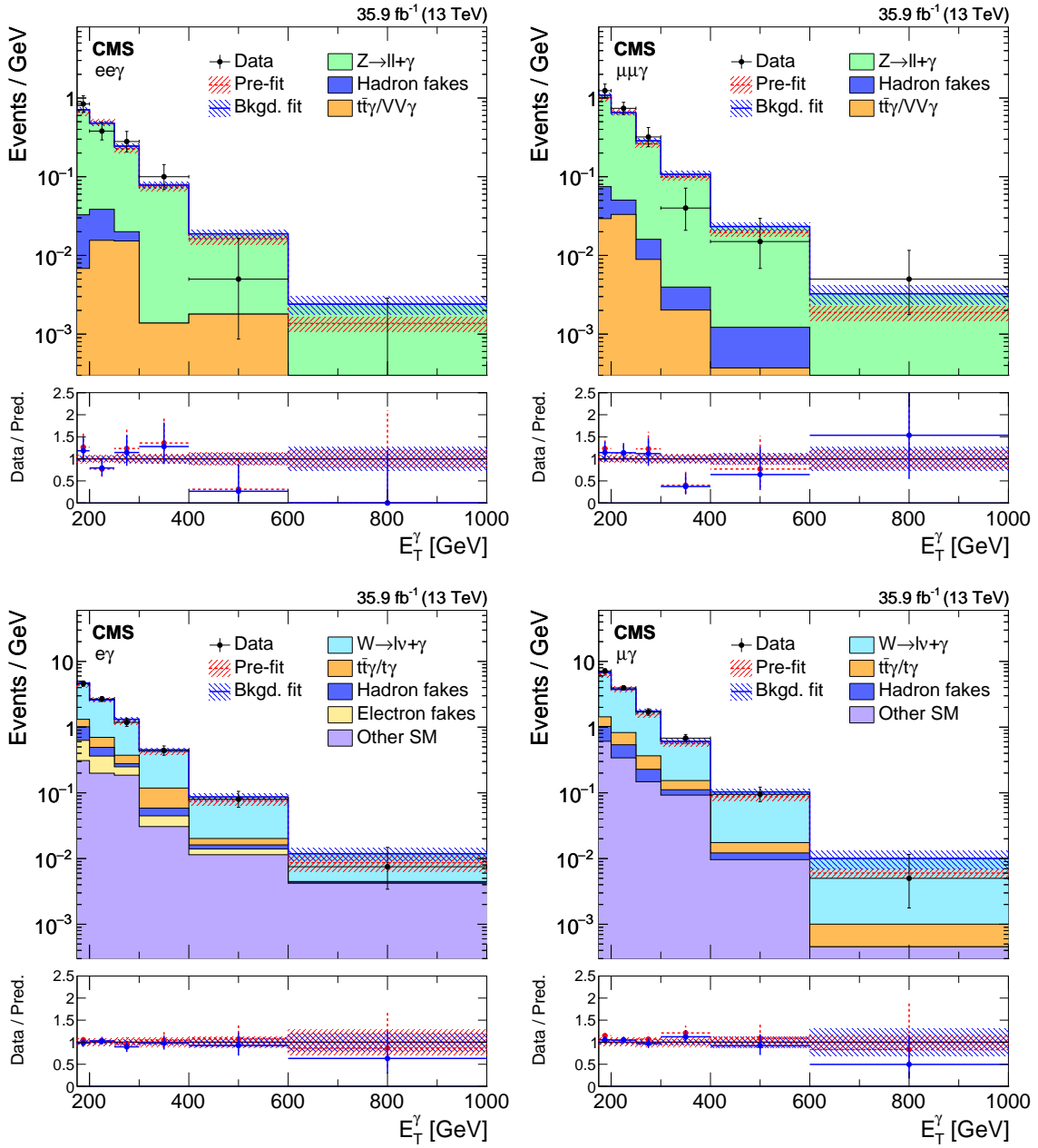


Figure 7-15: Comparison between data and MC simulation in the four control regions: $ee\gamma$ (upper left), $\mu\mu\gamma$ (upper right), $e\gamma$ (lower left), $\mu\gamma$ (lower right) before and after performing the simultaneous fit across all the control samples and signal region, and assuming absence of any signal. The last bin of the distribution includes all events with $E_T^\gamma > 1000$ GeV. The ratios of data with the pre-fit background prediction (red dashed) and post-fit background prediction (blue solid) are shown in the lower panels. The bands in the lower panels show the post-fit uncertainty after combining all the systematic uncertainties.

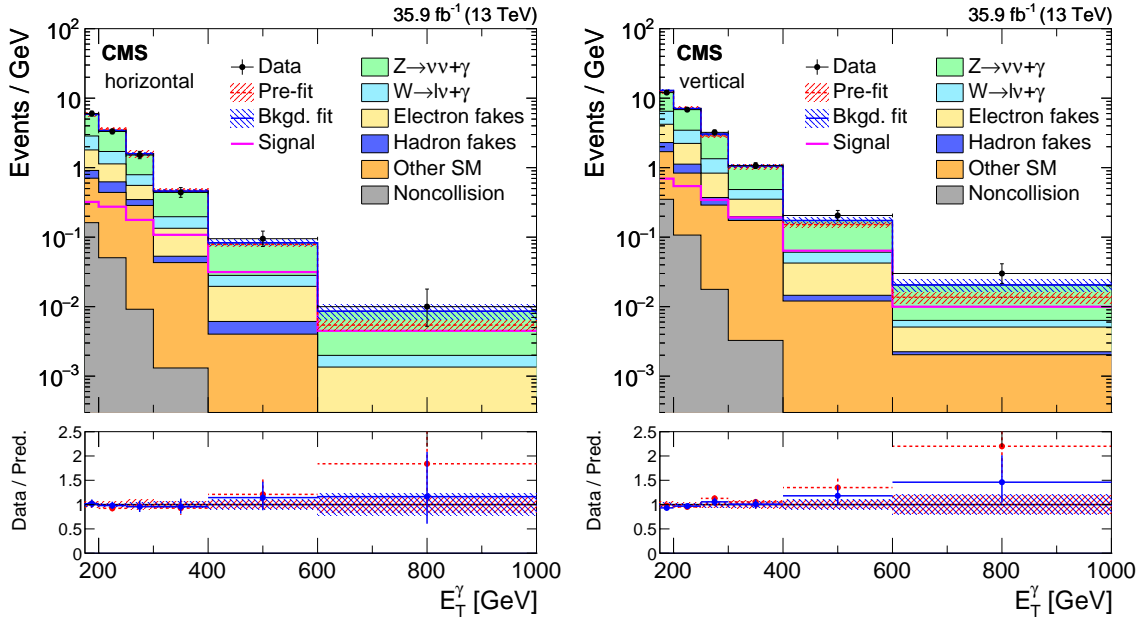


Figure 7-16: Observed E_T^γ distributions in the horizontal (left) and vertical (right) signal regions compared with the post-fit background expectations for various SM processes. The last bin of the distribution includes all events with $E_T^\gamma > 1000$ GeV. The expected background distributions are evaluated after performing a combined fit to the data in all the control samples and the signal region. The ratios of data with the pre-fit background prediction (red dashed) and post-fit background prediction (blue solid) are shown in the lower panels. The bands in the lower panels show the post-fit uncertainty after combining all the systematic uncertainties. The expected signal distribution from a 1 TeV vector mediator decaying to 1 GeV DM particles is overlaid.

combined fit to the data in all the control samples and the signal region. The observed distributions are in agreement with the prediction from SM and noncollision backgrounds.

Table 7.4: Expected event yields in each E_T^γ bin for various background processes in the horizontal signal region. The background yields and the corresponding uncertainties are obtained after performing a combined fit to data in all the control samples, excluding data in the signal region. The observed event yields in the horizontal signal region are also reported.

E_T^γ [GeV]	[175, 200]	[200, 250]	[250, 300]	[300, 400]	[400, 600]	[600, 1000]
$Z\gamma$	81.2 ± 8.0	88.2 ± 8.4	38.8 ± 4.8	26.8 ± 3.7	8.8 ± 1.9	1.4 ± 0.7
$W\gamma$	27.9 ± 3.7	29.9 ± 3.9	11.4 ± 1.7	6.3 ± 1.2	1.4 ± 0.4	0.1 ± 0.1
Misid. electrons	22.5 ± 2.7	25.7 ± 2.7	10.5 ± 1.0	8.2 ± 0.7	2.7 ± 0.2	0.5 ± 0.0
Misid. hadrons	5.2 ± 2.2	9.3 ± 1.8	3.1 ± 0.7	1.0 ± 0.3	0.4 ± 0.1	0.0 ± 0.0
Other SM	13.6 ± 2.0	19.6 ± 1.3	13.9 ± 0.4	4.2 ± 0.2	0.8 ± 0.0	0.1 ± 0.0
ECAL spikes	4.3 ± 1.3	2.7 ± 0.8	0.5 ± 0.1	0.1 ± 0.0	0.0 ± 0.0	0.0 ± 0.0
Total prediction	154.6 ± 8.3	175.4 ± 8.8	78.2 ± 5.3	46.6 ± 4.0	14.1 ± 2.1	2.1 ± 0.8
Observed	150 ± 12	166 ± 13	76.0 ± 8.7	44.0 ± 6.6	19.0 ± 4.4	4.0 ± 2.0

Table 7.5: Expected event yields in each E_T^γ bin for various background processes in the vertical signal region. The background yields and the corresponding uncertainties are obtained after performing a combined fit to data in all the control samples, excluding data in the signal regions. The observed event yields in the vertical signal region are also reported.

E_T^γ [GeV]	[175, 200]	[200, 250]	[250, 300]	[300, 400]	[400, 600]	[600, 1000]
$Z\gamma$	172 ± 17	190 ± 18	83 ± 10	58.6 ± 7.9	18.0 ± 3.9	3.1 ± 1.6
$W\gamma$	59.9 ± 7.8	63.6 ± 7.8	24.6 ± 3.5	13.4 ± 2.4	3.0 ± 0.8	0.3 ± 0.2
Misid. electrons	48.4 ± 5.6	56.2 ± 5.1	23.4 ± 1.8	15.7 ± 1.4	5.6 ± 0.4	1.2 ± 0.1
Misid. hadrons	15.1 ± 4.4	14.5 ± 3.1	4.2 ± 0.8	2.3 ± 0.8	0.5 ± 0.1	0.1 ± 0.1
Other SM	33.8 ± 4.1	36.6 ± 2.7	13.6 ± 0.5	17.1 ± 0.6	2.4 ± 0.1	0.8 ± 0.0
ECAL spikes	9.3 ± 2.8	5.7 ± 1.7	0.9 ± 0.3	0.3 ± 0.1	0.0 ± 0.0	0.0 ± 0.0
Total prediction	339 ± 18	366 ± 19	150 ± 11	107.5 ± 8.7	29.6 ± 4.3	5.4 ± 1.7
Observed	301 ± 17	342 ± 19	161 ± 13	107 ± 10	41.0 ± 6.4	12.0 ± 3.5

The expected yields in each bin of E_T^γ for all backgrounds in the horizontal and vertical signal regions after performing a combined fit to data in all the control samples, excluding data in the signal regions, are given in Tables 7.4 and 7.5, respectively. The covariances between the predicted background yields across all the E_T^γ bins in the two signal regions are shown in Fig. 7-17. The expected yields together with the

covariances can be used with the simplified likelihood approach detailed in Ref. [?] to reinterpret the results for models not studied in this thesis

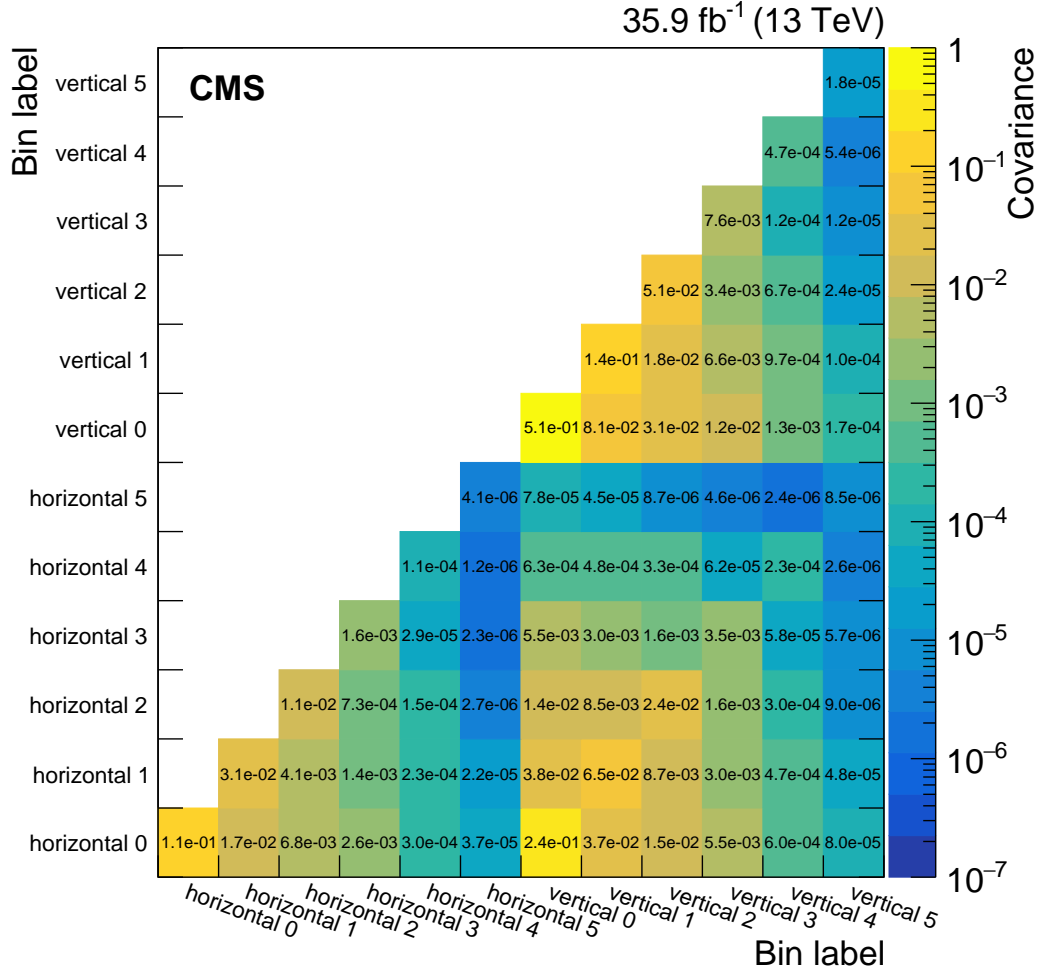


Figure 7-17: Covariances between the predicted background yields in all the E_T^γ bins of the horizontal and vertical signal regions. The bin labels specify which signal region the bin belongs to and what number bin it is for that region.

7.8.2 Limits

No significant excess of events beyond the SM expectation is observed. Upper limits are determined for the production cross section of the new-physics processes mentioned in Section ???. For each model, a 95% confidence level (CL) upper limit is

obtained utilizing the asymptotic CL_s criterion [?, ?, ?], using a test statistic based on the negative logarithm of the likelihood in Section 7.7.

Figure 7-18 shows the 95% CL upper cross section limits with respect to the corresponding theoretical cross section ($\mu_{95} = \sigma_{95\%}/\sigma_{\text{theory}}$) for the vector and axial-vector mediator scenarios, in the $M_{\text{med}}-m_{\text{DM}}$ plane. The solid black (dashed red) curves are the observed (expected) contours of $\mu_{95} = 1$. The σ_{theory} hypothesis is excluded at 95% CL or above in the region with $\mu_{95} < 1$. The uncertainty in the expected upper limit includes the experimental uncertainties. For the simplified DM LO models considered, mediator masses up to 950 GeV are excluded for values of m_{DM} less than 1 GeV.

The results for vector and axial-vector mediators are compared to constraints from the observed cosmological relic density of DM as determined from measurements of the cosmic microwave background by the Planck satellite experiment [?]. The expected DM abundance is estimated, separately for each model, using the thermal freeze-out mechanism implemented in the MADDM [?] framework and compared to the observed cold DM density $\Omega_c h^2 = 0.12$ [?], where Ω_c is the DM relic abundance and h is the dimensionless Hubble constant.

To enable a direct comparison with results from direct and indirect detection experiments, the 95% CL limits on the mediator mass for the vector and axial-vector models are translated to 90% CL limits on the spin-independent and spin-dependent DM–nucleon scattering cross sections, σ_{SI} and σ_{SD} respectively, following the prescriptions given in Ref. [?] and [?]. The exclusion contours for the vector and axial-vector models shown in Figure 7-18 are translated into the $\sigma_{\text{SI}}-m_{\text{DM}}$ and $\sigma_{\text{SD}}-m_{\text{DM}}$ planes shown in Figure 7-19. When compared to recent results by the CDMSLite [?], LUX [?], PandaX-II [?], XENON1T [?], and CRESST-II [?] collaborations, the limits obtained from this search provide stronger constraints for DM masses less than 2 GeV for spin independent models. When compared to recent results by the PICO-60 [?], IceCube [?], PICASSO [?] and Super-Kamiokande [?] collaborations, the limits obtained from this search provide stronger constraints for DM masses less than 200 GeV for spin dependent models.

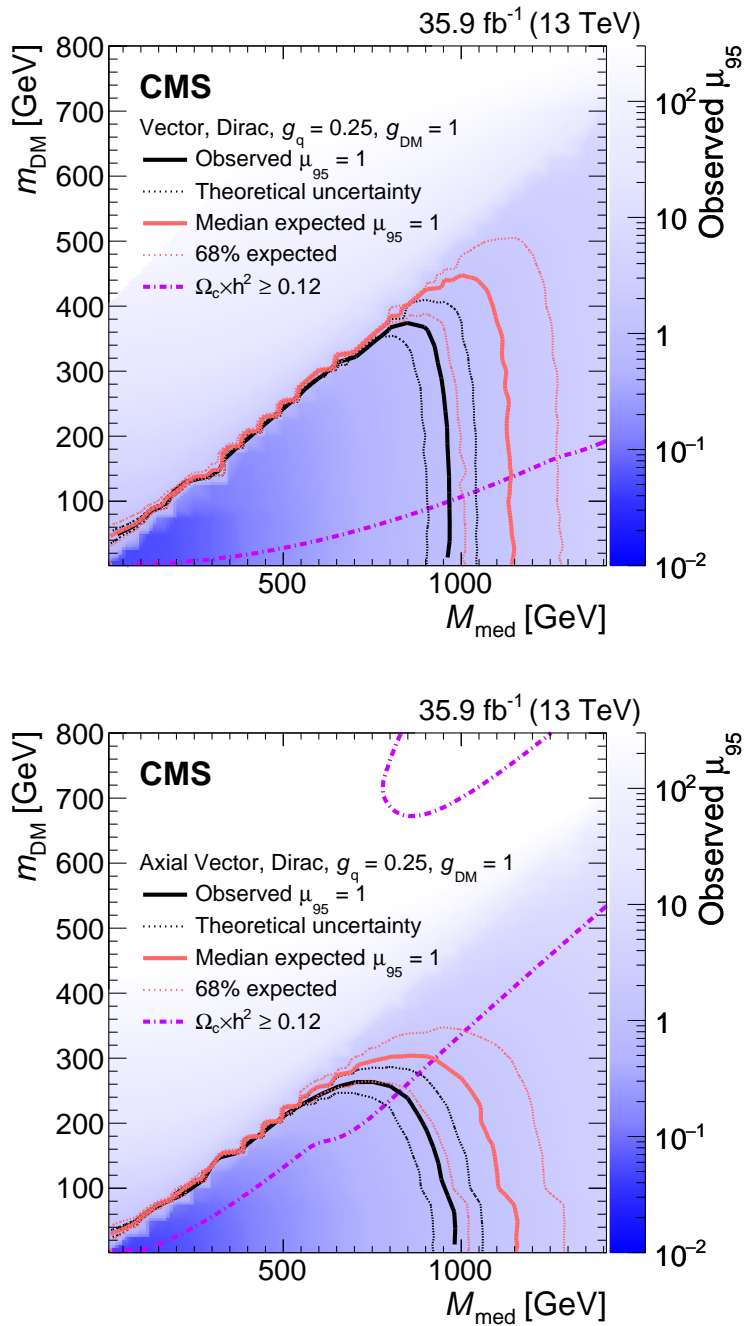


Figure 7-18: The ratio of 95% CL upper cross section limits to the theoretical cross section (μ_{95}), for DM simplified models with vector (top) and axial-vector (bottom) mediators, assuming $g_q = 0.25$ and $g_{\text{DM}} = 1$. Expected $\mu_{95} = 1$ contours are overlaid in red. The region under the observed contour is excluded. For DM simplified model parameters in the region below the lower violet dot-dash contour, and also above the corresponding upper contour in the right hand plot, cosmological DM abundance exceeds the density observed by the Planck satellite experiment.

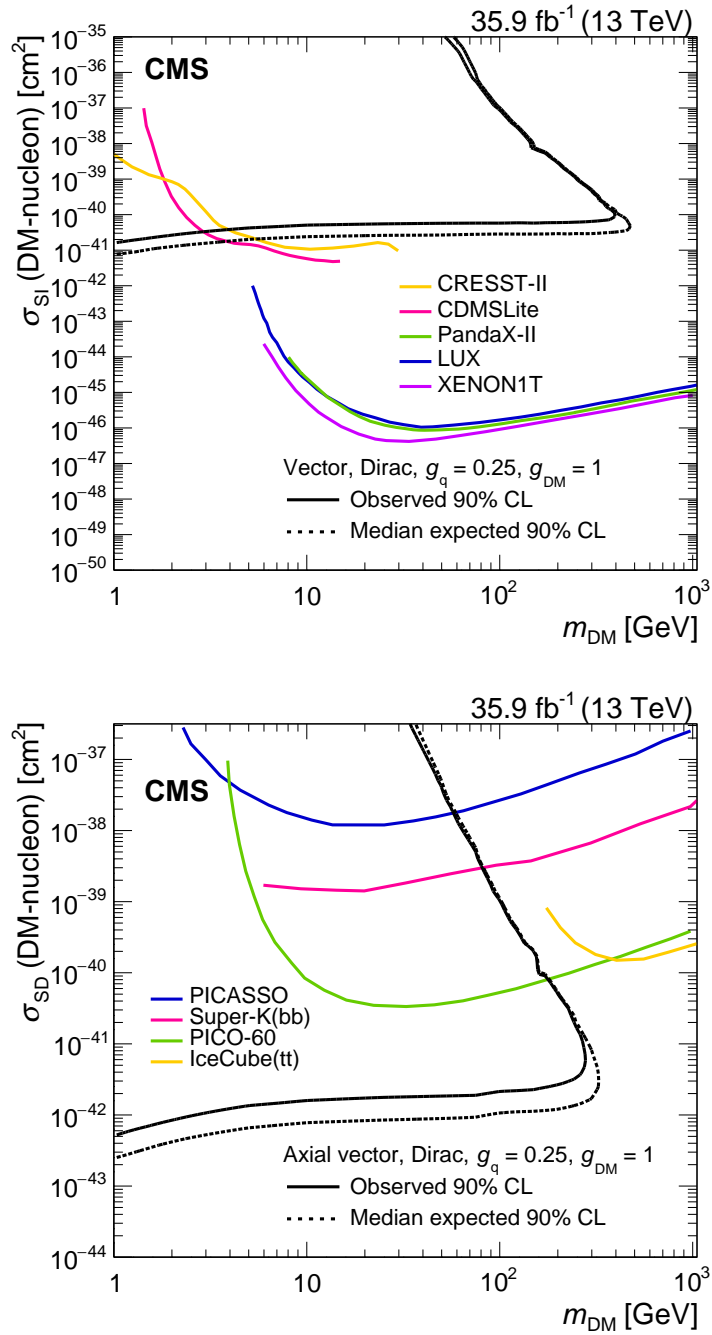


Figure 7-19: The 90% CL exclusion limits on the χ -nucleon spin-independent scattering cross sections involving the vector operator (top) and the χ -nucleon spin-dependent scattering cross sections involving the axial-vector operator (bottom) as a function of the m_{DM} . Simplified model DM parameters of $g_q = 0.25$ and $g_{\text{DM}} = 1$ are assumed. The region to the upper left of the contour is excluded. On the plots, the median expected 90% CL curve overlaps the observed 90% CL curve. Also shown are corresponding exclusion contours, where regions above the curves are excluded, from the recent results by the direct and indirect detection experiments listed in the text.